Physikalisches Institut III
Universität Stuttgart
Pfaffenwaldring 57
70550 Stuttgart

Decoherence properties of the NV-center in diamond

Von der Fakultät Mathematik und Physik der Universität Stuttgart zur Erlangung der Würde eines Doktors der Naturwissenschaften (Dr. rer. nat.) genehmigte Abhandlung

Vorgelegt von

Florian Rempp

aus Aalen

Hauptberichter:	Prof. Dr. Jörg Wrachtrup
Mitberichter:	Prof. Dr. Hans Peter Büchler
Tag der mündlichen Prüfung:	26. Oktober 2011

Physikalisches Institut der Universität Stuttgart

2011

Acknoledgements

I would like to thank Professor Wrachtup for letting me join his institute in order to pursue my PhD thesis. For very fruitful discussions and advice whenever it was needed.

Professor Buechler has my gratitude for accepting to do the second report for this work.

Professor Twamley greatly supported my work with all his “crazy” ideas and fruitful discussions. Especially I would like to thank him for the time he let me join his institute at Macquarie University.

Further thanks go to Professor Jelezko who always had an open ear and good advice.

I thank Dr. Jared Cole for sharing his insights into the noise spectral density and encourage me to pursue this idea further.

I would like to thank Dr. Balasubramanian for being the first to believing in my calculations on the noise spectral density and conducting the first measurements on the subject - it was a great collaboration.

To Dr. Naydenov and Dr. Reinhard I am grateful for countless fruitful discussions and the proofreading of this thesis.

All the members of the third institute - working with you was brilliant. Here I want to point out Phillip Neumann, Johannes Beck, Konstantin Schukraft and Florian Dolde for many fruitful discussions and Julia Michl for proofreading this thesis.

Special thanks to Heiko Schröder and Christoph Schimeczek for all the good times at our early riser breakfast.

I thank my parents without their support this would not have been possible.

Most of all I thank my wife Stefanie for always being there for me especially in the last phase of this thesis - You are the love of my live!

Contents

Part I.

Introduction

1. Introduction

The introduction of information processing to quantum science has led to a great variety of innovations. Beside the perspective to simulate large quantum systems exactly [31] or efficiently find the prime factors of large numbers [90] the biggest achievement of quantum computing is that it established a common language in quantum science. From electron spin resonance via supra conducting circuits to quantum dots and defect centers in diamond ideas and concepts can be transfered by reducing the description to the application of so called quantum gates, the quantum analogon to logic gates in classical information processing. The precise implementation of such a gate may differ greatly in the respective system, but the outcome and purpose remains the same. The research for a quantum computer has led to many developments like quantum cryptography [13], tailoring of matter on the nano scale [61, 69, 71, 33, 43] or metrology of ambient fields [4, 26, 97] along the way. They are nowadays of equal importance than the original goal itself. For example it is possible to measure magnetic fields down to the attotesla range employing quantum devices like SQUIDS [27] or nanotesla with a nanometer lateral resolution with solid state spin systems [4]. In the pursue of a scalable quantum computer DiVincenzo gave five criteria a given system has to fulfill in order to build a scalable quantum device [24].

The first criterion is to have a scalable physical system with well characterized qubits. This sounds simpler than it actually is. In order to be a well characterized qubit the system has to be able to assume every possible state of the single qubit Hilbert space independent of the other qubit states. One could e.g. define two quantum dots sharing one electron as a two qubit system with the eigenstates $|10\rangle$ (electron on the left dot) and $|01\rangle$ (electron on the right dot). This would not constitute valid qubits because the $|00\rangle$ and $|11\rangle$ states can not be assumed. The double dot system forms a single qubit with $|0\rangle$ (electron on the left dot) and $|1\rangle$ (electron on the right dot). In addition the system has to be reproducible in a deterministic way in order to build an arbitrary sized quantum computer. This second part is actually no problem for mesoscopic systems like superconducting qubits, but solid state systems can not be controlled on a sub nano scale in order to place single defects in a solid state system. But implantation techniques are improved continuously

reaching a lateral resolution of few nanometer [88].

Secondly one has to be able to initialize the system into a simple pure state like $|000\ldots\rangle$. From a classical computing point of view it is natural to have all registers initialized in a known state. Additionally quantum error correction needs a steady supply of low entropy anzilla qubits. So single qubits will have to be continuously reinitialized to provide those anzilla qubits. Most systems settle here with a pseudo pure state by going to cryogenic temperatures with $k_\mathrm{B}\,T \ll \Delta E$ with ΔE the splitting of the two qubit states. Otherwise one has to rely on algorithmic cooling techniques [9, 14, 83] to polarize the system below the thermal state. One seldom implemented initialization method would be by a projective measurement with an additional spin flip depending on the measurement outcome.

It is also required that the coherence time of the qubits is much longer than the gate operation time. By coupling to environmental degrees of freedom the state of the qubits is changed. A superposition state $|\Psi\rangle = a\,|0\rangle + b\,|1\rangle$ is transformed to an incoherent superposition $\rho = |a|^2\,|0\rangle\langle 0| + |b|^2\,|1\rangle\langle 1|$ by this interaction. Accordingly the whole computation has to be done on a time scale on that the system is not changed by the environment. As a figure of merit the ratio of gate time over coherence time should be of the order of 10^{-4}. Until in 1995 it was discovered that quantum error correction is actually possible [95] this would probably be unachievable. To understand the mechanisms of decoherence is the main requirement to be able to engineer the environment such, that coherence time is naturally prolonged or to be able to dynamically decouple the system from a major part of the environmental degrees of freedom. This is one of the major topics of this work.

DiVicenzos fourth criterion is to provide an universal set of quantum gates. The dynamics of the quantum register is controlled by the application of unitary operations. Each algorithm can be described as a series of unitary transformations $\hat{U} = \hat{U}_1 + \hat{U}_2 + \ldots$ with $\hat{U}_k = \exp[-\mathrm{i}\,\hat{H}_k\,\tau_k]$. The theoretically simplest solution would be to design the system such that the Hamiltonians $\hat{H}_k$ are switched on and off for the duration τ_k. In practice this is not so simple at all. The system imposes constraints on what unitary operations are feasible. Understanding how much control is at least required is at the heart of this criterion. It can be shown that arbitrary quantum processes can be re-expressed as one and two body transformations [23]. For the two body interaction even one type, the so called CNOT gate is sufficient [6]. So the CNOT gate plus an arbitrary single qubit rotation together pose a set of universal gates as the xor gate in classical computing.

Finally one has to be able to do a projective measurement on specific qubits. In the ideal case any given qubit should be read with a quantum efficiency of

one. In reality less is sufficient. As long as the measurement does not disturb the rest of the system, measurements can be repeated in order to increase the effective quantum efficiency of the system. It would be advantageous to be able to perform a measurement on the time scale of a single gate application. This would greatly simplify the quantum error correction.

Due to the relative nature of the above criteria it is possible to find a trade of between them. If one requirement is very hard to achieve overachieving at an an other might solve the problem, thus a variety of systems is thinkable.

Several different systems have been proposed as possible quantum computers [56, 94, 103, 22]. After room temperature nuclear magnetic resonance (NMR) has been shown to be essentially classical [38] efforts have focused on ultra cold systems like trapped ions or superconducting circuits. In recent years however the nitrogen vacancy (NV) center in diamond has advanced to one of the most promising candidates for an actual quantum processor. Due to the embedding in the extremely rigid and nearly spin free diamond lattice it is the only solid state system that allows room temperature quantum experiments. Coherence times up to the order of milliseconds have been observed [5]. With the average gate time about 10 ns actual quantum computing should be possible. It features all optical initialization, control and readout on a single center level.

2. Diamond a Quantum Material

Figure 2.1.: from left to right: Catharine the Great with her scepter holding the Orloff, Napoleon Bonaparte with the Regent diamond in the hilt of his coronation sword, Queen Elizabeth with the Koh-I-Noor right in the middle of the front cross and the Scepter with the cross housing the biggest of the culligan diamonds is part of the English crown jewels as well.

"Diamonds are a girls best friends" is the title of the famous song Marilyn Monroe sang in the 1953 movie "Gentlemen Prefer Blondes". It tells that girls prefer expensive gifts over courting with odes to their beauty, because the latter will cease with time but diamonds are forever. Most people know diamond as a vivid sparkling brilliant made into jewelery. To own diamonds the bigger the better was a sign of wealth and prestige at all times. The biggest and purest diamonds like the culligan, the blue Wittelsbacher, the Orloff or the Dresden green diamond (fig. 2.1) are part of crown jewels of the most influential royal families of europe. As a symbol of endless love, diamonds are given by men to their loved ones. People are fascinated by the inner fire and beauty of diamonds. All the myths and fairy tales around diamonds are not without a reason. Diamond is not only extreme in its beauty but also in most of its material properties as well. It is e.g. the hardest material there is, only scratched by other diamond. Because the hardness is anisotropic with a

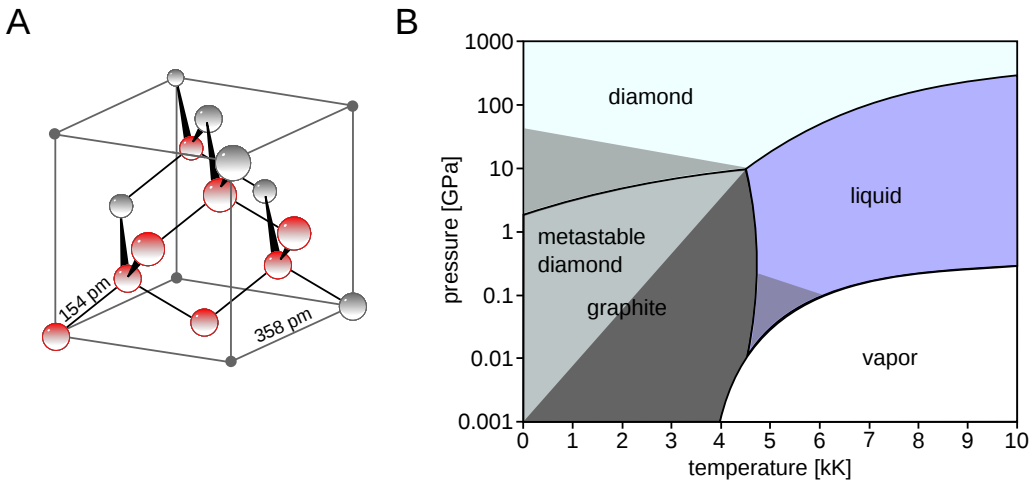

Figure 2.2.: **A** Schematic of the diamond unit cell. The red globes indicate the eight lattice sites assotiated with it. **B** The carbon phase diagram. Standard conditions are located in the lower left corner.

maximum along the [111] direction this is possible at all. Its inner fire, the sparkling when cut into facets originates of its immense index of refraction $n = 2.417$. For comparison glass has about $n = 1.5$. The diamond lattice is comprised purely of sp3 hybridized carbon atoms set with tetrahedral symmetry. This leads to 8 carbon sites within one unit cell of 0.3567 nm (fig. 2.2) with a bond length of 0.154 nm. The binding energy of $C - C$ bonds is at 350 kJ/mol which is actually 260 kJ/mol less than the sp2 double binding of graphite, but the graphite layers are only connected by Van-der-Waals-forces which drastically weakens the overall structure. Due to this rigid lattice structure and strong bounds diamond also features the highest heat conductivity ($k = 900 - 2.320\,W\,m^{-1}\,K^{-1}$) of any bulk material at room temperature. Copper for example comes with $k = 401\,W\,m^{-1}\,K^{-1}$. The diamond crystal structure and binding strength also results in a Debye temperature of 1860 K. So virtually no phonons are excited at room temperature. Additionally the most abundant isotope ^{12}C which makes up 98.9 % of the natural occurring carbon carries no nuclear spin. The diamond lattice is therefore essentially spin free except for 1.1 % ^{13}C with $I = 1/2$, thus enabling us to conduct room temperature quantum experiments. Diamond is a high bandgap semiconductor with a bandgap of 5.5 eV which corresponds to deep ultra violet light with a wavelength of 225 nm. So it is transparent to all visible wavelengths. A pure diamond crystal thus appears colorless. Color originates from chemical im-

purities such as nitrogen which is the most common impurity coloring yellow or boron that leads to blue. Nitrogen also forms the nitrogen-vacancy (NV) center that gives the diamond a pinkish red color.

In contrary to Marilyn Monroe's song Diamonds are not forever. Actually they are not stable under ambient conditions. The sp2 hybridized graphite is the stable configuration there with an energy difference of of $\approx 2.9\,\mathrm{kJ/mol}$. Due to the high energy barrier of $\approx 728\,\mathrm{kJ/mol}$ the diamond to graphite transition is extremely slow. The activation energy is so high because there are no other metastable structures to aid the transformation process. So a significant number of bonds have to be broken to disrupt the diamond structure and transform it into sp2 bonds. This may occur due to massive ion irradiation or thermally above 800° C in air or 1500° C in vacuum.

Since in 1814 H. Davy discovered that diamond is made up of pure carbon people have tried to turn cheap carbon material into diamond. Until 1879 James Ballantyne Hannay [42] discovered a way to do it. He put charcoal into an iron crucible and heated it up to $3500^\circ C$ then he rapidly cooled the compartment with water. The contraction of the iron provided enough pressure to turn the charcoal into diamond. Unfortunately his experiment could not be reproduced. It took until 1955 when Hall used a so called belt press to provide the pressure of 10 GPa that is necessary to turn carbon material into diamond at 2000° C. This high pressure high temperature (HPHT) method has not changed since then. There are two major press designs the belt press where two anvils provide pressure on top and bottom of a tube. On the bottom anvil a seed diamond crystal is placed on top of that comes a metal slug with the carbon material on top of it. Now pressure and temperature are raised to allow diamond to grow. By a small temperature gradient of approximately 50 K the carbon from the top of the tube is brought towards the diamond seed where it crystalizes. The second design the cubic press employs six anvils around a cubic sample. This in general smaller presses can reach the needed pressure faster than the belt press, but are not scaled easily to larger volumes because the required force is proportional to the area of the anvils, which can be kept constant with the belt press but not with the cubic press. The first diamonds produced that way were comparatively small yellowish crystals with rather bad crystallinity not suitable for jewelry. Today it is possible to replace the nitrogen by titanium or aluminium to create white crystals or boron to make blue ones for the price of lower crystallinity and hardness. Although since 1970 it is possible to create gem quality crystals by the HPHT method it is widely used today to manufacture small, nitrogen rich diamonds for industrial application in tools. They are used to coat cutting tools as scalpels, heavy duty grinding disks or drills to improve cutting performance and durability. Still it is desir-

able to produce single crystal diamond for various applications beside jewelery especially grown on non diamond surfaces like silicon or metals. A different technique was developed in three independent groups of Eversole (1963), Angus (1968) and by Deryagin and Fedoseev in 1970. While Eversole and Angus relied on single crystal diamonds as a substrate Deryagin and Fedoseev were able to grow diamond on silicon and metal surfaces. All of them deposited the carbon from a carbon plasma at rather mild temperatures of around 800° C. With this chemical vapor deposition (CVD) technique it is possible to engineer the chemical composition to a very high degree. Diamonds with down to 0.003 % of ^{13}C have been produced by Twitchen [5] with nitrogen concentration below the ESR detection limit ($\sim$ 1 ppb). These isotopically pure CVD provide the perfect frame for room temperature quantum experiments. Yet another method to generate diamond crystals is from explosives. Here conventional carbon containing explosives are detonated in sealed chambers. Heat and pressure are supplied by the explosion. The explosion chamber is rapidly cooled down to prevent the new formed diamonds from transforming into graphite. The crystals formed with this explosive growth technique have sizes in the order of a few nm set into aggregates with lots of graphite which is removed afterwards by acid treatment. Summarizing diamond is the only solid allowing room temperature quantum experiments with optical access. It can be manufactured at very high degree of crystallinity as well as chemical and isotopical purity. So one can truly say "diamonds are a physicists best friend"

2.1. The Nitrogen-Vacancy-Center in Diamond as a Quantum Register

The nitrogen vacancy (NV) center is formed by a substitutional nitrogen atom with a vacant lattice site next to it. Three dangling bonds are reaching into the vacancy from the remaining neighboring carbon sites. With the two unbound atoms of the nitrogen this forms a a five electron system. Due to its embedding in the diamond structure (fig. 2.3) its wave function has C_{3v} symmetry [62] resulting in one unpaired electron. In this uncharged state the NV_0 has therefore electron spin $S = 1/2$.

If the NV_0 catches an additional electron the two unpaired electrons form a ^{3}A triplet ground state with a zero field splitting (ZFS) of $D = 2.87$ GHz [62, 35](fig. 2.3). This stable configuration is called NV_-. The resonant transition to the ^{3}E excited state triplet ($D_e = 1.42$ GHz) is at a wavelength of

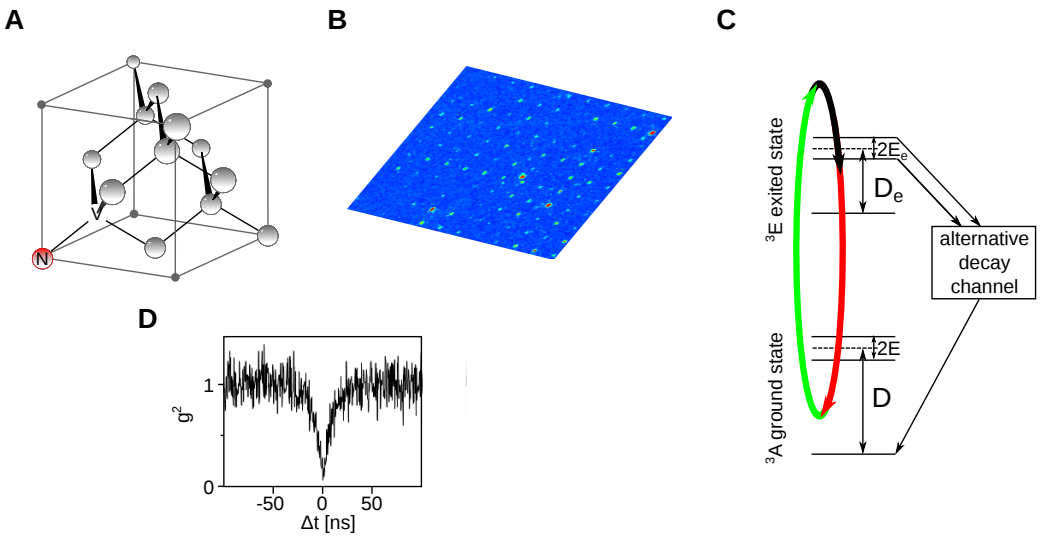

Figure 2.3.: **A** Schematic of the diamond unit cell with an NV center inside. There are four possible directions of the NV axis. The nitrogen could substitute the carbon atom of each lattice site around the vacancy. **B** Confocal scan over a diamond area where NV centers are implanted in a regular pattern. Only few feature more than one color center (red dots). **C** Level structure of the NV center at zero magnetic field. The ZFS in the ground state is $D = 2.87\,\mathrm{GHz}$, E varies between 0 and 5 MHz in bulk diamond. In the excited state $D_\mathrm{e} = 1.42\,\mathrm{GHz}$, E_e varies similar to E. **D** Exemplary measurement data of the g^2 function confirming that only a single emitter resides in the confocal volume.

700 nm. Because the C_{3v} symmetry groups irreducible representation is ^{3}A, ^{1}A and E, there has to be an additional singlet state, which has not been observed experimentally. It probably plays a role in the additional decay channel from the excited to the ground state. The dwell times in the excited state for this relaxation process are spin dependent. For $|\pm 1_\mathrm{e}\rangle$ it is 12 ns, for $|0_\mathrm{e}\rangle$ 170 ns. The dwell time in the alternative decay channel is 150 ns. From there the system relaxes into the $|0_\mathrm{e}\rangle$ ground state. This nonradiative decay process quenches the fluorescence of the NV. Because the transition from $|0_\mathrm{e}\rangle$ is negligible against the $|\pm 1_\mathrm{e}\rangle$ the fluorescence intensity of the NV is spin state dependent. This allows the optical detection of magnetic resonance (ODMR). If a microwave frequency alternating magnetic field hits the NV's spin transition while pumping the system with the green laser the fluorescence intensity drops 30 %. Thus by tuning the microwave frequency the magnetic resonance spectrum can be detected. Although the system can not be excited resonantly

at room temperature but via its phononic side band the cycling transition is nontheless spin conserving [36]. With an excited state radiative lifetime of about 12 ns the NV center is a very brightly fluorescing defect which allows optical detection on a single defect level. To prove that only one NV center resides within a confocal spot the g^2 autocorrelation function is measured by a standard Hanbury Brown and Twiss setup [41, 16]. At time delay $\Delta t = 0$ the autocorrelation function is

$$g^2(0) = \frac{\langle n\,(n-1)\rangle}{\langle n\rangle^2} \tag{2.1}$$

with n the photon number. For classical light $g^2(0) \geq 1$, for coherent light (e.g. laser light) $g^2(\Delta t = 0) = 1$ and for a single emitter $g^2(\Delta t = 0) = 0$ (fig. 2.3).

To make quantum devices work it is mandatory to be able to produce them deterministically. For NV centers this is possible by implanting nitrogen ions into the diamond [79]. The implantation depth linearly depends on the acceleration voltage with 1.4 nm/keV. There are various techniques e.g. implantation through an AFM tip [80] or an electron beam lithographic mask [93] to increase the lateral resolution of the process. So 5 nm lateral resolution on the surface is feasible. With increasing implantation depth the straggle of the ions increases with 0.46 nm/keV, counteracting the high precision on the surface. In the implantation process the nitrogen ions generate lots of lattice damage in their wake. Diamond is annealed for at least two hours at 800° C in vacuum. Vacancies become mobile at that temperature. Thus NV centers which are stable up to 1200° C form and the remaining vacancies diffuse out of the crystal regenerating the diamond structure. If however the lattice damage was too substantial the area of the diamond graphitizes instead of regenerating the diamond structure. The number of vacancies determines the NV yield after annealing [78]. For deep implanted NV it can be as high as 21 % whereas it is in the order of 1 % for shallow implants. The yield can be increased by implanting additional carbon ions or by electron irradiation.

2.1.1. The NV's Electron Spin Qubit

We utilize the electron spin of the NV_- as our qubit. Normally a small magnetic field along the NV axis is applied to lift the degeneracy between the $m_S = -1$ and $+1$ to allow selective addressing of the two allowed microwave transitions between $m_S = 0$ and $m_S = \pm 1$(fig. 2.3). Because the $m_S = \pm 1$ states can not be distinguished by the ODMR read out scheme the $m_S = 0$ to

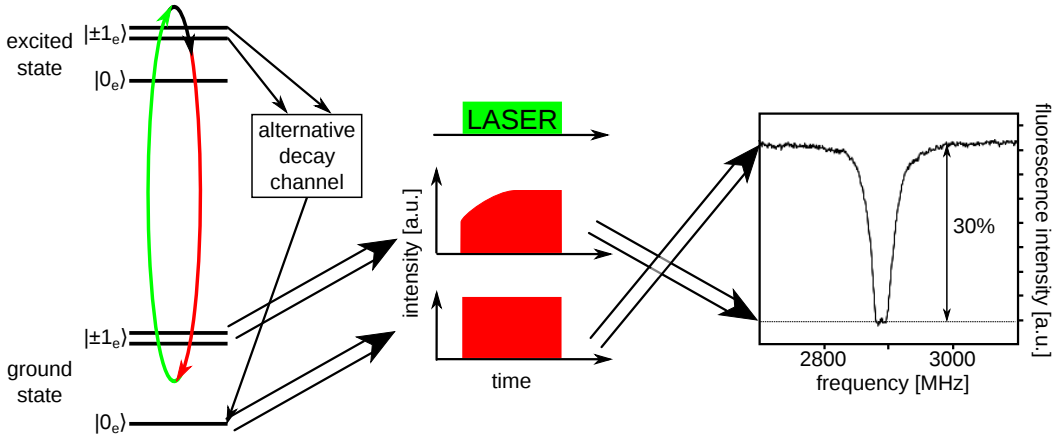

Figure 2.4.: Initialization and read out scheme of the NV center

$m_S = -1$ is normally used as the qubit transition. The system Hamiltonian reads

$$H_{\mathrm{NV}} = \overbrace{D\,(\hat{S}_{\mathrm{z}}^2 - 2/3\,\mathbb{1}) + E\,(\hat{S}_x^2 - \hat{S}_y^2)}^{\text{zero field splitting}} + \overbrace{\frac{\mu_{\mathrm{B}}}{h}\, g_{NV}\, \underline{B}\, \underline{\hat{S}}}^{\text{Zeeman splitting}}\,. \tag{2.2}$$

$D = 2.87\,\mathrm{GHz}$ is the axial zero field splitting (ZFS) parameter due to the dipole-dipole interaction of the 2 unpaired electrons. E denotes the non-axial rhombic ZFS. For all systems with rotational symmetry as the NV E should vanish, but lattice imperfections and impurities lead to distortions of the lattice and thus to a slight breaking of the C_{3v} symmetry, causing up to $E = 5\,\mathrm{MHz}$.

To use a two level system as a qubit one has to be able to initialize it into a known pure state [24]. This is achieved by just shining laser light on the NV. As long as population is left in the $|\pm 1\rangle$ state the system will eventually relax via the secondary decay channel into the $|0\rangle$ state undergoing cycling transitions from there (fig. 2.4) [87].

Single qubit quantum gates are applied by resonant microwave frequency ac magnetic fields that drive Rabi oscillations (see section 3.6) which are truncated after the respective rotation angle is reached. Because the transition to the $m_S = +1$ state is well detuned and the pulse has to be non-selective of eventual hyperfine splitting it can be driven with fairly high mw-powers, allowing gate times in the order of 1 ns [34]. So in an average phase coherence time $T_2 \approx 300\,\mu\mathrm{s}$ single quantum gates are achievable with an error per gate of 1 %. This is sufficient for scalable quantum computing.

In order to read out the final state laser light is applied again. Because the high probability to relax via the lightless alternate decay channel less

photons are emitted if the NV is in the $m_S = \pm 1$ state. The fluorescence intensity is integrated over 2 ms until the system is again polarized into $m_S = 0$ (fig. 2.4). This leads to a 30 % drop in fluorescence intensity if the electron was prepared in $|\pm 1\rangle$. Fluorescence intensities between 100 % ($|0\rangle$) and 70 % ($|\pm 1\rangle$) are linearly corresponding to the mixture of the spin state. Because of the photon shot noise of the laser the signal-to-noise ratio is proportional to the square root of the integration time. The phase coherence can not be measured directly e.g. as transverse magnetization. It has to be transformed into a population difference by a Hadamard gate. So all phase experiments like dynamic decoupling with the NV center have an additional Hadamard gate at the end of the sequence just before the read out laser pulse.

2.1.2. Nuclear Spin Qubits

The electron spin qubit itself is very useful e.g. for metrology of magnetic and electric fields [4, 26] but for quantum communication and information processing a register of qubits is required. Even small registers made up of 3 to 5 qubits can be utilized as nodes of a quantum repeater [52] or as an error corrected meta qubit [89]. To build such a quantum register additional qubits have to be addressed with single qubit gates and connected via two qubit gates to all other qubits in the register. In case of the NV nuclear spins in its near vicinity prove to be a convenient choice. Because only the electron spin qubit can be red out optically the nuclear spin states have to be swapped onto the electron spin for read out. That means only one qubit can be read out at a time because the information on nearly all qubits is scrambled by the laser pulse (see section 7).

^{13}C Nuclear Spin with Exchange Coupling

The most commonly used nuclear spin qubits are ^{13}C in the first or the third shell of carbon sites around the vacancy. They feature a strong hyperfine coupling of 120 MHz (14 MHz) in the first (third) shell due to exchange interaction [35]. Roughly at the the second shell the NV's wave function has a knot. So there is no strong exchange interaction from ^{13}C spins in the second shell. Fig. 2.5 shows some examples of ODMR spectra of NVs with up to three ^{13}C in the first three shells. Carbon spins with exchange coupling add

$$\hat{H}_{^{13}C\mathrm{ex}} = \overbrace{\frac{\mu_\mathrm{n}}{h}\, g_{^{13}C}\, \underline{B}\, \underline{\hat{I}}}^{^{13}C} + \overbrace{\underline{\underline{A}}_{^{13}C}\, \underline{\hat{S}}\, \underline{\hat{I}}}^{\text{exchange interaction}} \tag{2.3}$$

to the system Hamiltonian with $\mu_n/h = 0.76\,\mathrm{kHz/G}$ is the nuclear magnetic moment $g_{^{13}C} = 1.40483$, $\underline{B}$ the magnetic field and $\underline{\underline{A}}$ the isotropic hyperfine interaction tensor. It is assumed to be isotropic (120 MHz and 14 MHz respectively) neglecting the reported anisotropy of $A_{\mathrm{aniso}} = 27\,\mathrm{MHz}$ [35]. There are three lattice sites in the first shell and 16 in the third. So in principle one could have 19 nuclear spin qubits this way. Because all transitions have to be resolved in the ODMR spectrum to address every qubit separately up to 10 qubits at a single NV are possible [18]. Due to the fact that ^{13}C can not be placed deliberately in the lattice it is a probabilistic task to find a NV that features the desired number of nuclear spin qubits. This is getting more and more cumbersome the more ^{13}C are of need especially in isotopically purified diamonds. Thus not more than 3 such qubits have been reported up to now [74, 67] (fig. 2.5).

Single qubit gates are realized by applying a resonant radio frequency (rf) magnetic field on the hyperfine transitions as depicted in fig. 2.5. Because the direct "multi quantum gate"-transitions are forbidden the corresponding rotations are performed on the electron spin qubit and then swapped onto the respective transitions. To incorporate this into a quantum algorithm the initial state of the levels in question has to be swapped onto the NV spin prior to the application of the actual gate. This renders the NV spin an ancilla qubit ideally not contributing to the register other than gating. This is also preferable because the ^{13}C nuclei in the first and third shell feature coherence times around two orders of magnitude longer than the electron spin even at natural ^{13}C abundance. In combination with the comparatively fast gates of few nanoseconds with fidelities up to 98 % they are well suited for scaling up the system. Due to the strong orthogonal hyperfine interaction the quantization axis of the nuclei are tilted against the NV-axis even at aligned magnetic field. It is therefore not possible to achieve single shot readout of these qubits by the present scheme (sec. 7).

One major building block of quantum information processing is the generation of maximally entangled states with a high fidelity. This is demonstrated with a register of the NV electron spin and two carbon nuclear spins [74]. All four Bell states

$$\Phi^{\pm} = \frac{1}{\sqrt{2}} \left(|00\rangle \pm |11\rangle\right) \tag{2.4}$$

$$\Psi^{\pm} = \frac{1}{\sqrt{2}} \left(|01\rangle \pm |10\rangle\right) \tag{2.5}$$

are generated on the two nuclear spin qubits (qubit 1 and 2), the states tomographed and their phase coherence time is measured. From the tomogram the

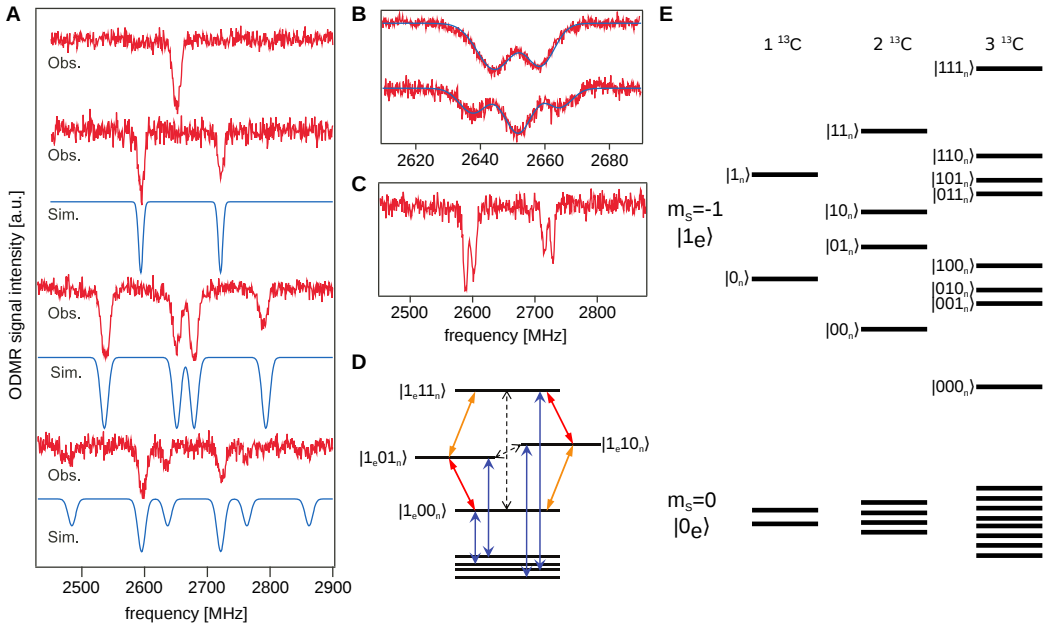

Figure 2.5.: **A** ODMR spectra of the hyperfine splitting of zero to three (top to bottom) ^{13}C in the first shell. The blue solid lines are simulated by exact diagonalization of the system Hamiltonian. **B** ODMR spectra of one/two ^{13}C in the third shell and **C** one in the first and one in the third shell. **D** shows a schematic of the allowed transitions of the microwave (blue) and radio frequency (orange and red) for two ^{13}C qubits. The orange arrows indicate the single qubit gate transitions of ^{13}C qubit one, red for two. Gates on the forbidden transitions are generated by combined pulses on allowed transitions. **E** Schematic of the NV's level structure with up to 3 ^{13}C. Because the spin quantum number is no good quantum number in the energy eigenbasis the levels are named in binary to emphasize the qubit character. Note that $|011_n\rangle$ and $|100_n\rangle$ are not in the counting order to indicate that one (two) physical spins have been flipped.

fidelity, concurrence and the eigenvalues of the partial transpose are calculated as an entanglement measure. The quantum circuit to generate the Φ^- state among the two nuclear spin qubits is depicted in fig. 2.6. First the system is initialized by optical pumping. Only the electron spin is initialized that way, the nuclear spins remain in the totally mixed state. By the initial CCNOT gate $|00_n\rangle$ is subselected. All other nuclear spin states do not contribute to the signal. Thus the measured contrast is reduced to 1/4. For enhanced contrast

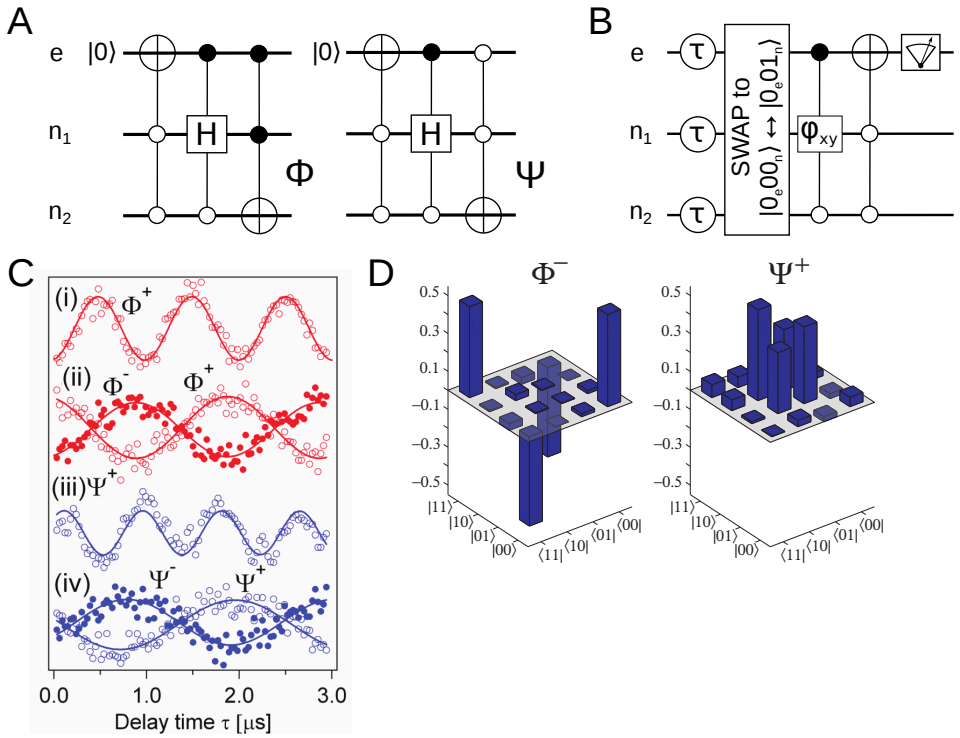

Figure 2.6.: **A** Quantum circuits to generate the Bell states. Replacement of the $\pi/2$ rotation of the controlled Hadamard gate by a $3\,\pi/2$ rotation results in the respective + state. **B** Tomography circuit for an arbitrary 3 qubit state. φ_{xy} denotes a $\pi/2_{\mathrm{x}}$, $\pi/2_{\mathrm{y}}$, π_x or no pulse respectively. **C** The chosen frequency offsets and fitted frequency ω_{fit} of the Ramsey fringes in MHz are (I) $\Delta\omega_1 = \Delta\omega_2 = 0.5$, $\omega_{\mathrm{fit}} = 1.0$, (II) $\Delta\omega_1 = 0$, $\Delta\omega_2 = 0.5$, $\omega_{\mathrm{fit}} = 0.5$, (III) $\Delta\omega_1 = -0.3$, $\Delta\omega_2 = 1.0$, $\omega_{\mathrm{fit}} = 1.3$, (IV) $\Delta\omega_1 = 0$, $\Delta\omega_2 = 0.4$, $\omega_{\mathrm{fit}} = 0.4$. All fitting the expected frequencies. **D** exemplary state tomogram of the Φ^- and the Ψ^+ state.

the nuclear spins can in principle be polarized before the algorithm [29, 49]. Because the direct transition $|1_{\mathrm{e}}00_{\mathrm{n}}\rangle \leftrightarrow |1_{\mathrm{e}}11_{\mathrm{n}}\rangle$ is forbidden the generation of the Bell state is split into two gates. First a controlled Hadamart gate (one controlled by the electron qubit zero controlled by qubit 2) on qubit 1 generates an equal superposition state which is swapped by a Toffoli gate onto the

$|1_e 00_n\rangle \leftrightarrow |1_e 11_n\rangle$ transition

$$\begin{aligned}
&\frac{1}{4}\,|0_e 00_n\rangle\langle 0_e 00_n| + |0_e 01_n\rangle\langle 0_e 01_n| + |0_e 10_n\rangle\langle 0_e 10_n| + |0_e 11_n\rangle\langle 0_e 11_n| \\
&\xrightarrow{\mathrm{CCNOT_e}} |1_e 00_n\rangle \xrightarrow{\mathrm{CH_{n1}}} \frac{1}{\sqrt{2}}\left(|1_e 00_n\rangle + |1_e 01_n\rangle\right) \\
&\xrightarrow{\mathrm{CCNOT_{n2}}} \frac{1}{\sqrt{2}}\left(|1_e 00_n\rangle - |1_e 11_n\rangle\right).
\end{aligned} \tag{2.6}$$

The other Bell states are generated in an analog fashion.

In order to analyze the generated states a full state tomography is carried out. It relies on the phase dependence of the entangled state. If like in the FID experiment (sec. 3.7) the state is generated by slightly detuned radio frequency fields ($\Delta\omega_1$, $\Delta\omega_2$) in the rotating frame the state precesses with the detuning frequency about the quantization axis (z-direction) after the pulse. The corresponding Hamiltonian is

$$\hat{H} = \Delta\omega_1\,\hat{I}_{z1} + \Delta\omega_2\,\hat{I}_{z2}. \tag{2.7}$$

It leads to a time evolution operator

$$U_z = \mathrm{e}^{-\mathrm{i}\,\hat{H}\,\tau} = \mathrm{e}^{-\mathrm{i}\,(\Delta\omega_1\,m_{I1} + \Delta\omega_1\,m_{I2})\,\tau} \tag{2.8}$$

This is equivalent to the acquisition of a global phase $\vartheta(m_{I1}, m_{I2}) = \Delta\omega_1\,m_{I1} + \Delta\omega_1\,m_{I2}$. Because of the dependence on the quantum numbers m_I the resulting phases $\varphi = \vartheta(m'_{I1}, m'_{I2}) - \vartheta(m_{I1}, m_{I2})$ of different entangled states evolve differently

$$\varphi_\Phi = \vartheta(1/2, 1/2) - \vartheta(-1/2, -1/2) = (\Delta\omega_1\,m_{I1} + \Delta\omega_1\,m_{I2})\,\tau \tag{2.9}$$

$$\varphi_\Psi = \vartheta(1/2, -1/2) - \vartheta(-1/2, 1/2) = (\Delta\omega_1\,m_{I1} - \Delta\omega_1\,m_{I2})\,\tau \tag{2.10}$$

The + and - states are discriminated by their π-phase difference. Results shown in fig. 2.6 are precisely matching the expected frequencies. The T_2^* times of the coherence is measured this way. It turned out that is limited by the $T_1 \approx 8\,\mathrm{ms}$ time of the electron spin. For the actual tomography the expectation values of all basis operators have to be measured. Because we are only able to read out the NV's electron spin we have to do the full tomography successive transition after transition swapping them onto a "working transition". We choose the $|1_e 00_n\rangle \leftrightarrow |1_e 01_n\rangle$ in this case. For a TLS the basis operators are $\hat{\sigma}_x$, $\hat{\sigma}_y$, $\hat{\sigma}_z$, $\hat{\sigma}_{\mathbb{1}}$. To precisely measure their expectation values Rabi oscillations by π phase shifted radio frequencies (x-, y driving field) are recorded. After a $\pi/2_{xy}$-pulse

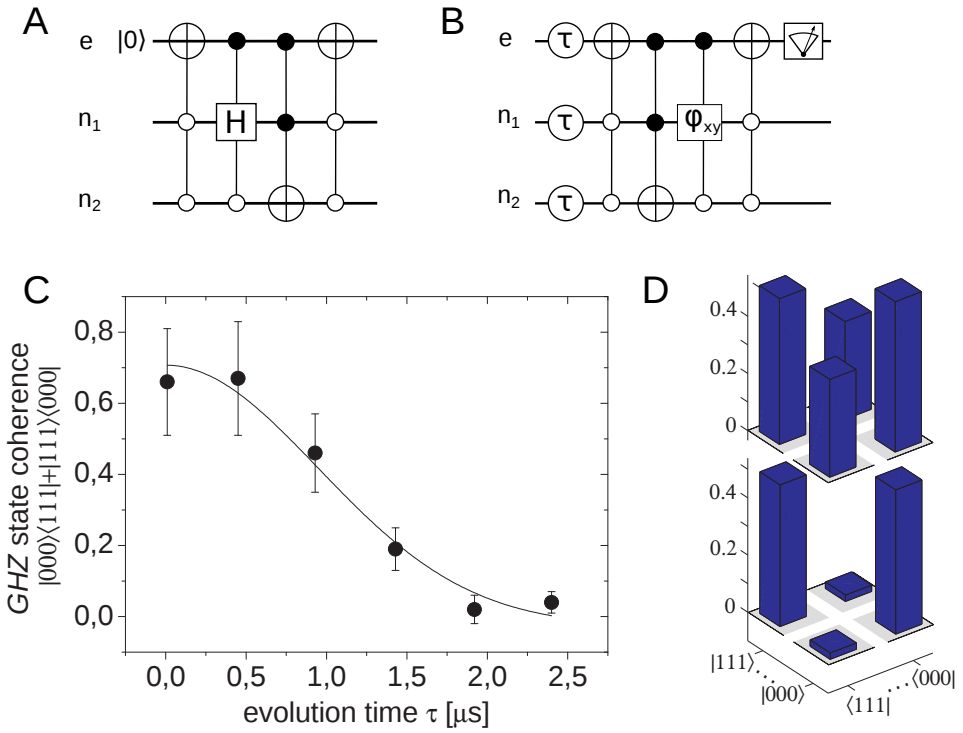

Figure 2.7.: **A** Quantum circuits to generate the GHZ state. **B** Tomography circuit for the four ideally nonzero entries of the GHZ density operator. It follows the same ideas as for the Bell states. **C** FID of the GHZ state showing the sum of the off diagonal entries $\rho_{18}^{\mathrm{GHZ}} + \rho_{81}^{\mathrm{GHZ}}$. The fitted decay $\exp[-(\tau/T_2^*)^2]$ yields $T_2^* = 1.3 \pm 0.2\,\mu$s. **D** state tomogram of the relevant matrix elements at $\tau = 0\,\mu$s on top and $\tau = 2.4\,\mu$s at the bottom. The off diagonal elements have decayed completely by then.

the measured value represents the expectation value $\hat{\sigma}_{\mathrm{x}}$, $\hat{\sigma}_{\mathrm{y}}$. The "no pulse" expectation value together with a π-pulse determine the $\hat{\sigma}_{\mathrm{z}}$, $\hat{\sigma}_{\mathbb{1}}$ values. from the full density matrix (fig. 2.7) we deduce the fidelity as well as the concurrence and the negative partial transpose of all four bell states

Bell state	Fidelity	Concurrence	Partial transpose
Ψ^+	0.80 ± 0.07	$0.65^{+0.15}_{-0.08}$	$-0.31^{+0.06}_{-0.05}$
Ψ^-	0.81 ± 0.06	0.65 ± 0.11	$-0.32^{+0.06}_{-0.05}$
Φ^+	0.98 ± 0.05	$0.96^{+0.09}_{-0.04}$	$-0.49^{+0.05}_{-0.04}$
Φ^-	0.96 ± 0.05	$0.92^{+0.08}_{-0.07}$	-0.47 ± 0.46

To demonstrate tripartite entanglement a Greenberger–Horne–Zeilinger (GHZ)

state [39] and the W state [28] were generated and analyzed. The GHZ state

$$|GHZ\rangle = \frac{1}{\sqrt{2}} \left(|000\rangle + \mathrm{e}^{\mathrm{i}\,\phi}\ |111\rangle\right) \tag{2.11}$$

with ϕ an arbitrary phase is the multi qubit analogon to the Bell states. It features threefold entanglement only. If one qubit is lost we are left with

$$\mathrm{tr}_3 \left\{ \frac{1}{2}\ \left(|000\rangle + |111\rangle\right)\ \left(\langle 000| + \langle 111|\right) \right\} = \frac{1}{2} \left(|00\rangle \langle 00| + |11\rangle \langle 11|\right) \tag{2.12}$$

which is a mixed state with no remaining entanglement. If the "lost" qubit was measured by a projective measurement the remaining state would be projected into a pure state $|00\rangle$ or $|11\rangle$ according to the measurement outcome. Although there exists no standard measure of multipartide entanglement the GHZ state is considered maximally entangled because of its analogy to the Bell states. Starting from the generation of the Φ^+ state the GHZ state is prepared by an additional CCNOT gate that swaps the coherence of the $|1_\mathrm{e}00_\mathrm{n}\rangle \leftrightarrow |1_\mathrm{e}11_\mathrm{n}\rangle$ to the $|0_\mathrm{e}00_\mathrm{n}\rangle \leftrightarrow |1_\mathrm{e}11_\mathrm{n}\rangle$ transition (fig. 2.7). Because the fidelity of a pure state depends only on the density operator entries that are nonzero in the goal operator it is sufficient to do a matrix tomography only for those matrix elements (fig. 2.7). We achieved the fidelity $F = 0.87 \pm 0.06$ with the phase coherence time of $T_2^* = 1.3 \pm 0.2\,\mu\mathrm{s}$.

Another maximally entangled three qubit state is the W state

$$|W\rangle = \frac{1}{\sqrt{3}} \left(|110\rangle + \mathrm{e}^{\mathrm{i}\,\phi}\ |101\rangle + \mathrm{e}^{\mathrm{i}\,\theta}\ |011\rangle\right). \tag{2.13}$$

It features bipartite entanglement between all pairs of qubits but the three-tangle vanishes. Thus it is fundamentally different from the GHZ state. If one qubit is lost, regardless whether it was measured or it just rapidly dephased, the remaining system is still entangled. The GHZ state and the W state represent the two non biseparable classes of three qubit states that can not be transformed into one another by local quantum operations not even by local projections. The generation is a little more complicated than for the Bell and GHZ states because the coherence has to be distributed among several transitions. In order to generate a 1/3 to 2/3 distribution a 2 $\arccos\sqrt{2/3}$ pulse is applied on the $|1_\mathrm{e}10_\mathrm{n}\rangle \leftrightarrow |1_\mathrm{e}11_\mathrm{n}\rangle$ transition. Then half of the remaining population (2/3) of the $|1_\mathrm{e}11_\mathrm{n}\rangle$ level is transfered to $|1_\mathrm{e}01_\mathrm{n}\rangle$. The system is now in the state $1/\sqrt{3}\,(|1_\mathrm{e}10_\mathrm{n}\rangle + |1_\mathrm{e}11_\mathrm{n}\rangle + |1_\mathrm{e}01_\mathrm{n}\rangle)$. Finally the $|1_\mathrm{e}11_\mathrm{n}\rangle$ population is swapped onto $|0_\mathrm{e}11_\mathrm{n}\rangle$ by a microwave π pulse completing the W state (fig. 2.8). The state tomography of the three relevant transitions revealed a fidelity of $F = 0.85^{+0.05}_{-0.1}$. The T_2^* times are

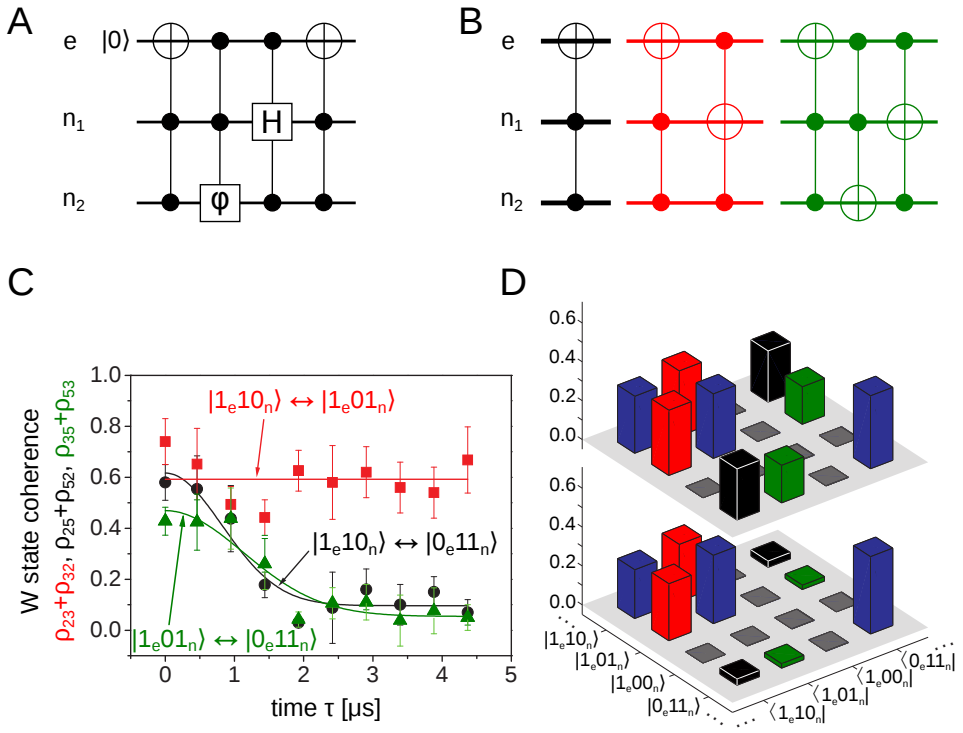

Figure 2.8.: **A** Quantum circuits to generate the W state. $\varphi = 2 \arccos \sqrt{2/3}$ to distribute the entanglement equally on all three states. **B** Schemes to swap the state of the three relevant transitions on the working transition $|1_e10_n\rangle \leftrightarrow |1_e11_n\rangle$. The color code corresponds to subfigure C and D. **C** FID of the three coherences. $\exp\{-(\tau/T_2^*)^2\}$ yields $T^*_{2\,23} = 1.6 \pm 0.3\,\mu$s and $T^*_{2\,25} = 1.2 \pm 0.3\,\mu$s. In ρ_{35}^{W} the NV's electron spin is not involved so the coherence time is limited by the electrons T_1 as at the Bell states. It does not decay at all over the observation time. The red horizontal line is a guide to the eye. **D** state tomogram of the relevant matrix elements at $\tau = 0\,\mu$s on top and $\tau = 4.4\,\mu$s at the bottom. The gray entries have not been measured.

Transition	T_2^*
$\|1_e10_n\rangle \leftrightarrow \|0_e11_n\rangle$	$1.2 \pm 0.2\,\mu$s
$\|1_e01_n\rangle \leftrightarrow \|0_e11_n\rangle$	$1.6 \pm 0.3\,\mu$s
$\|1_e10_n\rangle \leftrightarrow \|1_e01_n\rangle$	$\gg 2\,\mu$s.

Because the electron spin qubit is not involved in the $|1_e10_n\rangle \leftrightarrow |1_e01_n\rangle$ coherence it shows no decay at all on the measured time scale up to $4.4\,\mu$s. Its T_2^* time is as the Bell states rather limited by the $T_1 \approx 8\,$ms time of the NV spin.

Dipole-Dipole Coupled Carbon Nuclear Spins

Most carbon spins in the lattice have no exchange interaction with the NV, they couple via dipole-dipole interaction. Normally the axial components of these interactions are distributed so densely that they do not split the line. So those ^{13}C spins are not feasible as a qubit but contribute to inhomogeneous line broadening. If however the ^{13}C density is very low the inhomogeneous line width $\Delta\omega = 2\,\pi/T_2^*$ eventually reaches the order of 50 kHz and below (sec. 5). In this regime the strongest interacting carbon spins split the line and thus become addressable as qubits. The part of the system Hamiltonian corresponding to such a qubit is

$$\hat{H}_{^{13}C} = \overbrace{\frac{\mu_\mathrm{n}}{h}\, g_{^{13}C}\, \underline{B}\, \underline{\hat{I}}}^{^{13}C} - \overbrace{\frac{\mu_0}{2\,\hbar}\frac{\mu_\mathrm{B}\,\mu_\mathrm{n}\, g_\mathrm{NV}\, g_{^{13}C}}{|\underline{r}|^3}\left(\frac{3(\underline{\hat{S}}\,\underline{r})\,(\underline{\hat{I}}\,\underline{r})}{|\underline{r}|^2} - \underline{\hat{S}}\,\underline{\hat{I}}\right)}^{\text{dipole-dipole interaction}} \tag{2.14}$$

with μ_0 the permeability of free space, μ_B (μ_n) the Bohr (nuclear) magneton and g_NV ($g_{^{13}C}$) the electron (^{13}C) g-factor. $\underline{r}$ is the vector connecting the NV and the ^{13}C site.

Two qubit gates of dipole-dipole coupled nuclei and the NV electron spin are comparatively slow in the order of μs. Even with $T_2^* \approx 25$ ms at natural abundance this does not allow scaling of the register. Due to the weak coupling to the NV center at sufficiently high magnetic fields the quantization axis of such qubits is not deviated from the the magnetic field direction in first order. This should allow single shot read out on those spins (sec. 7).

Nitrogen Nuclear Spin

A nuclear spin that is always present is the one of the nitrogen atom. It has two stable isotopes ^{14}N and ^{15}N. 99.63 % of the natural occurrence is ^{14}N. It has nuclear spin $\hat{I} = 1$ whereas ^{15}N has $\hat{I} = 1/2$. The nitrogen nuclear spin is represented by

$$\hat{H}_{^iN} = \overbrace{Q\,\hat{I}_z^2 + \frac{\mu_\mathrm{n}}{h}\, g_{^iN}\, \underline{B}\, \underline{\hat{I}}}^{\text{nitrogen}} + \overbrace{A_{^iN}\, \underline{\hat{S}}\, \underline{\hat{I}}}^{\text{exchange interaction}} \tag{2.15}$$

in the Hamiltonian of the quantum register. The operators $\underline{\hat{I}}$ are chosen according to the isotope involved. Here $g_{^iN} = 0.4038$ (-0.5600) is the gyro magnetic ratio of ^{14}N (^{15}N). $A_{^iN} = 2.3$ MHz is the isotropic hyperfine coupling strength with the NV. The zero field splitting $Q = -5.04$ MHz of the ^{14}N

nucleus [96] originates from the nuclear quadrupole tensor induced by electric field gradients at the nitrogen location. Because the nitrogen spin is located on the NV's symmetry axis this tensor is assumed to be parallel to the NV axis. So the nitrogen nuclear spins quantization axis is always parallel to the NV's as long as the magnetic field is oriented in the same direction as well. This will prove to be a very important feature later on (sec. 7).

Because in the ground state the NV's wave function has next to no amplitude [35] at the nitrogen atom the exchange interaction is only 2.3 kHz. Thus gates with the nitrogen nuclear spin are comparatively slow in the order of a few μs.

3. Basic Quantum Mechanics

3.1. Operator Representations

In order to describe a quantum mechanic system one can not rely on the classical phase space but has to use the eigenvalues of Hermitian operators. Their representation is defined according to an appropriate frame of reference. These are called operator representations. They form a basis of the corresponding Hilbert space. Therefore all basis operators $\hat{B}$ have to be pairwise linear independent. Normally they are chosen to be orthonomal

$$\mathrm{tr}[\hat{B}_i^\dagger \hat{B}_j] = 0 \tag{3.1}$$

$$\mathrm{tr}[\hat{B}_i^\dagger \hat{B}_i] = 1 \tag{3.2}$$

for all i, j. In general the choice of the basis is arbitrary and can be adapted to the problem at hand (see sec. 3.4). The experiment however imposes a certain basis on the system, the energy eigenbasis in spectroscopy or a rotating frame for phase experiments like dynamic decoupling, quantum computing or quantum metrology (sec. 3.7). Some of the more common representations, relevant for this thesis are presented in the following section.

3.1.1. Transition Operator Representation

If one is interested in a discrete finite k-dimensional Hilbert space $\mathcal{H}$ it can be described in the complete orthogonal state basis $|i\rangle$ with

$$\langle i|\, j\rangle = \delta_{ij} \qquad \text{with } i, j = 1, 2, \ldots, k. \tag{3.3}$$

we can now define k^2 transition operators

$$\hat{P}_{ij} = |i\rangle \langle j| \tag{3.4}$$

which in general are non-Hermitian but nevertheless orthonormal

$$\mathrm{Tr}\, \hat{P}_{ij} \hat{P}^\dagger_{i'j'} = \delta_{ii'}\delta_{jj'} \tag{3.5}$$

if the trace operation Tr ... is used to calculate the norm, this is called tracenorm.

The transition operators form a complete basis in the accounting Liouville space $\mathcal{L}$ [37]. All Operators $\hat{O}$ can be expanded into this basis

$$\hat{O} = \sum_{ij} O_{ij} \hat{P}_{ij}, \tag{3.6}$$

where the O_{ij} are the expansion coefficients

$$O_{ij} = \mathrm{Tr}\{\hat{O}\hat{P}_{ij}^{\dagger}\} = \langle i| \hat{O} |j\rangle \tag{3.7}$$

This makes a total of $2k^2$ parameters due to the fact that coefficients O_{ij} in general are complex. In case of a Hermitian operator all O_{ij} are real because

with $\hat{O} = \hat{O}^{\dagger}$ and $\hat{P}_{ij} = \hat{P}_{ij}^{\dagger}$

$$\hat{O} = \sum_{ij} O_{ij} \hat{P}_{ij} \tag{3.8}$$

$$\hat{O}^{\dagger} = \sum_{ij} O_{ij}^{*} \hat{P}_{ij}^{\dagger} \tag{3.9}$$

$$\Rightarrow \; O_{ij} = O_{ij}^{*}. \tag{3.10}$$

So we need k^2 coefficients O_{ij} to define a Hermitian operator uniquely.

3.1.2. Generators of the SU

It is convenient, especially for spin systems, to use the generators of the SU(k) as a complete orthogonal basis of the Hilbert space. They are therefore often called spin operators. For $k = 2$ these are the Pauli operators $\hat{\sigma}_i$ with $i =$ x, y, z, 0. In terms of transition operators the Pauli operators are

$$\hat{\sigma}_{\mathrm{x}} = \hat{P}_{12} + \hat{P}_{21}, \tag{3.11}$$

$$\hat{\sigma}_{\mathrm{y}} = \mathrm{i}\,(\hat{P}_{21} - \hat{P}_{12}), \tag{3.12}$$

$$\hat{\sigma}_{\mathrm{z}} = \hat{P}_{11} - \hat{P}_{22}, \tag{3.13}$$

$$\hat{\sigma}_{0} = \mathbb{1}_2. \tag{3.14}$$

They are Hermitian and, except $\hat{\sigma}_0$, traceless. Some important relations for the Pauli operators are

$$(\hat{\sigma}_i)^2 = \mathbb{1}_2, \tag{3.15}$$

$$[\hat{\sigma}_{\mathrm{x}}, \hat{\sigma}_{\mathrm{y}}] = 2\mathrm{i}\hat{\sigma}_{\mathrm{z}}, \tag{3.16}$$

and cyclic permutations of (3.16). Additionally, raising and lowering operators

$$\hat{\sigma}+ = \hat{\sigma}_\mathrm{x} + \mathrm{i}\,\hat{\sigma}_\mathrm{y} \tag{3.17}$$

$$\hat{\sigma}- = \hat{\sigma}_\mathrm{x} - \mathrm{i}\,\hat{\sigma}_\mathrm{y} \tag{3.18}$$

can be introduced. For $k > 3$ the operators that generate rotations about the spacial directions do not form a full basis anymore. Nonetheless they are very useful to set up a spin Hamiltonian in the laboratory frame. The operators that complete the basis can be found as products of these "Cartesian" rotations. For $k = 3$ the generators of these rotations are

$$\hat{S}_\mathrm{x} = \hat{P}_{12} + \hat{P}_{12} + \hat{P}_{13} + \hat{P}_{31} \tag{3.19}$$

$$\hat{S}_\mathrm{y} = \mathrm{i}\,(\hat{P}_{21} - \hat{P}_{12} + \hat{P}_{31} - \hat{P}_{13}) \tag{3.20}$$

$$\hat{S}_\mathrm{z} = \hat{P}_{33} - \hat{P}_{11}. \tag{3.21}$$

The operators completing the basis are $\hat{S}_\mathrm{x}^2$, $\hat{S}_\mathrm{y}^2$, $\hat{S}_\mathrm{z}^2$, $\hat{S}_\mathrm{x}\,\hat{S}_\mathrm{y}$, $\hat{S}_\mathrm{y}\,\hat{S}_\mathrm{x}$,and $\mathbb{1}_3$. The Gell Mann matrices also generate the SU(3) but they do not feature the rotations about the Cartesian coordinates which makes them undesirable for spin Hamiltonians. We use $\hat{I}_i$ to denote the spin operators of nuclear spins with the respective dimension.

3.2. The Density Operator

Probably the most versatile way to describe an arbitrary quantum state is by the density operator $\hat{\rho}$. Its matrix representation is given by

$$\hat{\rho} = \sum_{i,j=1}^{k} \rho_{ij}\,\hat{P}_{ij}. \tag{3.22}$$

In order to describe a real quantum system, $\hat{\rho}$ is subject to the condition

$$\mathrm{Tr}\,\hat{\rho} = \sum_i \rho_{ii} = 1 \tag{3.23}$$

and has to be a positive definite Hermitian operator. The matrix elements can be projected out again with the aid of the state vectors

$$\rho_{ij} = \langle i|\,\hat{\rho}\,|j\rangle\,. \tag{3.24}$$

The expectation value of an arbitrary operator $\hat{O}$ for the state $\hat{\rho}$ is given by

$$\left\langle \hat{O} \right\rangle = \mathrm{Tr}\,\hat{O}\,\hat{\rho}. \tag{3.25}$$

3.2.1. Composite Quantum Systems

If the system of interest is composed of several interacting spin systems the Hamiltonian of the i^{th} subsystem $\hat{H}_{\text{i}}^{\text{iso}}$ is incorporated by multiplying $\mathbb{1}_d$ of sufficient dimension

$$d_{\text{b}} = \prod_{k=1}^{i-1} \dim(\hat{H}_k) \tag{3.26}$$

$$d_{\text{a}} = \prod_{k=i+1}^{n} \dim(\hat{H}_k) \tag{3.27}$$

by a dyadic product

$$\hat{H}_{\text{i}}^{\text{sys}} = \mathbb{1}_{d_{\text{b}}} \otimes \hat{H}_{\text{i}}^{\text{iso}} \otimes \mathbb{1}_{d_{\text{a}}}. \tag{3.28}$$

Interaction between two subsystems (i, j) is written

$$\hat{H}_{\text{ij}}^{\text{int}} = \sum_{\{l,m\}=\{\text{x,y,z}\}} \lambda_{ij\,lm} \hat{S}_{il}\, \hat{S}_{jm}. \tag{3.29}$$

For convenience the indices of the system ij are omitted.

Because (3.23) holds true for all subsystems the state of a single subsystem can be determined by applying the partial trace operation on all other subsystems

$$\hat{\rho}_i^{\text{iso}} = \text{tr}_{\{\mathbb{N}<g\setminus i\}} \hat{\rho} = \sum_{v=\{\mathbb{N}<g\setminus i\}} \sum_{w=1}^{k_v} \prod_{j=1}^{k} \hat{\rho}_{ww}^{j} \tag{3.30}$$

with g the number of subsystems. All correlations to other subsystems are lost. So only for a factorizeable state holds

$$\hat{\rho} = \prod_i \hat{\rho}_i^{\text{iso}}. \tag{3.31}$$

3.3. Dynamics of Closed Quantum Systems

According to quantum mechanics the time dependence of a state $\Psi(t)$ is given by the Schrödinger equation

$$\text{i}\,\hbar \frac{\text{d}}{\text{d}t} \left|\Psi(t)\right\rangle = \hat{H} \left|\Psi(t)\right\rangle. \tag{3.32}$$

A formal solution to this equation is given by the unitary time evolution operator

$$|\Psi(t)\rangle = \hat{U}(t, t_0)\ |\Psi(t_0)\rangle\,. \tag{3.33}$$

It only depends on the initial time t_0, t and the system's Hamiltonian. Substituting (3.33) in the Schrödinger equation (3.32) we get the time dependence of $\hat{U}(t, t_0)$

$$\mathrm{i}\,\hbar\,\frac{\partial}{\partial t}\,\hat{U}(t, t_0) = \hat{H}\,\hat{U}(t, t_0). \tag{3.34}$$

If $\hat{H}$ is time independent we are able to integrate this equation of motion

$$\hat{U}(t, t_0) = \mathrm{e}^{-\frac{\mathrm{i}}{\hbar}\hat{H}(t-t_0)}. \tag{3.35}$$

If the initial state is not a pure state it is reasonable to use the density matrix formalism to keep track of the system's state

$$\hat{\rho}(t_0) = \sum_{ij} p_{ij}\ |\Psi_i(t_0)\rangle\,\langle\Psi_j(t_0)|\,. \tag{3.36}$$

Using the time evolution operator (3.33) gives us

$$\hat{\rho}(t) = \sum_i w_i\,\hat{U}(t, t_0)\ |\Psi_i(t_0)\rangle\,\langle\Psi_i(t_0)|\ \hat{U}(t, t_0)^\dagger = \hat{U}(t, t_0)\,\hat{\rho}(t_0)\,\hat{U}(t, t_0)^\dagger. \tag{3.37}$$

After differentiating this equation [15] one eventually finds the Liouville von Neumann equation

$$\frac{\mathrm{d}\,\hat{\rho}}{\mathrm{d}t} = -\frac{\mathrm{i}}{\hbar}\,[\hat{H}, \hat{\rho}]. \tag{3.38}$$

3.4. Pictures of Quantum mechanics

In the Schrödinger picture the dynamics of the state $\hat{\rho}(t)$ are governed by the Liouville von Neumann equation (3.38). An equivalent description is the so called Heisenberg picture where the Hilbert space operators $\hat{A}_\mathrm{H}(t)$ undergo the time evolution instead of the density matrix. The density operator $\hat{\rho}_\mathrm{H}$ stays constant in time. It is assumed that at the initial time t_0 the quantum state of both pictures coincides $\hat{\rho}(t_0) = \hat{\rho}_\mathrm{H}$. Note that the Heisenberg picture operators

are indicated by an index H. The operators of both pictures are connected via the time evolution operator

$$\hat{A}_{\mathrm{H}}(t) = \hat{U}(t,t_0)^{\dagger}\,\hat{A}(t)\,\hat{U}(t,t_0). \tag{3.39}$$

Note that the $\hat{A}_{\mathrm{H}}(t)$ rotates exactly in the counter direction of $\hat{\rho}(t)$ in the Schrödinger picture. Expectation values of a given operator $\hat{A}$ are the same in either picture

$$\langle\hat{A}(t)\rangle = \mathrm{tr}\{\hat{A}(t)\,\hat{\rho}(t)\} = \mathrm{tr}\{\hat{A}_{\mathrm{H}}(t)\,\hat{\rho}_{\mathrm{H}}\}. \tag{3.40}$$

With (3.38) and the transformation relation (3.39) it is straightforward to derive the equation of motion in the Heisenberg picture

$$\frac{\mathrm{d}\,\hat{A}_{\mathrm{H}}(t)}{\mathrm{d}t} = -\frac{\mathrm{i}}{\hbar}\,[\hat{H}_{\mathrm{H}}(t), \hat{A}_{\mathrm{H}}(t)] + \frac{\partial\,\hat{A}_{\mathrm{H}}(t)}{\partial t}. \tag{3.41}$$

The Schrödinger and the Heisenberg picture form the extremal cases of a third picture, called the interaction picture. To derive this we have to separate the Hamiltonian into two parts

$$\hat{H}(t) = \hat{H}_0 + \hat{H}_{\mathrm{I}}. \tag{3.42}$$

In general $\hat{H}_0$ gives the energies of the subsystems neglecting the interaction between them. Usually this part is time independent. $\hat{H}_{\mathrm{I}}$ describes the interaction between the subsystems. We now introduce two partial time evolution operators

$$\hat{U}_0(t,t_0) = \mathrm{e}^{-\frac{\mathrm{i}}{\hbar}\hat{H}_0(t-t_0)} \tag{3.43}$$

$$\hat{U}_{\mathrm{I}}(t,t_0) = \mathrm{e}^{-\frac{\mathrm{i}}{\hbar}\hat{H}_{\mathrm{I}}(t-t_0)} = \hat{U}_0^{\dagger}(t,t_0)\,\hat{U}(t,t_0). \tag{3.44}$$

Now the time evolution of the expectation value of $\hat{A}(t)$ can be written as

$$\begin{aligned}\langle\hat{A}(t)\rangle &= \mathrm{tr}\{\hat{U}_0^{\dagger}(t,t_0)\,\hat{A}(t)\,\hat{U}_0(t,t_0)\,\hat{U}_{\mathrm{I}}(t,t_0)\,\hat{\rho}(t)\,\hat{U}_{\mathrm{I}}^{\dagger}(t,t_0)\} \\ &= \mathrm{tr}\{\hat{A}_{\mathrm{I}}(t)\,\hat{\rho}_I(t)\}\end{aligned} \tag{3.45}$$

with $\hat{A}_{\mathrm{I}}(t) = \hat{U}_0^{\dagger}(t,t_0)\,\hat{A}(t)\,\hat{U}_0(t,t_0)$ and $\hat{\rho}_I(t) = \hat{U}_{\mathrm{I}}(t,t_0)\,\hat{\rho}(t)\,\hat{U}_{\mathrm{I}}^{\dagger}(t,t_0)$ the operators in the interaction picture. The equation of motion takes the form

$$\frac{\mathrm{d}\,\hat{\rho}_{\mathrm{I}}(t)}{\mathrm{d}t} = -\frac{\mathrm{i}}{\hbar}\,[\hat{H}_{\mathrm{I}}(t), \hat{\rho}_{\mathrm{I}}(t)] \tag{3.46}$$

analog to the Liouville von Neumann equation. Some times it is convenient to apply this equation in its equivalent integral form

$$\hat{\rho}_{\mathrm{I}}(t) = \hat{\rho}_{\mathrm{I}}(t_0) - \frac{\mathrm{i}}{\hbar} \int_{t_0}^{t} [\hat{H}_{\mathrm{I}}(s), \hat{\rho}_{\mathrm{I}}(s)] \, \mathrm{d}s. \tag{3.47}$$

Foremost at perturbative or other approximate approaches this form is convenient because it is easily iterated.

3.5. Magnetic Dipole-Dipole Interaction

The predominant interaction between separated spin systems is the magnetic dipole-dipole interaction. It depends on the magnitude and relative direction of the involved magnetic moments and the separation vector $\underline{r}$ between them. Hence we focus on solid state systems, $\underline{r}$ is taken as constant in time which is a reasonable approximation especially in diamond. Effects of motional narrowing [91] as in liquids or gases will be omitted. The dipole dipole Hamiltonian reads

$$\hat{H}_{\mathrm{dip}} = \frac{\mu_0 \, \mu_1 \, \mu_2 \, g_1 \, g_2}{2 \, \hbar \, |\underline{r}|^3} \left(3 \, \frac{(\underline{\hat{S}}^{(1)} \, \underline{r}) \, (\underline{\hat{S}}^{(2)} \, \underline{r})}{|\underline{r}|^2} - \underline{\hat{S}}^{(1)} \, \underline{\hat{S}}^{(2)} \right) \tag{3.48}$$

with μ_0 the permeability constant, μ_i the magnetic moments of the two spins and g_1 their respective g-factors. To further examine the Hamiltonian we introduce raising and lowering operators

$$\hat{S}_+ = \hat{S}_{\mathrm{x}} + \mathrm{i} \, \hat{S}_{\mathrm{y}} \tag{3.49}$$

$$\hat{S}_- = \hat{S}_{\mathrm{x}} - \mathrm{i} \, \hat{S}_{\mathrm{y}} \tag{3.50}$$

to the bases operators and rewrite [2]

$$\begin{aligned} \hat{H}_{\mathrm{dip}} =& \frac{\mu_0 \, \mu_1 \, \mu_2 \, g_1 \, g_2}{2 \, \hbar \, |\underline{r}|^3} \Bigg\{ \underline{\hat{S}}^{(1)} \, \underline{\hat{S}}^{(2)} - \\ & - 3 \left[\hat{S}_{\mathrm{z}}^{(1)} \cos\theta + \frac{1}{2} \sin\theta \left(\hat{S}_+^{(1)} \, \mathrm{e}^{-\mathrm{i}\,\phi} + \hat{S}_-^{(1)} \, \mathrm{e}^{\mathrm{i}\,\phi} \right) \right] \cdot \\ & \cdot \left[\hat{S}_{\mathrm{z}}^{(2)} \cos\theta + \frac{1}{2} \sin\theta \left(\hat{S}_+^{(2)} \, \mathrm{e}^{-\mathrm{i}\,\phi} + \hat{S}_-^{(2)} \, \mathrm{e}^{\mathrm{i}\,\phi} \right) \right] \Bigg\} \end{aligned} \tag{3.51}$$

$$= \frac{\mu_0 \, \mu_1 \, \mu_2 \, g_1 \, g_2}{2 \, \hbar \, |\underline{r}|^3} \, (A + B + C + D + E + F). \tag{3.52}$$

The coefficients A to F are

$$A = \hat{S}_z^{(1)}\,\hat{S}_z^{(2)}\,(1-3\,\cos^2\theta) \tag{3.53}$$

$$B = -\,(\hat{S}_+^{(1)}\,\hat{S}_-^{(2)} + \hat{S}_-^{(1)}\,\hat{S}_+^{(2)})\,\frac{1}{4}\,(1-3\,\cos^2\theta) \tag{3.54}$$

$$C = -\,(\hat{S}_z^{(1)}\,\hat{S}_+^{(2)} + \hat{S}_z^{(2)}\,\hat{S}_+^{(1)})\,\frac{3}{2}\,\sin\theta\,\cos\theta\,\mathrm{e}^{-\mathrm{i}\,\phi} \tag{3.55}$$

$$D = C^* = -(\hat{S}_z^{(1)}\,\hat{S}_-^{(2)} + \hat{S}_z^{(2)}\,\hat{S}_-^{(1)})\,\frac{3}{2}\,\sin\theta\,\cos\theta\,\mathrm{e}^{\mathrm{i}\,\phi} \tag{3.56}$$

$$E = -\,\hat{S}_+^{(1)}\,\hat{S}_+^{(1)}\,\frac{3}{4}\,\sin^2\theta\,\mathrm{e}^{-\mathrm{i}\,2\,\phi} \tag{3.57}$$

$$F = E^* = -\hat{S}_-^{(1)}\,\hat{S}_-^{(1)}\,\frac{3}{4}\,\sin^2\theta\,\mathrm{e}^{\mathrm{i}\,2\,\phi}. \tag{3.58}$$

These six terms affect the interacting spin systems in a qualitatively different way. To neatly distinguish the effects we look at the change of the spin states m_1 and m_2 of the unperturbed spin states

$$\begin{array}{lllll}
A & \Delta m_1 = 0 & \Delta m_2 = 0 & \Delta(m_1+m_2) = 0 \\
B & \Delta m_1 = \pm 1 & \Delta m_2 = \mp 1 & \Delta(m_1+m_2) = 0 \\
C & \Delta m_1 = \begin{cases} 0 \\ +1 \end{cases} & \Delta m_2 = \begin{cases} +1 \\ 0 \end{cases} & \Delta(m_1+m_2) = +1 \\
D & \Delta m_1 = \begin{cases} 0 \\ -1 \end{cases} & \Delta m_2 = \begin{cases} -1 \\ 0 \end{cases} & \Delta(m_1+m_2) = -1 \\
E & \Delta m_1 = +1 & \Delta m_2 = +1 & \Delta(m_1+m_2) = +2 \\
F & \Delta m_1 = -1 & \Delta m_2 = -1 & \Delta(m_1+m_2) = -2.
\end{array}$$

A has the form of two classical interacting dipoles. It describes the magnetic field of the other spin at each spin site and thus splits the energy levels of both spins without causing dynamics. B allows energy transfer between the spins. It is called the flip flop term or Förster coupling [32]. In analogy to an ac-field in the rotating frame the amplitude of the flip flop dynamics diminishes like $1/\delta^2$ with $\delta = \omega_1 - \omega_2$ the difference of the energy splittings of the interacting spins. Thus B is only relevant to similarly split spins. Because A and B commute with the unperturbed Hamiltonian they are often called the adiabatic or secular part of $\hat{H}_{\mathrm{dip}}$. They do not introduce excitation or deexcitation to the full system. Terms like C introduce mixing of the unperturbed energy eigenstates of the system. Eigenstates e.g. are of the form $|m\rangle + \alpha\,|m-1\rangle + \ldots$ with α a small value. Thus weak additional peaks at sums and differences of the unperturbed energy splittings appear in the ESR spectrum although the ac field can only excite $\Delta m = \pm 1$. Amplitudes of these lines are in the order of α^2.

The dipole coupling to uncontrolled spins in the lattice leads to inhomogeneous broadening of the transition line with of the controlled spins. The Hamiltonian of the system is

$$\hat{H} = \hat{H}_{\mathrm{S}} + \sum_i \hat{H}_{\mathrm{B}i} \hat{H}_{\mathrm{dip}i} \tag{3.59}$$

with index S indicating the system Hamiltonian and B the Hamiltonian of a bath spin. In case of different spin species (e.g. a central electron spin interacting with a bath of nuclear spins) to first order the dynamics of B due to the A is strongly suppressed because of the big energy differences. The bath spins generally are randomly distributed on the lattice. Thus their interaction strength is randomly distributed too. So the splittings from the A terms result in an approximately Gaussian shaped line [25].

If spins are localized close by, their dipole-dipole interaction is responsible for the zero field splitting of the composite system. To see that we rewrite (3.48) in the form

$$\hat{H}_{\mathrm{dip}} = \underline{\hat{S}}^{(1)} \, \underline{\underline{d}} \, \underline{\hat{S}}^{(2)} \tag{3.60}$$

with

$$d_{ij} = \frac{\mu_0 \, \mu_1 \, \mu_2 \, g_1 \, g_2}{2 \, \hbar} \left(\frac{3 \, r_i \, r_j - |\underline{r}|^2 \, \delta_{ij}}{|\underline{r}|^5} \right). \tag{3.61}$$

Now we proceed to the combined spin operator $\hat{S}$. (3.60) can now be written as

$$\hat{H}_{\mathrm{dip}} = \underline{\hat{S}} \, \underline{\underline{D}} \, \underline{\hat{S}}. \tag{3.62}$$

The zero field matrix D is now

$$d_{ij} = \frac{1}{2 \, S \, (2 \, S - 1)} \, \frac{\mu_0 \, \mu_1 \, \mu_2 \, g_1 \, g_2}{2 \, \hbar} \left(\frac{3 \, r_i \, r_j - |\underline{r}|^2 \, \delta_{ij}}{|\underline{r}|^5} \right). \tag{3.63}$$

In its diagonal form the traceless matrix $\underline{\underline{D}}$ can be rewritten as

$$\underline{\underline{D}} = -\frac{1}{3} \, (D + E) \, \hat{P}_{11} + -\frac{1}{3} \, (D - E) \, \hat{P}_{22} + \frac{2}{3} \, D \, \hat{P}_{33}. \tag{3.64}$$

In this notation $|E/D| < 1/3$. Naturally the point dipole approximation does not hold for close by spins. So r has to be integrated over the whole wave function. This makes it non trivial to determine the zero field splitting from first principles. It can be shown that for wave functions with rotational symmetry E is always equal to zero.

3.6. Treatment of Alternating Magnetic Fields

A two level system (TLS) subjected to an alternating magnetic field is a very common situation. For example all optical quantum control can be modeled this way. The system has the Hamiltonian

$$\hat{H} = \hat{H}_{\mathrm{S}} + \hat{H}_{\mathrm{ac}} \tag{3.65}$$

with the TLS's Hamiltonian

$$\hat{H}_{\mathrm{S}} = \omega_{\mathrm{L}}\, \hat{\sigma}_{\mathrm{z}}. \tag{3.66}$$

The linear polarized alternating magnetic field has the Hamiltonian

$$\hat{H}_{\mathrm{ac}} = g\, \sin(\omega\, t)\, \hat{\sigma}_{\mathrm{x}} \tag{3.67}$$

ω is the oscillation frequency of the field and g the interaction strength which is proportional to the dipole matrix element of the respective transition and the amplitude of the magnetic field. We divide the linear polarization into two circular polarized parts

$$\hat{H}_{\mathrm{ac}} = \frac{1}{2}\, g \left(\mathrm{e}^{\mathrm{i}\,\omega\, t}\, \hat{S}_k + \mathrm{e}^{-\mathrm{i}\,\omega\, t}\, \hat{S}_k \right). \tag{3.68}$$

Where the second term is representing non energy conserving so called counter propagating wave. This term leads to energy shifts like Lamb shift or Bloch-Siegert shift. They are neglected by the *rotating wave approximation* (RWA). We now transform into a rotating frame of reference to get rid of the time dependence of $\hat{H}$ by applying the time dependent transformation

$$\hat{U}(t) = \mathrm{e}^{-\mathrm{i}\,\hat{H}_{\mathrm{S}}\, t}. \tag{3.69}$$

$\hat{H}_{\mathrm{S}}$ commutes with $\hat{U}(t)$ so it remains constant in time. The Hamiltonian is now

$$\hat{H}'_{\mathrm{S}} = \hat{H}_{\mathrm{S}} + \frac{1}{2}\, g\, \hat{\sigma}_{\mathrm{x}}. \tag{3.70}$$

The second term in (3.68) would have caused an additional time dependent part

$$\hat{H}_{\mathrm{cr}} = \frac{1}{2}\, g\, \mathrm{e}^{-\mathrm{i}\,(\omega+\omega_L)\,\hat{\sigma}_{\mathrm{x}}\, t} \tag{3.71}$$

hence "counter rotating" part. Injected into the Schrödinger equation (3.32) we arrive at

$$\mathrm{i}\,\hbar\,\frac{\mathrm{d}}{\mathrm{d}t}\;|\Psi(t)\rangle' = \left(\hat{H}' + \hbar\,\omega_L \hat{P}_{11}\right)\;|\Psi(t)\rangle' \tag{3.72}$$

With $\hat{P}_{11}$ the projection operator on the $|-1/2\rangle$ state. In the rotating frame the energy eigenvalues of $\hat{H}'_{\mathrm{S}}$ become degenerate. The new effective Hamiltonian is

$$\hat{H}_{\mathrm{eff}} = \hat{H}' + \hbar\,\omega_L \hat{P}_{11}. \tag{3.73}$$

We substitute $\omega = \omega_{\mathrm{L}} + \delta$ with δ the detuning frequency. Formally the solution to the problem is

$$\hat{\rho}'(t) = \hat{\rho}_0\,\mathrm{e}^{\mathrm{i}\,\hat{H}_{\mathrm{eff}}\,t}. \tag{3.74}$$

It results in an oscillation of the magnetization

$$\mu_{\mathrm{z}} = \langle \hat{S}_{\mathrm{z}} \rangle = \mathrm{tr}\hat{\rho}(t)\,\hat{S}_{\mathrm{z}} = -1 + \frac{2\,g^2}{g^2+\delta^2}\,\sin^2\left(\frac{\omega_{\mathrm{R}}}{2}\,t\right) \tag{3.75}$$

with the Rabi frequency

$$\omega_{\mathrm{R}} = \sqrt{g^2+\delta^2}. \tag{3.76}$$

As can be seen from (3.75) the amplitude of the observed oscillation is reduced by $1/\delta$. If $\delta^2 \gg g^2$ it gets negligible small. If this is the case for all but one transition we talk of a selective pulse, because only on this single transition dynamics are introduced. This means in reverse that in order to drive selective Rabi oscillations on a system with a small difference between two transition energies the intensity of the radiation and therefore the radiation frequency has to be lowered down to meet the above requirement.

In a classical picture one would imagine a magnetic moment precessing about the external fields. The dynamics of the spin is analog to the classical dynamic if we express the quantum state as a vector in the Hilbert space pointing from the center of the sphere to the actual quantum state. The Hilbert space is depicted by a n-sphere. In the special case of a TLS a 3-sphere. The pure states form the edge of the Hilbert space. They all lie on the surface of the sphere. This representation of the Hilbert space is called the Bloch sphere (fig. 3.1). If the state vector points somewhere inside the Bloch sphere the quantum state is not a pure state. The incoherent mixtures are located on

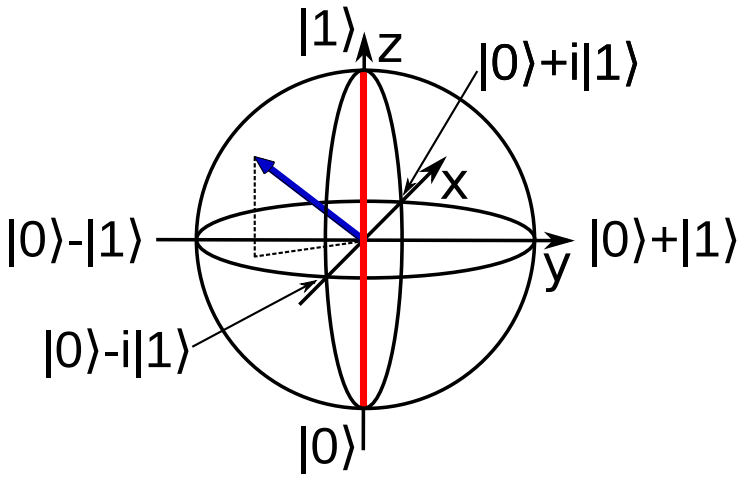

Figure 3.1.: Bloch sphere representation of the TLS Hilbert space. The blue vector is the state vector pointing to the actual quantum state within the sphere. The red line along the z-axis indicates the classical incoherent mixture of the two states $|0\rangle$ and $|1\rangle$.

the the quantization axis which is set to the z-axis. In a classical picture the dynamics is governed by the Bloch equations

$$\frac{\mathrm{d}\,\underline{M}(t)}{\mathrm{d}t} = \gamma\,(\underline{M}(t)\,\underline{B}(t))\,. \tag{3.77}$$

The analog calculation can be done in the quantum case [91]. As a result the Bloch vector precesses on the surface of the Bloch sphere. In the case of zero detuning δ it precesses in a plain perpendicular to the alternating field. The Bloch sphere is a very useful method to visualize quantum dynamics. It is also possible to introduce relaxation into the picture in a phenomenological way [91] by extending (3.77) to

$$\frac{\mathrm{d}\,M_{\mathrm{x}}(t)}{\mathrm{d}t} = \gamma\,(M_{\mathrm{x}}(t)\,B_{\mathrm{x}}(t)) + \frac{M_{\mathrm{x}}^*}{T_{2\rho}} \tag{3.78}$$

$$\frac{\mathrm{d}\,M_{\mathrm{y}}(t)}{\mathrm{d}t} = \gamma\,(M_{\mathrm{y}}(t)\,B_{\mathrm{y}}(t)) + \frac{M_{\mathrm{y}}^*}{T_{2\rho}} \tag{3.79}$$

$$\frac{\mathrm{d}\,M_{\mathrm{z}}(t)}{\mathrm{d}t} = \gamma\,(M_{\mathrm{z}}(t)\,B_{\mathrm{z}}(t)) + \frac{M_0 - M_{\mathrm{z}}}{T_1} \tag{3.80}$$

with M_0 the steady state magnetization $T_{2\rho}$ the pure transverse dephasing time and T_1 the longitudinal relaxation time. This set of equations leads to

an exponential decay of the magnetization with the two aforementioned time constants. One can also use the Bloch 3-sphere to visualize 2D subspaces of bigger Hilbert spaces. It is valid to do so as long as dynamics in the other dimensions are negligible on the examined timescale.

By the application of resonant ac fields with power ($\sim g$) low enough to affect only a single transition all operations necessary for modern quantum applications can in fact be implemented. Some are detailed below.

3.7. An Introduction to Quantum Computing and Dynamic Decoupling

It is instructive to approach pulsed measurements from an algorithmic point of view. All quantum dynamics can be expressed by the application of a unitary operator to the initial quantum state (3.33). In analogy to logical operations on classical bits they are called quantum gates. The two level quantum system (TLS) in question is referred to as qubit. Because the NV center features a $S = 1$ ground state we normally apply a magnetic field to lift the degeneracy of the $m_S = \pm 1$ levels and use $|0\rangle$ and $|-1\rangle$ as our qubit states. We label the eigenstates of the qubit as $|0\rangle$ and $|1\rangle$. Unitarity is the only constraint on logic operations performed on quantum systems. The big advantage of such a description is that it is independent of the specific physical realization of the qubit. If one is confronted with a new type of quantum system one needs only to understand the control mechanics and can directly apply any given algorithm. In the following we give an overview of quantum control operations.

A quantum system has to fulfill five criteria given by DiVincenzo [24] in order to achieve scalable quantum computing. These five criteria say that for a system to be a candidate for an implementation of quantum computation, it should

- Be a scalable physical system with well-defined qubits
- Be initializable to a pure state
- Have a universal set of quantum gates with an error per gate less than 5 %
- Have long coherence times compared to a single gate operation
- Permit high quantum efficiency, qubit-specific measurements

Postponing the scalability criterion one has to be able to initialize the qubit to a known pure state. In case of the NV center this is done by just shining green laser light on the defect center. By relaxation via the alternative decay channel the system is polarized into the $m_S = 0$ state.

3.7.1. Single Qubit gates

The single qubit gates introduced below can all be implemented by an arbitrary rotation gate. These special gates simplify algorithms by defining special often needed angles. They are realized by driving Rabi oscillations on the qubits transition that are truncated after the required rotation. Thus an arbitrary rotation gate is possible.

In case of the NV center the driving field is in the microwave range. Operations are therefore called mw-pulses. The nuclear spins that couple to the NV are addressed in the radio frequency range (rf-pulse). For simplicity all gate operations are described for TLS as qubits. It is completely analogous for the NV because the third level of the $S = 1$ system is neglected so far. Although the three level qutrid may prove relevant for more complicated algorithms in the future.

The Hadamard gate transforms the $|0\rangle$ state into the coherent superposition $(|1\rangle + |0\rangle)/\sqrt{2}$ and $|1\rangle$ into $(|1\rangle - |0\rangle)/\sqrt{2}$. It is represented by the unitary operator

$$\hat{U}_{\mathrm{H}} = \frac{1}{\sqrt{2}} \begin{pmatrix} 1 & 1 \\ 1 & -1 \end{pmatrix} \tag{3.81}$$

It corresponds to a $\pi/2$ rotation of the Bloch vector about the x-direction and is thus often simply called $\pi/2$-pulse.

The Pauli gate is the quantum pendant to a classical NOT-gate. It transforms $|0\rangle$ to $|1\rangle$ and vise versa. The unitary operator of the Pauli gate depends on the rotation direction. There are three realizations

$$\hat{U}_{\mathrm{P_x}} = \hat{U}_{\mathrm{P}} = \begin{pmatrix} 0 & 1 \\ 1 & 0 \end{pmatrix} \tag{3.82}$$

$$\hat{U}_{\mathrm{P_y}} = \begin{pmatrix} 0 & -\mathrm{i} \\ i & 0 \end{pmatrix} \tag{3.83}$$

$$\hat{U}_{\mathrm{P_z}} = \begin{pmatrix} 1 & 0 \\ 0 & -1 \end{pmatrix} \tag{3.84}$$

In some algorithms it is relevant to rotate in a specific direction. If not specified $\hat{U}_{\mathrm{P_x}}$ is used. The Pauli gate is also called π-pulse because it performs a π rotation of the Bloch vector.

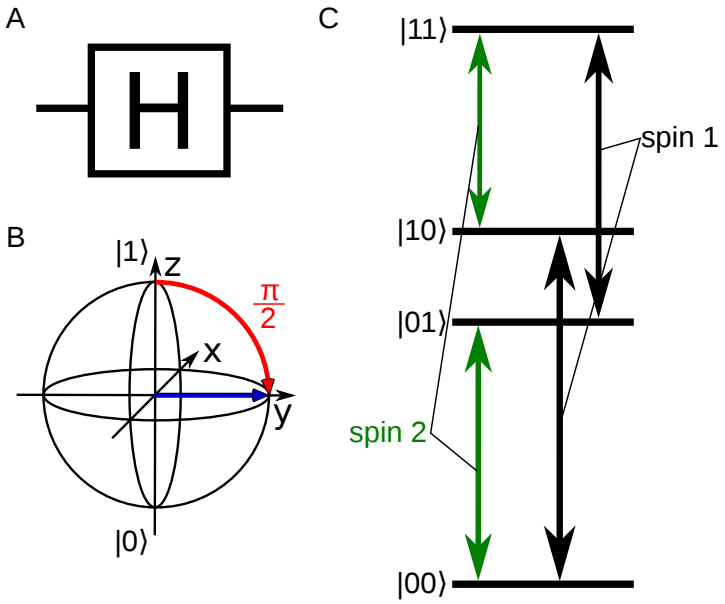

Figure 3.2.: **A** shows the quantum circuit symbol of the Hadamard gate. **B** gives the Bloch sphere representation of the gate. It is also often just called $\pi/2$-pulse. **C** depicts the transitions in a two qubit register that have to be addressed to apply the gate.

3.7.2. Two qubit gates

At multi qubit gates we restrict ourself to two qubit operations. Higher gates work in principle the same way. Nonetheless two qubit gates are sufficient for quantum computing. They are implemented by truncated Rabi oscillations on the respective transition. If the coupling between the qubits is not larger than the line width the transition can not be addressed directly or the transition can not be driven selectively. One has to resort to variants of the DEER sequence [57] as described in chapter 6 to realize the gates. If the respective transition is forbidden the gate can be implemented on a allowed transition e.g. an ancilla qubit. The outcome is then swapped onto the target pair (sec. 2.1.2).

The most important two qubit gate is the controlled-NOT-gate (CNOT), the quantum analog to a XOR-operation. It flips the controlled qubit only if the control qubit is $|1\rangle$. The unitary operator representation of the CNOT-gate

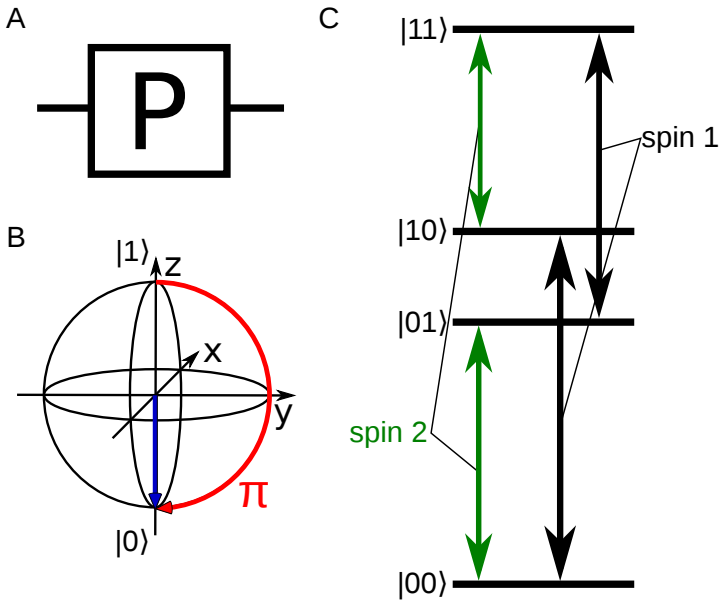

Figure 3.3.: **A** shows the quantum circuit symbol of the Pauli gate. **B** gives the Bloch sphere representation of the gate. It is also often just called π-pulse. **C** depicts the transitions in a two qubit register that have to be addressed to apply the gate. If only one transition is driven a CNOT is applied instead of a Pauli gate.

is

$$\hat{U}_{\mathrm{CNOT}} = \begin{pmatrix} 0 & 1 & 0 & 0 \\ 1 & 0 & 0 & 0 \\ 0 & 0 & 1 & 0 \\ 0 & 0 & 0 & 1 \end{pmatrix} \text{ or } \begin{pmatrix} 0 & 0 & 1 & 0 \\ 0 & 1 & 0 & 0 \\ 1 & 0 & 0 & 0 \\ 0 & 0 & 0 & 1 \end{pmatrix} \tag{3.85}$$

if the second qubit is the controlling one. The Hadamard gate and the CNOT-gate form a set of universal gates [76]. Every quantum gate can be approximated by combinations of these two. As a variant the target qubit can be flipped if the controlling qubit is $|0\rangle$. This is indicated by a small circle instead of a dot in the quantum circuit. Sometimes it is necessary to apply an arbitrary controlled rotation $\hat{O}$ on a register

$$\hat{U}_{\mathrm{Cop}} = \begin{pmatrix} \hat{O} & 0 & 0 \\ 0 & 1 & 0 \\ 0 & 0 & 1 \end{pmatrix}. \tag{3.86}$$

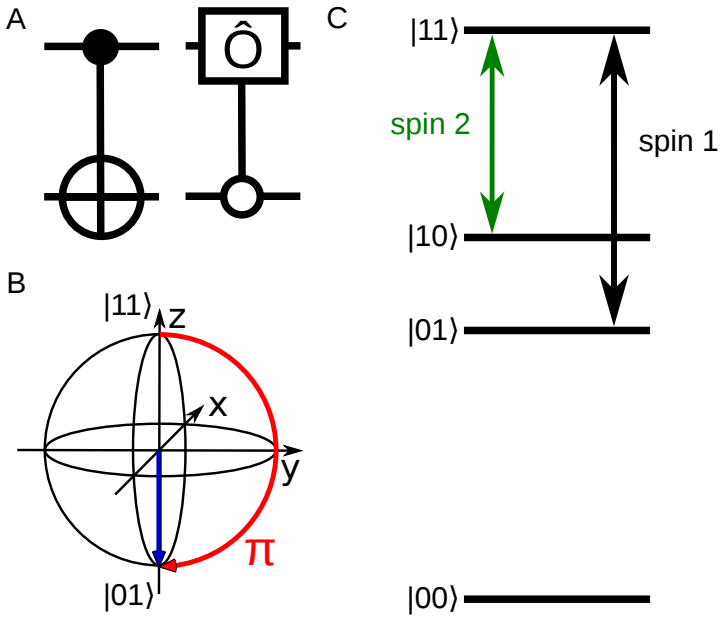

Figure 3.4.: **A** shows the quantum circuit symbol of the CNOT gate and a zero controlled arbitrary rotation $\hat{O}$. The qubit with the dot acts as the control qubit while the other (crossed circle) is flipped if the control qubit is $|1\rangle$. If the target qubit is flipped if the control qubit is $|0\rangle$ it is indicated by a small circle instead of the dot. In **B** the Bloch sphere representation of the CNOT is shown. The rotation is independent of the actual initial state. **C** indicates the transitions that have to be selectively driven to implement the CNOT gate. The single qubit transition energy has to be different to allow a direct implementation of the quantum gate.

If e.g. a controlled Hadamard gate is required it is indicated in the quantum circuit by the accounting gate symbol with the "control dots" attached. In the case of three qubits with two controlling qubits this operation is called CCNOT or Toffoli gate.

The SWAP gate interchanges the states of the two qubits

$$\hat{U}_{\mathrm{SWAP}} = \begin{pmatrix} 1 & 0 & 0 & 0 \\ 0 & 0 & 1 & 0 \\ 0 & 1 & 0 & 0 \\ 0 & 0 & 0 & 1 \end{pmatrix}. \tag{3.87}$$

It can be substituted by 3 consecutive CNOT-gates as depicted in fig. 3.5.

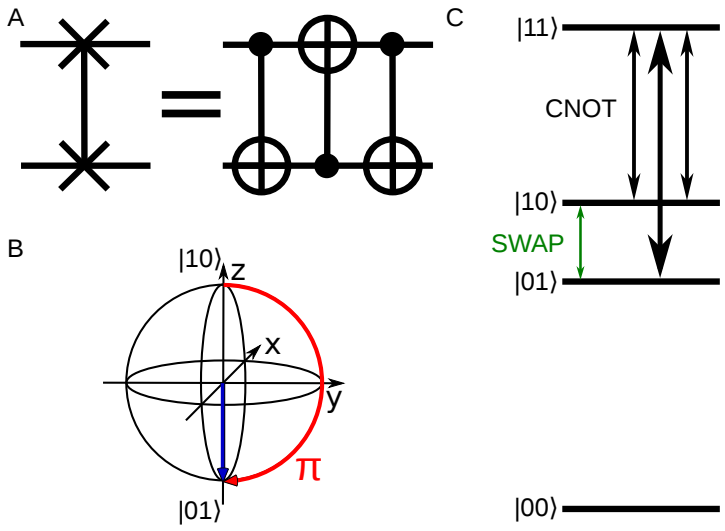

Figure 3.5.: **A** The SWAP gate can be decomposed into 3 consecutively applied CNOT gates. In combination with Hadamard gate the CNOT is universal. In **B** the Bloch sphere representation of the CNOT is shown. The rotation is independent of the actual initial state. **C** depicts the direct swap transition (green) as well as the decomposition into 3 CNOT transitions.

3.7.3. Single Qubit Algorithms

The simplest quantum algorithms are those that involve only a single qubit. They are designed to measure and/or prolong the phase coherence time or to measure the accumulation of a phase for metrology reasons. From a quantum information perspective long coherence time is indispensable because all algorithms have to be implemented within the shortest phase memory time of all qubits involved. Otherwise the quantum character of the register is lost.

Free Induction Decay

The most simple algorithm is the free induction decay (FID) experiment. There are two variants, one to measure the spin relaxation time T_1 the other to gauge the dephasing time T_2^*. The T_1 describes the system's relaxation from a pure state towards a steady state e.g. the thermal equilibrium. To probe this the system is initialized into a pure state, then evolves freely for a time τ and is measured. In the Bloch sphere picture the spin is initialized on the z direction,

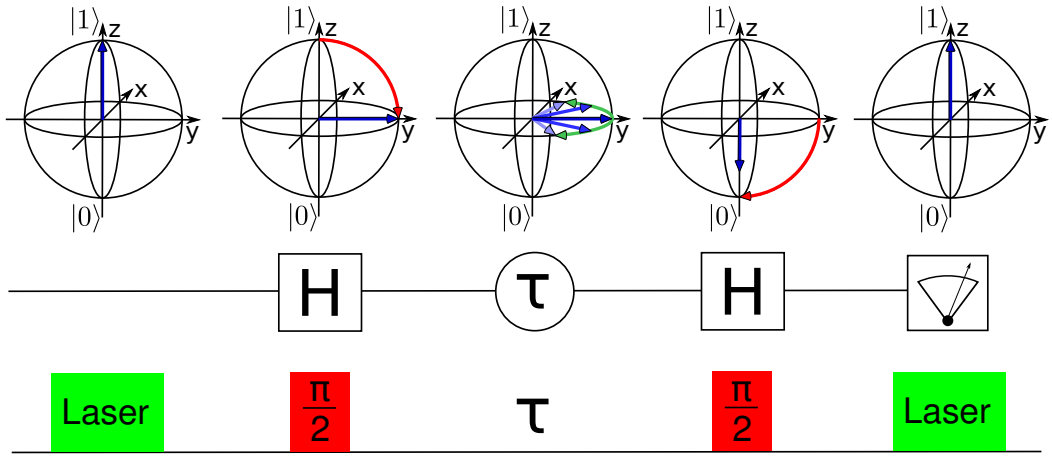

Figure 3.6.: In this figure three descriptions of the FID are displayed. In the Bloch sphere the effect of the corresponding quantum gates and free induction times is illustrated.

then shrinks along the axis until it reaches its steady state. Therefore the T_1 process is also called longitudinal relaxation.

For the second variant we start each sequence with a polarized state of the spin system. With the application of a Hadamard gate we rotate the Bloch vector into the equatorial plain of the Bloch sphere generating a superposition state. In the rotating frame in absents of external disturbance this state shows no further dynamics. If not controllable external fields now detune the transition frequency from the rotating frame the Bloch vector starts precessing about the z-axis. Due to paramagnetic defects in the vicinity the local field may be different for every repetition of the sequence in a integrated measurement and thus the precession speed of the Bloch vector. All these statistically rotated vectors for a given free precession time add up to a reduction of the length of the Bloch vector. If we repeat this experiment with different induction times τ and track the length of the Bloch vector we see it decay with increasing τ. A visualization of the sequence as a quantum circuit and in Bloch spheres is shown in fig. 3.6. Because this process shrinks the Bloch vector along the x axis towards the z axis the loss of phase coherence is called transverse relaxation in contrast to longitudinal relaxation. By solving the Bloch equations (3.78)-(3.80) we find that

$$\frac{1}{T_2^*} = \frac{1}{2\,T_1} + \frac{1}{T_{2\rho}}. \tag{3.88}$$

So in the case that $T_1 \gg T_{2\rho}$ we can approximate $T_2^* = T_{2\rho}$. On the other hand

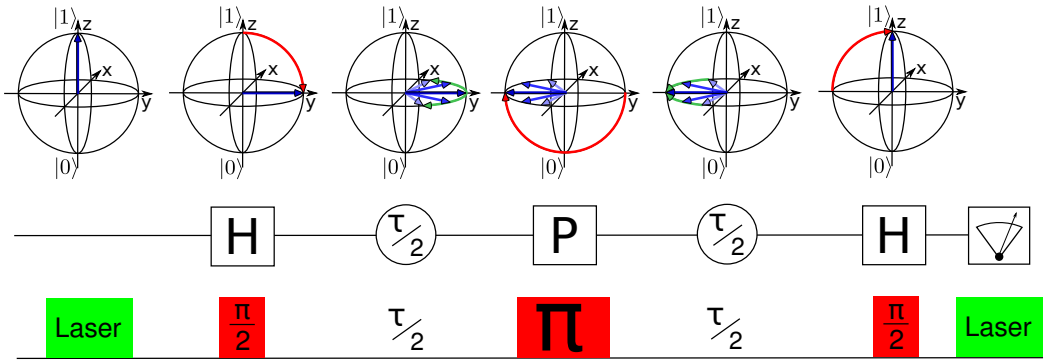

Figure 3.7.: The Hahn echo sequence is depicted by its quantum logical circuit and its pulse scheme. The Bloch spheres depict how the refocusing takes place.

T_2^* can in principle be as long as $2\,T_1$. Which is never reached in a physical system because the local fields can not be completely stabilized.

In order to improve the visibility of the decay one can detune the control field from the respective transition. Additionally to the process described above the state vector now precesses with the detuning frequency in the rotating frame. The decay manifests now in a dumped oscillation which is easier discriminated from the shot noise background. These oscillations are called Ramsey fringes [81].

Because the precession frequency is linked to the detuning δ of the transition frequency from the ac-field by

$$\omega = \mathrm{e}^{\mathrm{i}\,\delta\,t} \tag{3.89}$$

the Fourier transform of the FID signal is equal to the ESR spectrum of the probed quantum system. Normally the spectra acquired by FID have better resolution than spectra by ODMR.

Spin Echo

One method to prolong the phase coherence time is to apply a spin echo sequence or dynamic decoupling sequence. The most simple and most often applied one is the so called Hahn echo [40] depicted in fig. 3.7. It was discovered by Erwin Hahn just after finishing his graduate studies, thus kicking off the whole field of pulsed ESR and NMR experiments. Leading to an inconceivable amount of discoveries in molecular structure analysis, medical imaging, and to some extend quantum information processing. It is considered one of

the most important contributions to NMR. We start with the creation of an superposition state from a energy eigenstate by applying a Hadamard gate. Now we wait for a time $\tau/2$. A FID occurs. Now we flip the Bloch vector over by applying a π-pulse. If the fluctuating local field does not change over the course of one application of the echo sequence the Bloch vector continues to rotate in the same direction with the same angular velocity as before the π-pulse. After a second free induction time $\tau/2$ the vector arrives at a state which has π phase difference to the state created by the initial $\pi/2$-pulse. This holds true for every realization of the echo sequence. The integrated Bloch vector does not decay at all with time. The system has been decoupled from noise that fluctuates much slower than τ by the dynamic imposed on the system hence "dynamic decoupling". Field fluctuations during the application of the echo sequence are not refocused. They lead to a decay of the coherence. This coherence time is called T_2. There are more elaborated dynamic decoupling sequences like the "Carr, Purcell, Meiboom, Gill" sequence (CPMG) [19] or "Uhrig dynamic decoupling" (UDD) [100]. Their application prolongs T_2 beyond the Hahn echo result. In chapter 8.3 we examine these sequences in detail.

3.7.4. Multi Qubit algorithms - The DEER Sequence

Multi qubit quantum algorithms are described the same way by their circuit diagram. As an example we introduce the double electron electron resonance (DEER) sequence, an algorithm designed to probe the $\hat{S}_\mathrm{z} \otimes \hat{S}_\mathrm{z}$ component of an interaction Hamiltonian e.g. the A term of the dipolar coupling (sec. 3.5). The basic idea is to detect the line shift caused by the interaction by measuring the phase accumulation of a controlled spin. DEER is applied e.g. if the splitting of interest is smaller than the ESR line width. When just taking the Fourier transform of the FID does not resolve the splitting. In order to effectively narrow down the line width of the observed line (spin A) a Hahn echo sequence that refocuses all slow modulations is applied. Thus the measurements precision is limited by T_2 rather than T_2^* of the FID. To render the probe spin sensitive to the interaction to the second spin that spin is flipped during the second free precession time of the echo. If the spin is flipped at the end of the Hahn echo sequence it is completely refocused assuming $T_1^{(\mathrm{B})} \gg \tau$. If spin B is flipped at a time $\tau/2+T$ with $T < \tau/2$ a net phase is accumulated. During the Hahn echo spin A accumulates the phase $\phi_1 = \gamma\, B_\mathrm{int}\, \tau/2$ until the Pauli gate by the magnetic field of spin B B_int. The Pauli gate inverts the phase and it starts to refocus $\phi_2 = -\phi_1 + \gamma\, B_\mathrm{int}\, T$. After spin B is flipped the

phase accumulation inverts its direction again

$$\phi_\mathrm{f} = \phi_2 - \gamma\, B_\mathrm{int}\,(\tau/2 - T) = \gamma\, B_\mathrm{int}\,(\tau - 2\,T). \tag{3.90}$$

So if τ is kept constant and T is varied the signal oscillates with twice the interaction frequency. Of course this only works if spin B was polarized in the beginning. For a mixed state of B spin A only feels the net magnetic field.

In addition to the detection of the coupling the observed oscillation can be utilized to substitute a selective pulse on the flip flop transition. T is then chosen such that the desired phase is accumulated (sec. 6). The phase rotation is translated into a population difference by the final Hadamard gate. This gates precision again is limited by T_2 of qubit A and thus applicable even if the splitting due to the coupling is not resolved in the ESR spectrum.

For $S = 1$ systems there are several possibilities to perform the DEER sequence. If the Hahn echo gates are applied on the $|0\rangle \leftrightarrow |\pm1\rangle$ transition and spin B is flipped from $|0\rangle$ to $|\pm1\rangle$ there is no phase accumulation until spin B is flipped ($\phi_1 = \phi_2 = 0$). Thus the signal oscillates with the interaction frequency

$$\phi_\mathrm{f} = \phi_2 - \gamma\, B_\mathrm{int}\,(\tau/2 - T) = -\gamma\, B_\mathrm{int}\,(\tau/2 - T). \tag{3.91}$$

It is also possible to initialize spin B into $|\pm1\rangle$ and flip it to $|\mp1\rangle$. Then again the double frequency is observed. To apply the Hahn echo on the double transition $|\pm1\rangle \leftrightarrow |\mp1\rangle$ of spin A doubles the phase acquisition. The signal therefore oscillates with

$$\phi_\mathrm{f} = \begin{cases} \gamma\, B_\mathrm{int}\,(\tau - 2\,T) & \text{for spin B } |0\rangle \rightarrow |\pm1\rangle \\ \gamma\, B_\mathrm{int}\,(\tau - 4\,T) & \text{for spin B } |\pm1\rangle \rightarrow |\mp1\rangle\,. \end{cases} \tag{3.92}$$

The quantum circuits of all DEER variants are depicted in fig. 3.8.

3.8. Evaluation of Quantum States - Fidelity and Entanglement Measures

The implementation of quantum gates on a real physical system is never as perfect as assumed up until now. The gate durations are estimated by an initial Rabi oscillation which is prone to environmental noise and shot noise from the laser there are already small errors at the fit of the oscillation and thus to the pulse durations. In addition the acquisition of the data needs either a time average or an ensemble average. Small changes to the transition frequencies

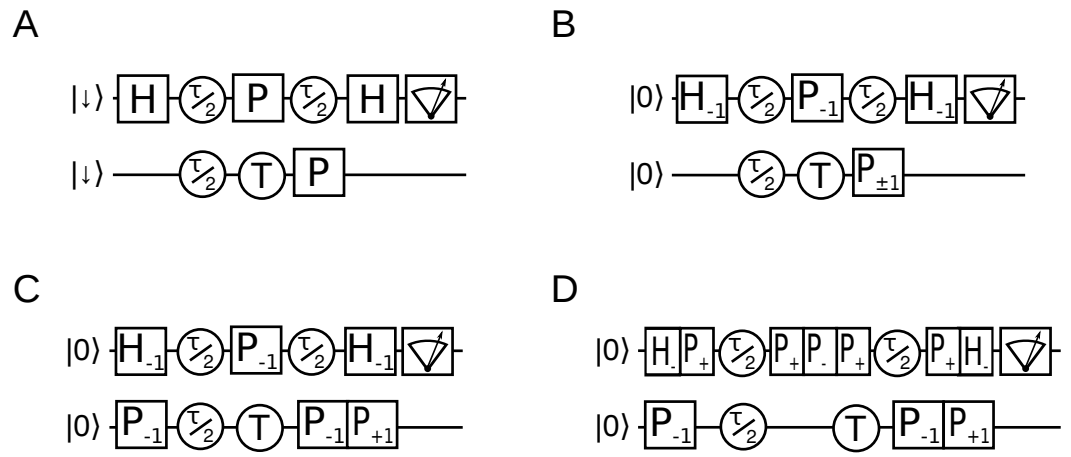

Figure 3.8.: **A** The quantum circuit of two $S = 1/2$ spins. The resulting signal oscillates with twice the coupling frequency. **B**-**D** show possible DEER algorithms for two $S = 1$ spins. The transitions the gates have to be applied to are marked by the indices $-$ for $|0\rangle \leftrightarrow |-1\rangle$, $+$ for $|0\rangle \leftrightarrow |+1\rangle$ and $\pm$ for $|-1\rangle \leftrightarrow |+1\rangle$. The signal corresponds to the coupling frequency once (**C**), twice (**B**) and four times (**D**) the coupling.

e.g. due to temperature changes or field inhomogeneities lead to pulse errors over the course of the measurement. Furthermore the gates can not be applied instantaneously but have some duration which normally is short compared to the experiment duration τ but nonetheless allows system dynamics on other transitions during the pulse. As the transition frequencies get dense either to similar interaction frequencies or the increasing number of qubits the control pulses are not perfectly spin selective any more. So transitions that are not part of the desired gate are weakly driven as well, causing additional errors to the gate result. There are three major questions to ask to address this situation. How can the performance of a gate operation be quantized? How much error per gate can a quantum algorithm take? How can errors be corrected? The first two questions are addressed here. Quantum error correction is a field of its own and not discussed in this work. Although dynamical decoupling (sec. 3.7) can be viewed as single qubit error correction. The simplest possibility to evaluate the performance of a gate is to define a distance measure on the Hilbert space and measure how close a generated state gets to the ideal target state. Such a measure is the fidelity F of a quantum state. It is taken from classical probability theory. Where the fidelity of two random variables $\underline{p}$ and

$\underline{q}$ it is defined as

$$F(p,q) = \sum_i \sqrt{p_i\, q_i}. \tag{3.93}$$

It is easy to see that

$$0 \leq F(p,q) \leq 1 \tag{3.94}$$

and $F = 1$ if and only if $\underline{p} = \underline{q}$. It is the overlap of the two random variables. The same notion transfered to pure quantum states $|\Phi\rangle$ and $|\Psi\rangle$ leads to the definition

$$F(|\Phi\rangle, |\Psi\rangle) = |\langle\Phi|\Psi\rangle|^2 \tag{3.95}$$

If one state is represented by a density operator $\hat{\rho}$ this is generalized to

$$F(|\Phi\rangle, \hat{\rho}) = \langle\Phi|\,\hat{\rho}\,|\Phi\rangle = \mathrm{tr}\hat{\varphi}\,\hat{\rho} \tag{3.96}$$

with $\hat{\varphi} = |\Phi\rangle\langle\Phi|$. This definition is used most frequently to determine how close an experimentally generated quantum state is to the ideal result of the algorithm. From the product $\hat{\varphi}\,\hat{\rho}$ in (3.96) one can directly see, that only entries that are nonzero in both density operators contribute to the fidelity. Therefore only nonzero components of the density operator of the generated state need to be measured to calculate the fidelity of an algorithm or gate. To scale up a quantum register an error per gate $(1 - F(|\Phi\rangle, \hat{\rho}))$ of 0.05 or less is required [58]. The definition (3.96) fails however if none of the two states is a pure state. As introduced by Jozsa [55] the correct extension is

$$F(\hat{\sigma}, \hat{\rho}) = \left(\mathrm{tr}\sqrt{\sqrt{\hat{\rho}}\,\hat{\sigma}\,\sqrt{\hat{\rho}}}\right)^2 \tag{3.97}$$

The fidelity is basis invariant

$$F(\hat{\sigma}, \hat{\rho}) = F(\hat{U}\,\hat{\sigma}\,\hat{U}^*, \hat{U}\,\hat{\rho}\,\hat{U}^*) \tag{3.98}$$

as well as symmetric in its arguments

$$F(\hat{\sigma}, \hat{\rho}) = F(\hat{\rho}, \hat{\sigma}). \tag{3.99}$$

In the special case of entangled states the fidelity can only tell that there is no entanglement if $F \leq 0.5$. In order to decide whether or not the generated state is entangled or not an entanglement witness has to be utilized. For

bipartite systems the Peres-Horodecki criterion or positive partial transpose (PPT) is such a witness [77]. It gives a necessary criterion for the separability of a state $\hat{\rho}$. As proven by Horodecki [44] for systems of the form $2 \otimes 2$ and $3 \otimes 2$ it is even sufficient. With

$$\hat{\rho} = \hat{\rho}^{\mathrm{A}} \otimes \hat{\rho}^{\mathrm{B}} = \rho^{\mathrm{A}}_{ij}\, \rho^{\mathrm{B}}_{\alpha\beta} = \rho_{i\alpha\, j\beta} \tag{3.100}$$

we introduce four indices to the density operator. By interchanging one set (Latin or Greek letter indices) the matrix is partially transposed (pT)

$$\mathrm{pT}(\rho_{i\alpha\, j\beta}) = \xi_{j\alpha\, i\beta}. \tag{3.101}$$

This is no unitary transformation but leaves $\hat{\xi}$ a Hermitian operator nonetheless. If $\hat{\rho}$ is separable, that means it can be written as a sum of direct products

$$\hat{\rho} = \sum_k w_k\, \hat{\rho}^{\mathrm{A}}_k \otimes \hat{\rho}^{\mathrm{B}}_k, \tag{3.102}$$

the partial transpose is

$$\xi_{j\alpha\, i\beta} = \mathrm{pT}(\rho_{i\alpha\, j\beta}) = \sum_k w_k\, (\hat{\rho}^{\mathrm{A}}_k)^T \otimes \hat{\rho}^{\mathrm{B}}_k. \tag{3.103}$$

$\hat{\xi}$ is again a valid density matrix. Therefore none of its eigenvalues can be negative. If the partial transpose leads to one or more negative eigenvalues the state can not be separable and must therefore be entangled. The inverse statement, that if all eigenvalues are positive the state is separable, is only true for $2 \otimes 2$ and $3 \otimes 2$ systems. The drawback of the partial transpose is that it makes only a Boolean statement whether a given state is separable or not. It does not quantify the amount of entanglement. To do so one needs to find a figure of merit that is monotonous in the amount of entanglement in the system. For pure states of bipartite the von Neumann entropy

$$S(\Psi) = -\mathrm{tr}\{\hat{\rho}^A\, \ln \hat{\rho}^A\} = -\mathrm{tr}\{\hat{\rho}^B\, \ln \hat{\rho}^B\} \tag{3.104}$$

is such a measure. Since the local state obtained by the partial trace operation

$$\hat{\rho}^{A(B)} = \mathrm{tr}_B(A)\, |\Psi\rangle\, \langle Psi| \tag{3.105}$$

is pure ($S(\Psi) = 0$) if the system was not entangled and a maximally mixed state ($S(\Psi) = \log_2 N$) if maximally entangled, with N the Hilbert space dimension. Due to classical correlations mixed states can however have nonzero local entropy even if the global state is not entangled. This makes the von

Neumann entropy a very fragile entanglement measure. In order to maintain the entropy idea the entanglement of formation measure was defined as the minimum of an average entropy of the state over all pure state decompositions of the state [11]

$$E_{\mathrm{f}}(\hat{\rho}) = \min \sum_i p_i S(\Psi_i). \tag{3.106}$$

This poses a reliable measure of bipartite entanglement. The major drawback is that there is no explicit formula for the entanglement of formation except for $2 \otimes 2$ systems [105]. Here Wootters has shown that the entanglement of formation of a two qubit state is related to a quantity called concurrence as

$$E_{\mathrm{f}}(\hat{\rho}) = H(\frac{1}{2} + \frac{1}{2}\sqrt{1 - C^2}) \tag{3.107}$$

With $H(x) = -1 \ln x - (1-x) \ln (1-x)$ the binary entropy and the concurrence

$$C(\hat{\rho}) = \max\{0, \lambda_1 - \lambda_2 - \lambda_3 - \lambda_4\}, \tag{3.108}$$

where λ_i are the non negative eigenvalues, in decreasing order, of the Hermitian Matrix

$$\hat{R} = \sqrt{\sqrt{\hat{\rho}}\,\tilde{\hat{\rho}}\,\sqrt{\hat{\rho}}}. \tag{3.109}$$

Hereby $\tilde{\hat{\rho}}$ the spin flipped state of $\hat{\rho}$ is defined as

$$\tilde{\hat{\rho}} = (\hat{\sigma}_{\mathrm{y}} \otimes \hat{\sigma}_{\mathrm{y}})\, \hat{\rho}^*\, (\hat{\sigma}_{\mathrm{y}} \otimes \hat{\sigma}_{\mathrm{y}}), \tag{3.110}$$

with $\hat{\rho}^*$ the complex conjugate of $\hat{\rho}$. Because the entanglement of formation is a monotonic function of the concurrence the latter can directly used as an measure of bipartite entanglement.

Multipartite entanglement is way richer than bipartite entanglement because there is not only the distinction between separable and entangled but also partial separability is possible. As a straight forward generalization of the two particle case a m-particle state is fully separable if it can be written as

$$\hat{\rho} = \sum_i p_i \hat{\rho}_i^1 \otimes \cdots \otimes \hat{\rho}_i^m. \tag{3.111}$$

The other way round it is fully entangled if it can not be written that way. A state is separable with respect to a given partition $\{I_1, \ldots, I_k\}$, where the I_i

are disjoint subsets of the indices $\{1, \ldots, m\}$, if and only if it can be written as

$$\hat{\rho} = \sum_i p_i \hat{\rho}_i^{\mathrm{p}1} \otimes \cdots \otimes \hat{\rho}_i^{\mathrm{p}k}. \tag{3.112}$$

A state is called semiseparable if it is separable with respect to all partitions. There is also more than one notion of a maximally entangled state. There could be m-fold entanglement or any combination of partitioned entanglement pairwise, triplewise, ... over all partitions. There are several measures for multipartite entanglement. A. Miyake showed that hyperdeterminants are monotonous functions of entanglement [66]. The bipartite concurrence hereby is the first order whereas the 3-tangle of tripartite systems

$$\tau(I_1 : I_2 : I_3) = C(I_1 : I_2\, I_3)^2 - C(I_1\, I_2)^2 - C(I_1\, I_3)^2 \tag{3.113}$$

is the second order hyperdeterminant. The 3-tangle is permutationally invariant and vanishes on all states that are separable under any cut. Even for states that feature bipartite entanglement such that it is not separable with respect to any cut $\tau(I_1 : I_2 : I_3) = 0$ still holds.

These measures are sufficient to characterize all quantum states examined in this work. For further information on the rich physics of quantum entanglement see [45].

Part II.

Main

4. Rabi Oscillations at Low Magnetic Field

In $S = 1$ Systems like the NV^- there are two allowed transitions $|0\rangle \leftrightarrow |\pm 1\rangle$. The $m_S = \pm 1$ levels are separated from $m_S = 0$ by the zero field splitting due to internal interaction (sec. 3.5). If the $m_S = \pm 1$ levels are well separated e.g. by a magnetic field and the ac-field frequency is close to resonance with one transition we are in the limit of $\delta^2 \gg g^2$ (sec. 3.6) for the other transition. In this case there is no effective difference to the TLS case described in section 3.6, resulting in Rabi oscillations

$$\mu_z = -1 + \frac{2\,g^2}{g^2 + \delta^2}\,\sin^2\left(\frac{\sqrt{g^2 + \delta^2}}{2}\,t\right) \tag{4.1}$$

If however at low magnetic fields the $m_S = \pm 1$ levels are only slightly split or even degenerate both transitions are driven simultaneously. This makes a more involved description necessary [30].

Starting from the system Hamiltonian

$$\hat{H}_S = D\,(\hat{S}_z^2 - 2/3\,\mathbb{1}) + \gamma\,\underline{B}\,\underline{\hat{S}} \tag{4.2}$$

we apply a driving field in the semi classical description

$$\hat{H}_{ac} = g\,\sin(\omega\,t)\,\hat{S}_x \tag{4.3}$$

to the system. Here we assume that the transitions $|0\rangle \leftrightarrow |\pm 1\rangle$ have equal transition matrix elements which is reasonable for most experimental situations. After the RWA and transformation into the rotating frame the Hamiltonian has the form

$$\hat{H}_{rot} = \begin{pmatrix} \Delta - \delta & g & 0 \\ g & 0 & g \\ 0 & g & \Delta + \delta \end{pmatrix} \tag{4.4}$$

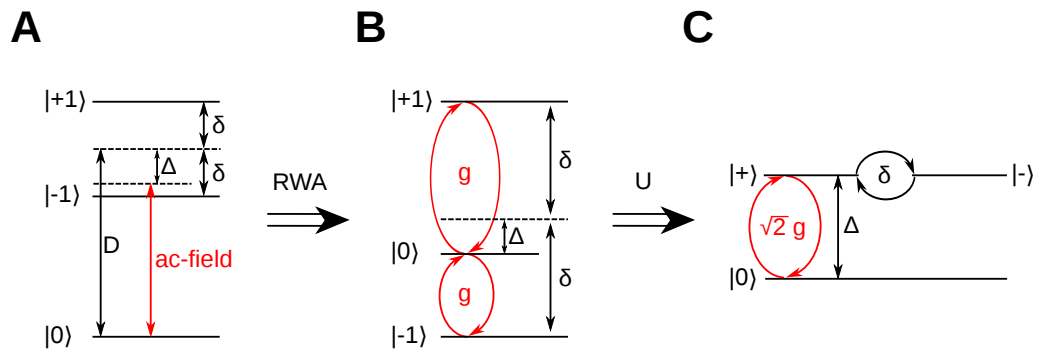

Figure 4.1.: **A** the NVs ground state level scheme. Δ and δ denote the detuning of the driving field from the two transitions and D is the zero field splitting. **B** Level scheme after the rotating wave approximation. The driving field is transformed in an time independent coupling g. **C** Final basis transform to the $|\pm\rangle$ basis states.

with $\delta = \Delta E_{\pm 1}/2$ and Δ the detuning of the microwave from $|-1\rangle + \delta$ (fig. 4.2). To obtain the new Rabi frequency we transform $\hat{H}_{\text{rot}}$ into a new basis

$$|+\rangle = |-1\rangle + |+1\rangle \tag{4.5}$$
$$|-\rangle = |-1\rangle - |+1\rangle \tag{4.6}$$
$$|0\rangle = |0\rangle\,. \tag{4.7}$$

By the transformation

$$\hat{U} = \begin{pmatrix} \frac{1}{\sqrt{2}} & 0 & -\frac{1}{\sqrt{2}} \\ 0 & 1 & 0 \\ \frac{1}{\sqrt{2}} & 0 & \frac{1}{\sqrt{2}} \end{pmatrix}. \tag{4.8}$$

There the Hamiltonian reads

$$\hat{H}'_{\text{rot}} = \begin{pmatrix} \Delta & 0 & -\delta \\ 0 & 0 & \sqrt{2}\,g \\ -\delta & \sqrt{2}\,g & \Delta \end{pmatrix}. \tag{4.9}$$

Only one effective transition is driven in this basis. In order to obtain compact analytical eigenvalues we set $\Delta = 0$. This leads to a Rabi frequency of

$$\omega'_{\text{R}} = \sqrt{2\,g^2 + \delta^2}. \tag{4.10}$$

If the $|\pm 1\rangle$ states are degenerate or $g \gg \delta$ the Rabi frequency observed by driving two transitions at once is $\sqrt{2}$ faster than driving a single level. We

now consider the time evolution of the system with initial state $|0\rangle$. The dynamics of $|0\rangle$ are

$$\rho_{|0\rangle} = \frac{\left(\delta^2 + 2\,g^2\,\cos\left[\sqrt{2\,g^2+\delta^2}\,t\right]\right)^2}{(2\,g^2+\delta^2)^2}. \tag{4.11}$$

From expanding the numerator we see, that there are actually two frequencies involved, corresponding to the cos and $\cos^2$ terms. If $|\pm 1\rangle$ are again degenerate or $g \gg \delta$ the dominant frequency corresponds to $\cos^2$. Thus the observed Rabi frequency of such a triplet system is

$$\omega'_{\mathrm{R\,eff}} = 2\,\sqrt{2\,g^2+\delta^2}. \tag{4.12}$$

Experimental verification of these frequencies is shown in fig. 4.2. In the data hyperfine splitting due to the ^{14}N nuclear spin is present. Because the the nuclear spin is in its totally mixed state the three resulting Rabi oscillation are independent of one another. They are all carried out simultaneously, resulting in a beating of the oscillation amplitude.

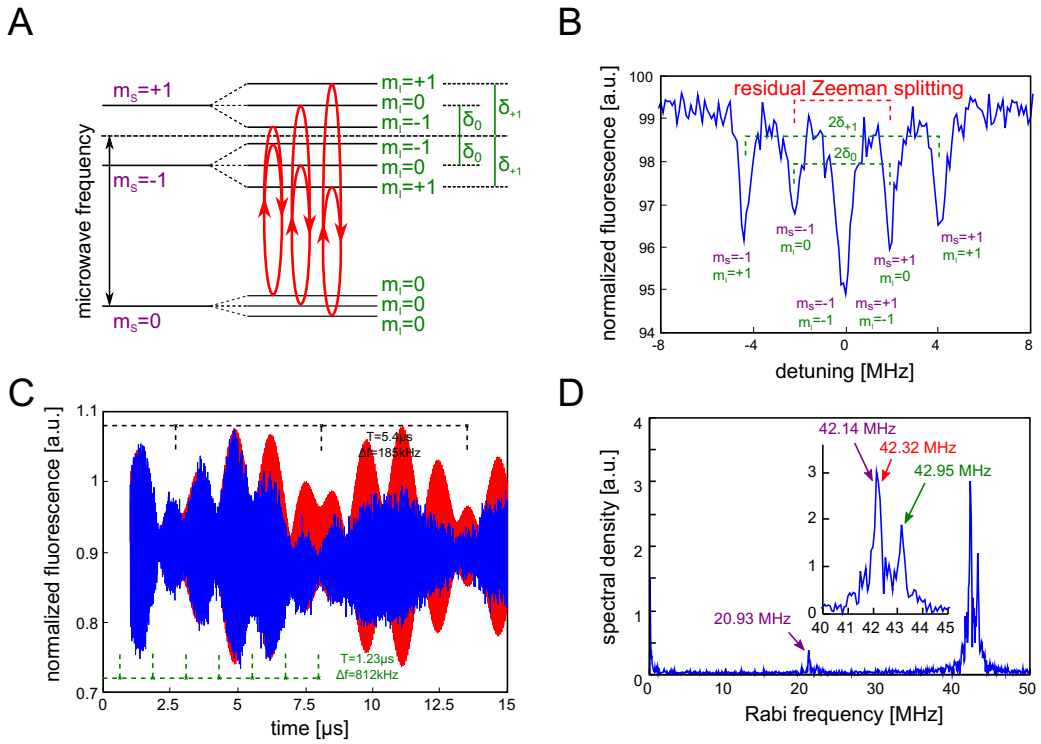

Figure 4.2.: **A** Level scheme of the recorded Rabi oscillations. For the sake of simplicity the contribution of the $m_S = 0$ hyperfine splitting was neglected. The three separate three level Rabi oscillations cause the beating observed in **C**. **B** ODMR spectrum of the second NV center without DC bias field. The two hyperfine triplets corresponding to the $m_s = -1$ and $m_s = +1$ spin levels overlap in the central dip. **C** Rabi oscillations of the system shown in **B**. The solid blue line depicts the experimental data. The solid magenta line represents the calculated beatings. Black and green markers denote the extracted beat frequencies. **D** Fourier transform of the oscillations in ^{13}C.

5. Coherence of the NV Center in ^{13}C Environments with Varying Density

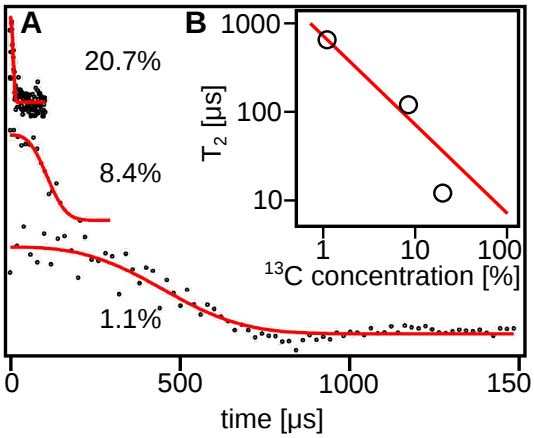

Figure 5.1: **A** Hahn echo decays at varying ^{13}C concentrations (1.1 %, 8.4 %, 20.7 %). The black dots mark the measurement data, the red lines are fitted according to [21] with $\exp\{(t/T_2)^3\}$. **B** ^{13}C concentration (f) dependence of T_2. The red line is the best fit $1/f$ curve.

For all applications like quantum computing, communication and metrology [50, 29, 74, 53, 64, 4, 63] it is of uttermost importance that the quantum register remains in a coherent state for as long as possible. In a quantum computer the coherence time of the qubits should be much bigger than the gate time. The number of gates possible limits the complexity of a quantum algorithm. In quantum communication the coherence time of the qubits involved limits the communication distance. And in metrology the achievable sensitivity is determined by the lifetime of the sensor qubit. To prolong the coherence time one has to understand the mechanisms of decoherence. In most solid state systems the spin lattice relaxation is dominant. Experiments can only be conducted at low temperatures. In diamond even at room temperature few phonon modes are excited thus enabling room temperature quantum experiments. In quantum dot systems nuclear spins of the semiconductor material cause fast decay. Diamond lattice in contrast is essentially spin free because the most abundant carbon isotope (^{12}C) carries no nuclear spin. At natural abundance there is

1.1 % of ^{13}C in the lattice carrying a $I = 1/2$ nuclear spin. To confirm that the carbon nuclear spins are the main source of dephasing measurements of T_2 as well as T_2^* have been performed on various NV centers in diamond samples with ^{13}C concentration (f) varying from $0,03$ % to ~ 100 %. Here the 0.03 % and the 100 % diamonds are grown with HPHT method utilizing getters that prevented the incorporation of Nitrogen into the lattice. The samples with 0.35 %, 1.1 %, 8.4 % and 20.7 % ^{13}C are CVD grown. The Nitrogen concentration was below the ESR detection limit (1 pbb) in those crystals. In the HPHT diamonds it was around 1 ppm.

The T_2 time was found to be inversely proportional with the carbon concentration as depicted in fig. 5.1. This is in accordance with results found by disjoint cluster expansion [64]. The HPHT diamonds are excluded from this analysis because the generation of paramagnetic impurities could not be suppressed during the growth process. T_2^* i.e. on the other hand shows $T_2^* \sim f^{-\frac{1}{2}}$ dependence with the carbon concentration f. As depicted in fig. 5.2 there are two regimes. In the high concentration regime above 1.1 % ^{13}C the line width $\Delta\omega = 2\sqrt{\ln 2}/\pi\, T_2^*$ is dominated by exchange interaction between the NV electron spin and the closest ^{13}C nuclear spins. This is similar to P donors in ^{29}Si. Here the average line width is well described by [1, 59]

$$\overline{\Delta\omega} = 2\sqrt{2\,\ln 2}\left[f\sum_l \left(\frac{a_l}{2}\right)^2\right]^{\frac{1}{2}} \tag{5.1}$$

with a_l the exchange interaction. The sum runs over all lattice sites. The first three shells around the vacancy account for over 90 % of the linewidth. In the low concentration regime the inhomogeneous broadening is governed by dipole-dipole interaction. To calculate the ODMR line width of the NV center we apply the method of moments.

5.0.1. Method of Moments

In principle it is possible to calculate the inhomogeneous broadening of a transition by applying Gibbs model of ac-field absorption [2]. It considers the Hamiltonian of the central system $\hat{H}_{\mathrm{S}}$ and its spin environment

$$\hat{H} = \hat{H}_{\mathrm{S}} + \sum_i \hat{H}_{\mathrm{B}i} + \hat{H}_{\mathrm{I_{SB}}i} + \sum_{j>i} \hat{H}_{\mathrm{I_{BB}}ij} \tag{5.2}$$

with $\hat{H}_{\mathrm{B}i}$ the Hamiltonian of a bath spin, $\hat{H}_{\mathrm{I_{SB}}i}$ the system - environment interaction and $\hat{H}_{\mathrm{I_{BB}}ij}$ the inter bath interactions. If an ac magnetic field

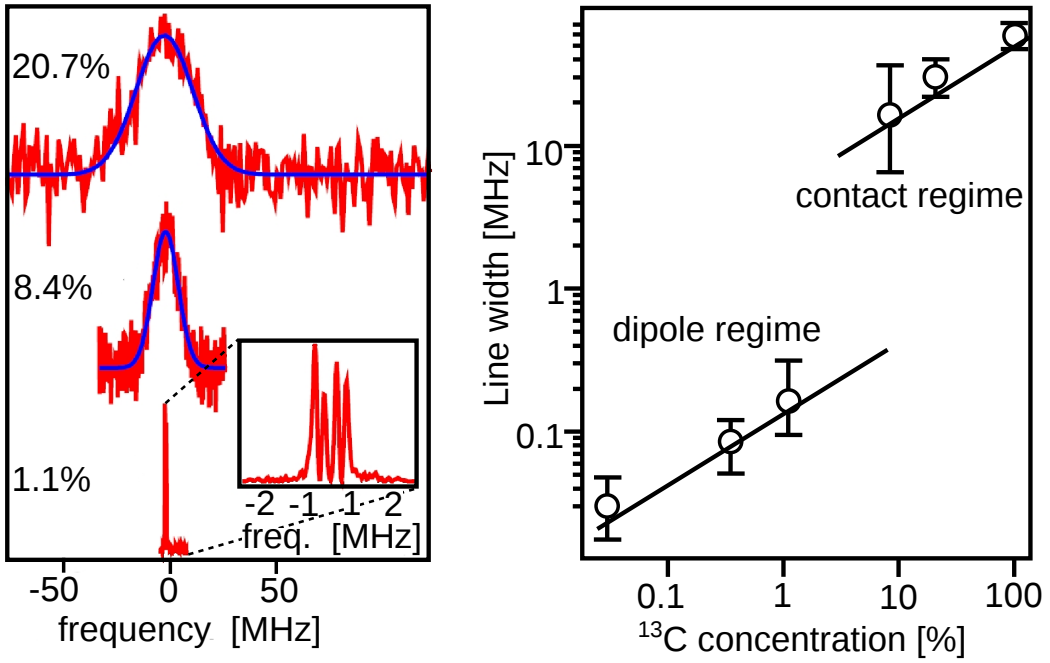

Figure 5.2.: **A** Examples of ODMR lines at different ^{13}C concentrations (1.1 %, 8.4 %, 20.7 %). Red lines show experimental data, blue lines are fitted Gaussian lines. **B** Concentration dependence of the line width. In the low concentration regime it is dominated by dipole coupled ^{13}C spins. The solid line here calculated from the 2$^{\text{nd}}$ moment (5.36). At high concentrations the exchange interaction dominates. The solid line is calculated by (5.1).

$g \cos(\omega t)\, \hat{S}_\mathrm{x}$ is applied one arrives at the dynamics of the magnetization along the x-axis

$$M_\mathrm{x} = g\,(\chi'(\omega)\cos(\omega t) + \chi''(\omega)\sin(\omega t)). \tag{5.3}$$

After transforming to the Heisenberg picture and some algebra we arrive at

$$\chi''(\omega) = C \int_0^\infty \cos(\omega t')\, G(t')\, \mathrm{d}t', \tag{5.4}$$

where $G(t')$ is the time correlation function of the magnetization operator in the Heisenberg picture

$$G(t) = \mathrm{tr}(\hat{M}_\mathrm{x}(t)\, \hat{M}_\mathrm{x}). \tag{5.5}$$

Because the size of the Hilbert space scales with 2^N, with N the number of spins, no exact solution to this problem is feasible. Still we are able to calculate the moments $\mathcal{M}_n$ of the transition line [101]. They are a set of numbers that are used to characterize the shape of a distribution. If the distribution is symmetric to its peak all odd moments vanish. The second moment $\mathcal{M}_2$ is a measure of the width of the distribution. It is called the variance. The fourth moment $\mathcal{M}_4$ the kurtosis is a measure of the wings of the distribution. It describes whether they are sharp or flat. The n^{th} moment of a real valued function $f(x)$ is defined as

$$\mathcal{M}_n = \int_{-\infty}^{\infty} (x - x_0)^n \, f(x) \, \mathrm{d}x. \tag{5.6}$$

The main problem with the calculation of the moments of the inhomogeneous broadened ODMR line is that we have to exclude interactions that lead to a splitting rather than a broadening. Easy to see that if a spin of the bath is interacting stronger with the central spin than the line width introduced by the other environmental spins it has to be discarded. This is especially true for ^{13}C spins within the first and third shell of lattice sites around the vacancy site. They interact with 130 MHz and 14 MHz respectively [67]. For simplicity we neglect the first 3 shells. A second possibility for additional lines is the contribution of the non secular part of the dipole-dipole Hamiltonian. It allows transition frequencies of $2\,\omega_0$, $3\,\omega_0$ etc. if ω_0 is the transition frequency. These lines have very small amplitudes, but due to their high frequency difference they would change the moments of the distribution drastically. In order to get the correct line width we have to restrict ourself to the secular part of the dipole-dipole interaction

$$H_{\mathrm{I}i} = \gamma_{\mathrm{e}} \, \gamma_{\mathrm{n}} \hbar^2 \, \frac{1 - 3 \, \cos^2 \theta}{r^3} \, \hat{S}_{\mathrm{z}} \otimes \hat{I}_{\mathrm{z}i}. \tag{5.7}$$

It is again easy to see that the line is symmetric to its central frequency. Every shift δ of the resonance frequency ω_0 by the above interaction will be exactly inverted by flipping all the spins responsible for the shift

$$\omega_0 + \delta \overset{\text{spin flip}}{\Rightarrow} \omega_0 - \delta. \tag{5.8}$$

At high temperatures both orientations are equally probable. Thus the line is symmetric. All odd moments therefore vanish. Since moments of a curve are proportional to the derivatives at the origin of its Fourier transform we

start from (5.4) with their derivation [2]. We introduce the normalized shape function $f(\omega)$ and rewrite (5.4)

$$f(\omega) = A \int_0^\infty \cos(\omega\, t)\, G(t)\, \mathrm{d}t. \tag{5.9}$$

A is determined by the normalization of $f(x)$ and $G(t)$. And therefore

$$G(t) = \frac{2}{\pi\, A} \int_0^\infty \cos(\omega\, t)\, f(\omega)\, \mathrm{d}\omega. \tag{5.10}$$

Since in the Heisenberg picture $\hat{H}_{\mathrm{HS}}$ commutes with $H_{\mathrm{HI}i}$ we may write

$$G(t) = \mathrm{tr}\left(\mathrm{e}^{\mathrm{i}\,\mathrm{H_S}\,t}\, \mathrm{e}^{\mathrm{i}\,\hat{H}_\mathrm{I}\,t}\, \hat{M}_\mathrm{x}\, \mathrm{e}^{-\mathrm{i}\,\hat{H}_\mathrm{I}\,t}\, \mathrm{e}^{-\mathrm{i}\,\hat{H}_\mathrm{S}\,t}\, \hat{M}_\mathrm{x}\right) \tag{5.11}$$

With the trace operation invariant to cyclic permutation of its components we can write

$$G(t) = \mathrm{tr}\left(\mathrm{e}^{\mathrm{i}\,\hat{H}_\mathrm{I}\,t}\, \hat{M}_\mathrm{x}\, \mathrm{e}^{-\mathrm{i}\,\hat{H}_\mathrm{I}\,t}\, \mathrm{e}^{-\mathrm{i}\,\hat{H}_\mathrm{S}\,t}\, \hat{M}_\mathrm{x}\, \mathrm{e}^{\mathrm{i}\,\mathrm{H_S}\,t}\right). \tag{5.12}$$

$\exp(\mathrm{i}\,\hat{H}_\mathrm{S}\,t)$ generates a rotation about the z-axis by the angle $\omega_0\, t$. So we can simplify

$$G(t) = \cos(\omega_0\, t)\, \mathrm{tr}\left(\mathrm{e}^{\mathrm{i}\,\hat{H}_\mathrm{I}\,t}\, \hat{M}_\mathrm{x}\, \mathrm{e}^{-\mathrm{i}\,\hat{H}_\mathrm{I}\,t}\, \hat{M}_\mathrm{x}\right) + \sin(\omega_0\, t)\, \mathrm{tr}\left(\mathrm{e}^{\mathrm{i}\,\hat{H}_\mathrm{I}\,t}\, \hat{M}_\mathrm{x}\, \mathrm{e}^{-\mathrm{i}\,\hat{H}_\mathrm{I}\,t}\, \hat{M}_\mathrm{y}\right). \tag{5.13}$$

The second term vanishes because a π-rotation about the x-axis changes the sign of $\hat{M}_\mathrm{y}$ but not of $\hat{M}_\mathrm{x}$ and the other way round for a y-rotation. We get the reduced correlation function about ω_0

$$G_1(t) = \mathrm{tr}\left(\mathrm{e}^{\mathrm{i}\,\hat{H}_\mathrm{I}\,t}\, \hat{M}_\mathrm{x}\, \mathrm{e}^{-\mathrm{i}\,\hat{H}_\mathrm{I}\,t}\, \hat{M}_\mathrm{x}\right). \tag{5.14}$$

By substituting

$$G(t) = G_1(t)\, \cos(\omega_0\, t) \tag{5.15}$$

in equation (5.10) one gets

$$G_1(t)\, \cos(\omega\, t) = \frac{2}{\pi\, A} \int_{-\omega_0}^\infty \cos((\omega_0 + u)\, t)\, f(\omega_0 + u)\, \mathrm{d}u. \tag{5.16}$$

by substituting $h(u) = F(\omega_0 + u)$ and extending the lower limit of the integral to $-\infty$, which is legitimate if the line width is small against ω_0 we arrive at

$$G_1(t) = \frac{2}{\pi\, A} \int\limits_{-\infty}^{\infty} \cos(u\, t)\, h(u)\, \mathrm{d}u. \tag{5.17}$$

The moments of the new distribution $h(u)$ about ω_0 are now given as

$$\mathcal{M}_n = \int\limits_{-\infty}^{\infty} h(u)\, u^n \mathrm{d}u. \tag{5.18}$$

The odd moments vanish so via the Fourier transform we get

$$\mathcal{M}_{2\,n} = (-1)^n \frac{\pi}{2}\, A \left[\frac{\mathrm{d}^{2\,n}\, G_1(t)}{\mathrm{d}t^{2\,n}}\right]_{t=0} = \frac{(-1)^n}{G_1(0)} \left[\frac{\mathrm{d}^{2\,n}\, G_1(t)}{\mathrm{d}t^{2\,n}}\right]_{t=0}. \tag{5.19}$$

We obtain the moments by expanding (5.17) in powers of t. The expansion coefficients are traces of polynomial functions of $\hat{H}_\mathrm{I}$ and $\hat{M}_x$. The trace operation is invariant to basis transforms. Therefore the moments are independent of the choice of basis they are calculated in. So we can choose e.g. a basis where the m_{Ii} of the single spins i are good quantum numbers. Thus we circumvent the problem of finding the eigenstates of the complete Hamiltonian (5.2). By expanding the equation of motion for the magnetization

$$\frac{\mathrm{d}\,\hat{M}_x}{\mathrm{d}t} = \mathrm{i}\left[\hat{H}_\mathrm{I}, \hat{M}_x\right] \tag{5.20}$$

into a series

$$\hat{M}_x(t) = \hat{M}_x(0) + \hat{M}_x^{(1)}(t) + \cdots + \hat{M}_x^{(n)}(t) \tag{5.21}$$

where the respective parts can be iterated by

$$\hat{M}_x^{(n)}(t) = \mathrm{i} \int\limits_0^t \left[\hat{H}_\mathrm{I}, \hat{M}_x^{(n-1)}(t')\right] \mathrm{d}t', \tag{5.22}$$

we acquire the $(2\,n)^{\mathrm{th}}$ derivative of $G_1(t)$

$$\left[\frac{\mathrm{d}^{2\,n}\, G_1(t)}{\mathrm{d}t^{2\,n}}\right]_{t=0} = \mathrm{i}^{2\,n}\, \mathrm{tr}\Big\{ \overbrace{[\hat{H}_\mathrm{I}, [\hat{H}_\mathrm{I}, [\ldots, [\hat{H}_\mathrm{I}}^{2\,n \text{ times}}, \hat{M}_x] \ldots] \hat{M}_x] \hat{M}_x] \Big\}. \tag{5.23}$$

The second moment is therefore

$$\mathcal{M}_2 = -\frac{\mathrm{tr}\{[\hat{H}_\mathrm{I}, \hat{I}_\mathrm{x}]^2\}}{\mathrm{tr}\{\hat{I}_\mathrm{x}^2\}} \tag{5.24}$$

where we replace $\hat{M}_x$ by the spin operator $\hat{I}_x$ which is proportional to it.

To calculate the commutator $[\hat{H}_\mathrm{I}, \hat{I}_\mathrm{x}]$ for our specific case we insert the interaction Hamiltonian (5.7) finding

$$[\hat{H}_\mathrm{I}, \hat{I}_\mathrm{x}] = \gamma_\mathrm{e}\,\gamma_\mathrm{n}\,\hbar \sum_{j<k} \frac{3}{2\,r_{jk}^3}\,(1 - 3\,\cos^2(\Theta_{jk}))\,[\hat{I}_\mathrm{z}^j\,\hat{I}_\mathrm{z}^k, \hat{I}_\mathrm{x}^j + \hat{I}_\mathrm{x}^k] \tag{5.25}$$

Since $\hat{I}_\mathrm{x}^j + \hat{I}_\mathrm{x}^k$ commutes with $\underline{\hat{I}}^j\,\underline{\hat{I}}^k$ the commutator $[\hat{H}_\mathrm{I}, \hat{I}_\mathrm{x}]$ is unaffected by any inter bath interaction that commutes with $\hat{I}_\mathrm{x}$. By applying basic commutator relations we simplify (5.25) to

$$[\hat{H}_\mathrm{I}, \hat{I}_\mathrm{x}] = \mathrm{i}\,\frac{3}{2}\gamma_\mathrm{e}\,\gamma_\mathrm{n}\,\hbar \sum_{j<k} \frac{(1 - 3\,\cos^2(\Theta_{jk}))}{r_{jk}^3}\,(\hat{I}_\mathrm{z}^j\,\hat{I}_\mathrm{y}^k + \hat{I}_\mathrm{z}^k\,\hat{I}_\mathrm{y}^j). \tag{5.26}$$

Inserting this into (5.24) we arrive at

$$-\mathrm{tr}\{[\hat{H}_\mathrm{I}, \hat{I}_\mathrm{x}]^2\} = \frac{2}{9}\,\gamma_\mathrm{e}^2\,\gamma_\mathrm{n}^2\,\hbar^2\,I^2(I+1)^2\,(2\,I+1)^N \sum_{j<k} b_{jk}^2, \tag{5.27}$$

$$\mathrm{tr}\{\hat{I}_\mathrm{x}^2\} = \sum_j \mathrm{tr}\{\hat{I}_\mathrm{x}^j\}^2 = \frac{1}{3}\,N\,I\,(I+1)\,(2\,I+1)^N, \tag{5.28}$$

with

$$b_{jk}^2 = \frac{3}{2}\,\frac{(1 - 3\,\cos^2(\Theta_{jk}))}{r_{jk}^3} \tag{5.29}$$

and N is the number of spins measured. Because far away from the surface $\sum\limits_{j<k} b_{jk}^2$ is absolutely convergent we are allowed to rearrange the terms

$$\sum_{j<k} b_{jk}^2 = \frac{1}{2} \sum_{j\neq k} b_{jk}^2 = \frac{1}{2}\,N \sum_k b_{jk}^2 \tag{5.30}$$

The second equality holds if the sum is equal for all spins measured. We arrive at the Van Vleck formula for the second moment [101]

$$\mathcal{M}_2 = \frac{1}{3}\,\gamma_\mathrm{e}^2\,\gamma_\mathrm{n}^2\,\hbar^2\,I(I+1) \sum_k b_{jk}^2. \tag{5.31}$$

We extend the lattice sum to a statistically occupied lattice by introducing a functional

$$F(k,f) = \begin{cases} 1 & \text{if lattice site } k \text{ carries a nuclear spin} \\ 0 & \text{else.} \end{cases} \tag{5.32}$$

f is the concentration of ^{13}C in the lattice. For a partially filled lattice the second moment is then

$$\mathcal{M}_2 = \Delta\omega^2 = \frac{1}{3}\,\gamma_\mathrm{e}^2\,\gamma_\mathrm{n}^2\,\hbar^2\,I(I+1)\sum_k F(k,f)\,b_{jk}^2. \tag{5.33}$$

On average $F(k,f)$ is replaced by the probability to find a ^{13}C at a lattice site f. $\overline{\mathcal{M}_2}$ is therefore proportional to f and therefore

$$\overline{\Delta\omega} \sim \sqrt{f}. \tag{5.34}$$

The exact dependence is obtained by taking the whole lattice sum

$$\sum_k b_{jk}^2 \approx 1.278 \cdot 10^{59}\,\mathrm{m}^{-6} \tag{5.35}$$

which is convergent after taking roughly 4 nm around the NV site into account. Plugged into (5.33) we get

$$\Delta\omega = \gamma_\mathrm{e}\,\gamma_\mathrm{n}\,\hbar\,1.787 \cdot 10^{23}\,\sqrt{f}\,\mathrm{MHz} \tag{5.36}$$

As can be seen from fig. 5.2 this fits well to the experimental data.

5.0.2. Conclusion

We have conclusively shown that ^{13}C is the main source of decoherence of the NV center in otherwise pure diamond. In highly isotopically purified crystals (under 0.01 % ^{13}C) other sources like uncontrollable defects or fluctuating charges become relevant. Coherence times of up to $T_2 = 1.8\,\mathrm{ms}$ have been observed in such isotopically engineered diamonds [5]. This suggests that NVs that are separated some tens of nanometers can directly be coupled in such crystals (sec. 6). It also allows the detection of external magnetic fields with a sensitivity up to $4\,\mathrm{nT}/\sqrt{\mathrm{Hz}}$ at spatial resolution around 1 nm.

6. A Quantum Register Based on Coupled NV Centers

Because the number of nuclear spin qubits accessible from the NV center is severely limited (sec. 2.1.2) one essential step in scaling up the quantum register is the implementation of quantum gates connecting multiple NV centers.

So we aim to couple two close by color centers via their magnetic dipole dipole coupling to increase the local register size. To generate entanglement the coupling has to be faster than the decoherence of the system. The coupling scales like

$$E_{\mathrm{dip}} \sim \frac{\mu_0 \, \mu_{\mathrm{B}}^2 \, g_{\mathrm{NV}}^2}{2 \, \hbar \, |\underline{r}|^3} \tag{6.1}$$

with $|\underline{r}|$ the distance between the spins. μ_0 is the permeability of free space, μ_{B} the Bohr magneton and g_{NV} the electron g-factor. At a distance of 10 nm this is about 70 kHz. This corresponds to a time scale of 14.3 μs for the coupling. Diamond can be isotopically purified to such degrees that the decoherence process is not governed by the nuclear spin bath anymore. In such diamonds T_2 times in the order of ms where reported [5] so at a NV-NV distance of ≈ 10 nm the creation of entanglement is achievable.

The primary experimental challenge is to implant Nitrogen such that exactly two NV centers form within a few nm from one another. If the magnetic field is aligned along one NV axis the other three possible directions are spectrally degenerate, thus they can not be addressed selectively without the application of a magnetic field gradient, which is not applicable at the moment. With two addressable centers every additional one would introduce redundancy, but due to different coupling between pulse errors are inevitable.

In essence there are two possibilities to implant nitrogen ions into the diamond in order to generate such a close by pair. Either at low implantation energy nitrogen is deposited few nm below the diamond surface or at high energies μm deep into the bulk material. Shallow implanted nitrogen ions can deterministically be placed close by each other by implanting through a photoresist mask or an AFM tip with around 20 nm resolution [78]. But the NV yield after annealing is only in the order of a few percent [71]. Thus many

nitrogen ions have to be implanted in order to generate a close by pair with an acceptable probability. The untransformed nitrogen atoms then contaminate the environment of the NVs, lowering their coherence time. Even if carbon ions are implanted after a few nitrogen ions the shallow NV feel electron spins at the surface of the crystal. This limits the coherence properties as well. Due to the large number of vacancies created along the implantation path at high energies the NV creation efficiency is increased to $\approx 20\%$ after annealing. But the straggle of the ions increases by 0.46 nm/keV implantation energy preventing the deterministic placement of the NV [54]. Nevertheless exceptionally long coherence times are only observed deep within the diamond crystal where surface effects are negligible.

In the reported case [73] patterns of high energy nitrogen ions have been implanted into 99.99% isotopically pure ^{12}C diamond. Fig. 6.1 shows such a pattern with two NVs per site on average. The presence of two close by NVs was confirmed by measuring the fluorescence autocorrelation function $g^2(\tau)$ as well as by stimulated emission depletion microscopy (STED) [84].

The two NV system is described by the Hamiltonian

$$\hat{H} = \overbrace{\sum_{i=\{\mathrm{A,B}\}} \underline{\hat{S}}_i \, \underline{\underline{D}}_i \, \underline{\hat{S}}_i + \mu_\mathrm{B} \, g_\mathrm{NV} \, \underline{B} \, \underline{\hat{S}}_i}^{\hat{H}_\mathrm{A}+\hat{H}_\mathrm{B}} + \overbrace{\frac{\mu_0 \, \mu_\mathrm{B}^2 \, g_\mathrm{NV}^2}{2 \, \hbar \, |\underline{r}|^3} \left(3(\underline{\hat{S}}_\mathrm{A} \, \underline{r}) \, (\underline{\hat{S}}_\mathrm{B} \, \underline{r}) - \underline{\hat{S}}_\mathrm{A} \, \underline{\hat{S}}_\mathrm{B} \right)}^{\hat{H}_\mathrm{dip}} \tag{6.2}$$

Here $\underline{\underline{D}}_i$ is the zero field splitting tensor. $\underline{\underline{D}}_\mathrm{A}$ is assumed to be aligned with the magnetic field while $\underline{\underline{D}}_\mathrm{B}$ is tilted by the tetrahedron-angle of 109.5°. Due to the tilted zero field tensor the spin states are mixed in the energy eigenbasis. Due to the huge $D \sim \hat{S}_\mathrm{z}^2$ part of the zero field splitting the mixing of $|0\rangle$ with $|\pm 1\rangle$ is negligible. The optical detection of the spin state remains possible for the tilted NV. We name the energy eigenvalues of $\mathrm{NV_B}$ $|0\rangle_\mathrm{B}$, $|+\rangle_\mathrm{B}$ and $|-\rangle_\mathrm{B}$. Due to the tilted zero field splitting tensor the ODMR resonance lines of the two centers are separated (fig. 6.1). Thus allowing selective control over the two spin states.

To measure the coupling strength it is appropriate to measure Ramsey fringes (sec. 3.7) on $\mathrm{NV_A}$ while the $\mathrm{NV_B}$ is prepared in one of its 3 energy eigenstates The A component of the dipole-dipole interaction provides an offset field dependent on the spin state of $\mathrm{NV_B}$ at the site of $\mathrm{NV_A}$, thus the detuning frequency observed by the Ramsey fringes is

$$\Delta\omega_\mathrm{A} = \Delta\omega_\mathrm{A}^\mathrm{det} + \omega_\mathrm{AB}^\mathrm{dip} \, m_\mathrm{S}^\mathrm{B}. \tag{6.3}$$

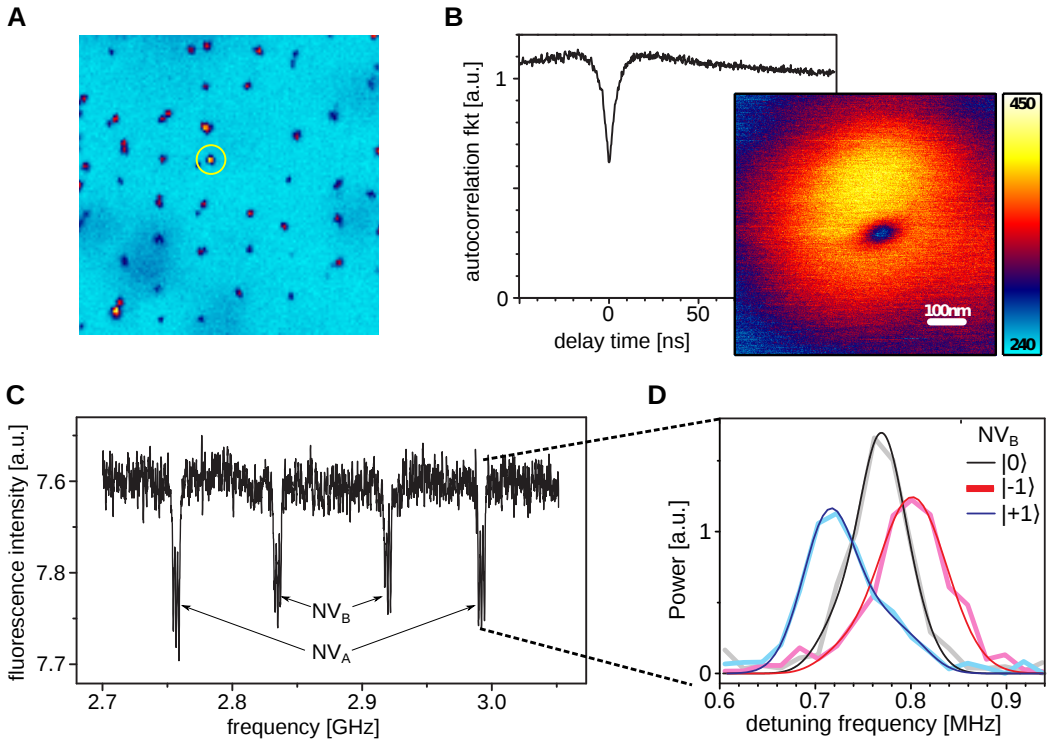

Figure 6.1.: **A** Confocal scan of the nitrogen implanted area. Red dots mark single centers while more yellowish dots represent multiple NVs inside the confocal spot. The encircled spot is the NV pair the experiments were conducted on. **B** shows the two point autocorrelation function confirming there are two emitters inside the focus by dropping to 0.5 instead of 0 at $\tau = 0$. The picture is the STED image of the pair site. The elongation of the spot indicates two NVs but they are not resolved. **C** ODMR spectrum of the two NV centers. Due to different orientation on the lattice the degeneracy of the $m_S = \pm 1$ energy levels is lifted by a small magnetic field ($\approx 43\,\mathrm{G}$) along the axis of $\mathrm{NV_A}$. **D** splitting of one spectral line due to the interaction between the two color centers obtained from the fast Fourier transform of the Ramsey fringes of $\mathrm{NV_A}$ after initializing $\mathrm{NV_B}$ in $m_S = \{0, \pm 1\}$ respectively.

The Fourier transform of the three experiments is shown in fig. 6.1. This method measures the $\hat{S}_z \otimes \hat{S}_z$-component of the interaction. Non axial interaction enters as second order perturbation and is thus negligible. In order to further analyze the coupling the separation vector $\underline{r}$ has to be determined.

6.1. Relative Position of the Two NVs

In order to infer the separation vector $\underline{r}$ we need to take a closer look on the system's Hamiltonian (6.2). As long as the magnetic field is aligned with the axis of a single NV the system behaves as described in sec. 2.1 but as soon as there is a component perpendicular to the axis $B_\perp$ the quantization axis of the NV tilts away from the NV axis. In first order this does not influence the magnetic moment of the $m_S = \pm 1$ states. The $m_S = 0$ state however acquires a magnetic moment perpendicular to the NV axis that is proportional to $B_\perp$. This magnetic moment influences the dipole-dipole coupling strength depending on the amplitude and direction of $B_\perp$. For at least one of the two NV centers $B_\perp$ is always present because the zero field splitting tensors $\underline{\underline{D}}_i$ are tilted against each other. By the magnetic field dependence of the interaction strength the separation vector $\underline{r}$ can thus be determined. From the diagonalized Hamiltonian the interaction strength of the respective transitions is computed as

$$\omega_{-1-1} = [E(|-1\,0\rangle - |0\,0\rangle) - E(|-1\,-1\rangle - |0\,-1\rangle)]/\hbar \tag{6.4}$$
$$\omega_{-1+1} = [E(|-1\,0\rangle - |0\,0\rangle) - E(|-1\,+1\rangle - |0\,+1\rangle)]/\hbar \tag{6.5}$$
$$\omega_{+1-1} = [E(|+1\,0\rangle - |0\,0\rangle) - E(|+1\,-1\rangle - |0\,-1\rangle)]/\hbar \tag{6.6}$$
$$\omega_{+1+1} = [E(|+1\,0\rangle - |0\,0\rangle) - E(|+1\,+1\rangle - |0\,+1\rangle)]/\hbar. \tag{6.7}$$

These energies are fitted to the experimental results by moving $\mathrm{NV_B}$ around while $\mathrm{NV_A}$ resides at the center of the coordinate system. This leaves an ambiguity along an equipotential line of the interaction Hamiltonian. Acquisition of a second data set with different field direction lifts this ambiguity. By rotating the magnetic field the quantization axis of both NVs is tilted. Thus a different projection of the interaction Hamiltonian is detected. $\mathrm{NV_B}$ is located at the crossing of the two equipotential lines. The interaction energies corresponding to the double transition of $\mathrm{NV_B}$

$$\omega_{-1\mathrm{d}} = [E(|-1\,-1\rangle - |0\,-1\rangle) - E(|-1\,+1\rangle - |0\,+1\rangle)]/\hbar \tag{6.8}$$
$$\omega_{+1\mathrm{d}} = [E(|+1\,-1\rangle - |0\,-1\rangle) - E(|+1\,+1\rangle - |0\,+1\rangle)]/\hbar \tag{6.9}$$

should remain unaffected by the magnetic field strength. This is measured to verify the model.

Experimentally the interaction strength is measured best by double electron electron resonance (DEER) (sec. 3.7), which is designed to detect the z-component of interaction between two electron spins. This echo based measurement scheme is making use of the normally two orders of magnitude longer

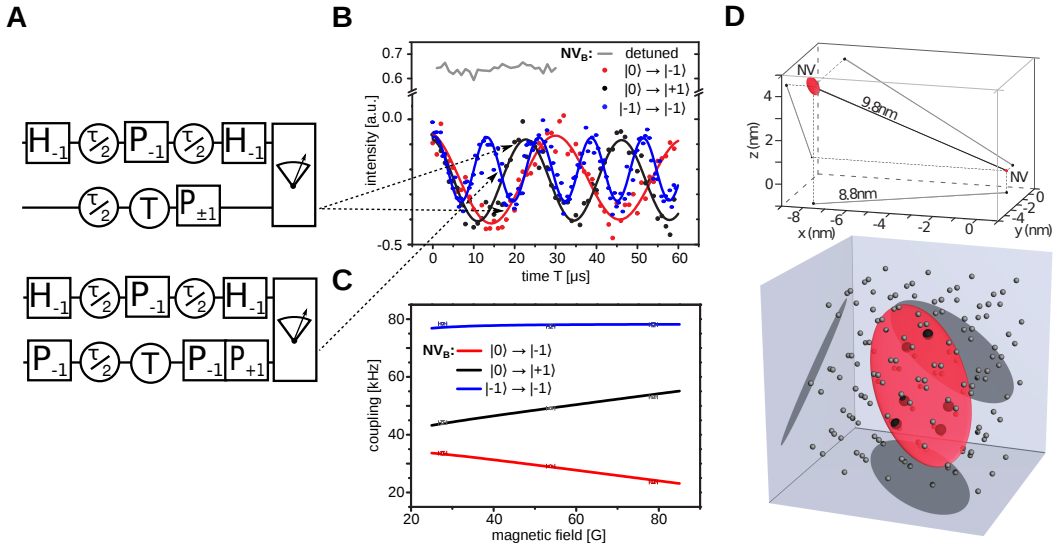

Figure 6.2.: **A** Quantum circuit of the DEER sequence. The indices (± 1) indicate whether the gate is implemented on the transition $|0\rangle \leftrightarrow |-1\rangle$ or $|0\rangle \leftrightarrow |+1\rangle$. **B** exemplary DEER measurement results for one magnetic field direction. As expected the oscillation corresponding to the double transition of NV_B has the double frequency of the single transitions. **C** Magnetic field dependence of the interaction strength for $\underline{B}$ aligned to the axis of NV_A. The model is fitted to the single transition data. It describes the double transition data very well. **D** Reconstruction of the system geometry. Details of the uncertainty area are shown on the lower part. The possible location sites are highlighted as bigger spheres.

T_2 time instead of T_2^* of the Ramsey fringes. As an adaption to the NV's $S = 1$ the sequence is carried out three times for each of the two transitions of NV_A the "echo spin" (fig. 6.2), flipping NV_B from $|0\rangle$ to $|-1\rangle$, then to $|+1\rangle$ and finally from $|-1\rangle$ to $|+1\rangle$. In fig. 6.2 the measurement data with the fitted field dependence is depicted showing very good agreement with the model.

As depicted in fig. 6.2 this method narrowed the potential location of NV_B down to six lattice sites within the measurement error. It is located 9.8 nm apart from NV_A, 8.8 nm in the lateral direction. This was confirmed optically by fluorescence lifetime imaging (FLIM) analysis [17]. This method relies on different fluorescence lifetimes of the emitters inside the confocal spot. It collects lifetime information of every pixel. In the case of two emitters with different fluorescence lifetime two exponentials can be fitted to the data. The

amplitudes of the two exponentials contain the pixel information for two separate images of the two emitters. A 2D correlation of these two images results in a Gaussian like distribution. The vector from the center to the peak of that Gaussian is the displacement vector of the two centers. In order to introduce different radiative lifetimes to the two NV centers we make use of its spin dependence of around 12 ns for the $m_S = 0$ states and 7 ns for $m_s = \pm 1$ [8]. We have to make sure that one NV is in $|0\rangle$ the other is not. This is achieved by moving to higher magnetic fields (700 G in our case). While the magnetic field is aligned to NV_A is causes mixing of $|0\rangle$ and $|\pm 1\rangle$ for NV_B. For NV_A $|0\rangle$ remains a good quantum number and the system is polarized into this eigenstate. NV_B however is polarized into a mixture of $|0\rangle$ and $|\pm 1\rangle$. The radiative lifetime of NV_B is shortened while NV_A's is not, thus enabling the FLIM analysis. For our NV pair this resulted in a lateral distance of 8 ± 3 nm. This fits very well to the 8.8 nm measured by the DEER method.

6.2. Entanglement Generation

The source of the superiority of quantum computing over classical computing is entanglement. In order to harness its possibilities one has at least to be able to generate bipartite entanglement between every pair of qubits in a register. Hence we devised a quantum algorithm that acts as an entanglement gate between the two NV centers. It is again based on the DEER sequence. Both NVs are initialized into $|0\rangle$.

$$|\Phi\rangle_{\mathrm{i}} = |00\rangle \tag{6.10}$$

Instead of a Pauli gate we apply a Hadamard gate on NV_B right after the Pauli gate of the Hahn echo of NV_A generating the state

$$|\Phi\rangle_1 = \frac{1}{2}(|-1-1\rangle + |0-1\rangle + \mathrm{i}\,(|-10\rangle + |00\rangle)) \tag{6.11}$$

By fixing the echo duration $\tau = 2\,(2\,n-1)\,\pi/(E_{\mathrm{dip}}\,\delta B)$ with $n \in \mathbb{N}$ we allow the dipole-dipole coupling to swap the superposition on NV_B between the two NVs. Thus implementing a phase shift gate resulting in

$$|\Phi\rangle_2 = \frac{1}{2}(\mathrm{i}\,(|-1-1\rangle + |-10\rangle) + |0-1\rangle + |00\rangle). \tag{6.12}$$

The final Hadamard gate on NV_A transforms the system state into a maximally entangled state

$$|\Phi\rangle_{\mathrm{f}} = \frac{1}{\sqrt{2}}\,(\mathrm{i}\;|-1-1\rangle - |00\rangle) \tag{6.13}$$

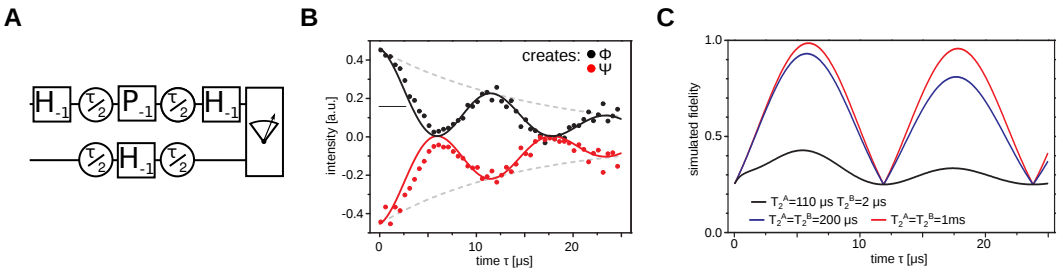

Figure 6.3.: **A** Quantum circuit of the entanglement sequence. The indices (± 1) indicate whether the gate is implemented on the transition $|0\rangle \leftrightarrow |-1\rangle$ or $|0\rangle \leftrightarrow |+1\rangle$. **B** comparison of the measured population (dots) with the simulated time dependence (solid lines). In order to generate the Ψ state the final Hadamard gate has to be substituted by a $3\,\pi/2$ pulse. **C** Simulated fidelity of the generated state. The black curve represents the present experimental conditions. If the T_2 time reaches $200\,\mu$s $F = 0.9$ is reached. for T_2 of 1 ms the fidelity approaches 1.

If this final Hadamard gate is replaced by a $3\,\pi/2$ pulse a Ψ type entangled state

$$|\Psi\rangle_{\mathrm{f}} = \frac{1}{\sqrt{2}} \left(\mathrm{i}\,|-10\rangle - |0-1\rangle\right) \tag{6.14}$$

is generated instead.

For experimental purposes the echo duration is modulated to observe an oscillation between the not entangled superposition state of $\mathrm{NV_B}$ $(\mathrm{i}\,|0-1\rangle - |00\rangle)/\sqrt{2}$ at $\tau = 2\,(2\,n)\,\pi/(E_{\mathrm{dip}}\,\delta B)$ with $n \in \mathbb{N}$ and the Bell state (6.13). Examining the occupation probabilities of the two states we see that $|\Phi\rangle_{\mathrm{f}}$ has the lower fluorescence intensity because both NVs feature a mixture between the $|0\rangle$ and $|-1\rangle$ state while in the unentangled state $\mathrm{NV_A}$ is in the $|0\rangle$ state. For the Ψ states the superposition state of $\mathrm{NV_B}$ is $(\mathrm{i}\,|-1-1\rangle - |-10\rangle)/\sqrt{2}$ with lower intensity than (6.14) (fig. 6.3).

The scheme is limited by the coherence time of the single NVs in comparison to the duration of the entanglement gate, especially since to swap the coherence on a working transition for a state tomography (sec. 2.1.2) the entanglement gate has to be applied a second time. Because the T_2 times of the measured NV pair are surprisingly short ($T_2^{\mathrm{A}} = 110\,\mu$s and $T_2^{\mathrm{B}} = 2\,\mu$s) no entanglement could be created experimentally. We simulated the result for various coherence times by applying the unitary transformations for the gates to an initially polarized state $\hat{\rho}_i = |00\rangle\langle 00|$. The free induction times where modulated

by applying the time evolution operator of the closed system Hamiltonian (6.2). To incorporate the decay of the coherences the result of the closed free induction is multiplied by an array of exponential decay functions with the corresponding decay constants ($1/T_2^{\mathrm{A}}$, $1/T_2^{\mathrm{B}}$ for state including $|0\rangle\langle\pm1|_{\{\mathrm{A,B}\}}$, $2/T_2^{\mathrm{A}}$, $2/T_2^{\mathrm{B}}$ for the double transitions $|\pm1\rangle\langle\mp1|_{\{\mathrm{A,B}\}}$). From these results the expected fidelity of the generated Bell states is calculated. The simulation matches the measured data (fig. 6.3) very well. The maximum fidelity of $F = 0.47$ confirms that no entanglement was created. If however a pair with longer T_2 times was examined the fidelity would reach $F = 0.9$ for $T_2^{\mathrm{AB}} = 200\,\mu\mathrm{s}$. At T_2 times above 1 ms as already observed in isotopically enriched diamond [5] the fidelities above $F = 0.99$ can be expected.

It is possible to improve the ratio of the entanglement gate time to the coherence time by a factor of two by applying the entanglement gate on the double transition. To do that the Hahn echo is carried out on the double transition and $\mathrm{NV_B}$ is flipped from $|-1\rangle$ to $|+1\rangle$. This increases the observed DEER oscillating frequency by a factor of 4 while the coherence time of the double transition is half as long as the single transitions. So even for shorter coherence times than $200\,\mu\mathrm{s}$ high fidelity entanglement between two NV spins is feasible. In order to exploit T_2 rather than T_2^* of $\mathrm{NV_B}$ the entanglement sequence can be modified such that on both NVs a Hahn echo is implemented. If the τ again is fixed to $\tau = 2\,(2\,n-1)\,\pi/(E_{\mathrm{dip}}\,\delta B)$ the Bell state

$$|\Phi\rangle_{\mathrm{f}} = \frac{1}{\sqrt{2}}\left(|-1\,-1\rangle - |00\rangle\right) \tag{6.15}$$

is generated. Yet a different approach would be to implement the entanglement gate at zero magnetic field. Here the energy eigenstates are $|0\rangle$ and $|-1\rangle \pm |+1\rangle$. Thus by applying a π-pulse between $|0\rangle$ and $|-1\rangle + |+1\rangle$ the "double quantum coherence" is already created. Furthermore the spectra of the two NVs are degenerate. Mutual flip flops thus are allowed. Instead of exploiting only the axial interaction ($\hat{S}_{\mathrm{z}} \otimes \hat{S}_{\mathrm{z}}$) as with Ramsey fringes and the DEER sequence the off diagonal part of the interaction Hamiltonian now takes the leading role. Depending on the separation vector of the two NVs it can be stronger as well as weaker than the axial component. Entanglement is generated just by waiting for a $\pi/2$ partial swap to occur. Disadvantage of this scheme is that for many quantum algorithms the single nodes have to be addressed individually. This is not possible at zero field. In order to implement algorithms the magnetic field has to be switched during the computation. Due to long rise times of the magnets this is not experimentally feasible at the moment.

7. Quantum-Non-Demolition Measurement

For many quantum algorithms it is sufficient to read the result by performing a time average of many repetitions of the same experiment. That way statistical information about the final spin state is gathered and thus the entries of the density operator are measured. The precision of such an integrating measurement is in our case limited by shot noise from the read out laser. Due to its statistical nature the measurement accuracy is proportional to $1/\sqrt{N}$ if N is the number of repetitions. One step further would be to do a projective measurement of the qubit after each run of the algorithm. Two types of such projective measurements are distinguished.

Single shot read out projects the system onto an eigenstate and reads out the result, but destroys it in the process. It is commonly featured by photon qubits where the Photon is destroyed by the detection. To be able to perform single shot readout on a quantum register enables a wide field of quantum experiments. One can for example test Bell type inequalities [10] or perform teleportation experiments [12].

Quantum-non-demolition (QND) measurement projects the system onto an eigenstate and reads out the state without destroying it. The projected qubit can be manipulated after the read out starting from the eigenstate it was projected in, this allows e.g. to measure the quantum zeno effect [65]. Some types of quantum error correction algorithms rely on projective measurements as well.

Are projective measurements feasible for the NV center? To answer this question all possible qubits of the register have to be checked, starting with the electron spin.

QND measurement of the electron spin can be ruled out because the optical readout polarizes the qubit into $m_S = 0$. To implement single shot readout however the transition in the alternative decay channel has to be observed directly. This can be realized by increasing the collection efficiency of the fluorescence light and/or the radiative lifetime would be reduced. We would benefit both ways by putting the NV center inside an optical cavity. Most of the fluorescence light is emitted into the cavity mode and by the Purcell effect

the radiative lifetime is lowered. At the moment we collect about 2 % of the fluorescence light which means roughly 1 photon in 4 μs while the decay via the alternate channel takes about 255 ns. Even a low Q cavity with a quality factor $Q \approx 10$ would already be sufficient to demonstrate optical single shot read out of the NV's electron spin. Unfortunately there are no such systems feasible at the moment.

For nuclear spin qubits direct measurement is not possible on a single spin level. They have to be read via the electron spin. So single shot is feasible as soon as it is for the electron spin by swapping the nuclear spin state onto the electron spin. If the readout of the electron qubit could be decoupled from the nuclear spin dynamic the nuclear state could be extracted from the time averaged measurement of the electron qubit by correlating the electron qubit with a nuclear qubit. This process would be an implementation of a quantum-non-demolition measurement because only the ancilla qubit is reseted by the readout. In the following we discuss under which conditions such a measurement scheme is possible.

At low magnetic fields ($B < 100$ G) laser irradiation polarizes the electron spin into $m_S = 0$ and scrambles the state of nuclear spins coupling to the NV. Weak coupling carbon nuclear spins can be used for a repetitive read out scheme [51]. As detailed below the loss of the nuclear spin state is due to mixing of the nuclear and electron spin states in the electronic excited state of the NV near its level anti crossing (LAC) at ~ 500 G. By increasing the magnetic field well above this we effectively decouple the nuclear spin dynamics from the electron spin. This enables us to conserve the nuclear spin state of the nitrogen atom during a laser pulse. The readout scheme follows suit as depicted in fig. 7.1. We correlate the electron spin state with the nuclear spin state we want to read by applying a CNOT gate. The nuclear spin selective microwave pulse flips the electron state from $|0_\mathrm{e}\rangle$ to $|-1_\mathrm{e}\rangle$ depending on the nuclear spin state. Then we read out and repolarize the electron spin by shining a short laser pulse on the system. One such step gives us 0.2 photons on average. Thus we have to repeat this process. Because the nuclear spin state remains virtually untouched by the short laser pulse we accumulate information about one single nuclear state. The CNOT pulse takes 1300 ns the read out/reinitialize laser pulse has a duration of 200 ns but 1000 ns wait time is necessary to make sure the NV center has returned into its electronic ground state. 2000 repetitions are necessary to estimate the spin state. Thus the measurement takes 5 ms. Continuous repetition of this scheme reveals two discrete fluorescence levels (fig. 7.1) revealing the projective character of the measurement. To quantify the measurement data, we take the histogram of the intensities time trace. Revealing two distinct Poissonian distributions with a slight overlap (fig. 7.1).

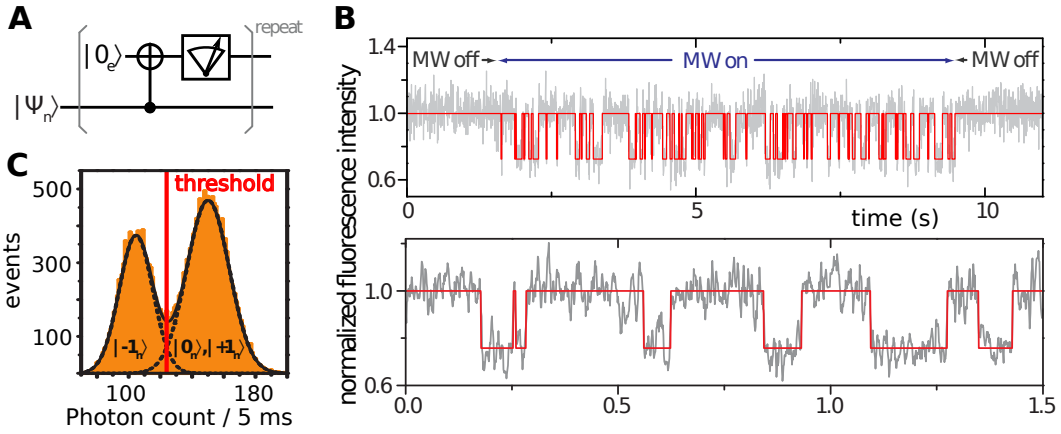

Figure 7.1.: **(A)** The quantum circuit of the single shot read out of the nuclear spin state $|\Psi_n\rangle$. **(B)** The normalized fluorescence time traces of continuous readout. Each data point represents 2000 integrated repetitions of the scheme corresponding to 5 ms acquisition time. High intensity corresponds to the nuclear spin state $|0_n\rangle$ or $|+1_n\rangle$ the low intensity to $|-1_n\rangle$. Without the microwave pulses the intensity stays high, because the NV is not correlated with the nuclear spin and thus remains in $|0_e\rangle$. **(C)** The photon count histogram shows two Poissonian peaks. The threshold marks the count rate above which the state is counted to be either $|0_n\rangle$ or $|+1_n\rangle$. Below the state is $|-1_n\rangle$.

The readout fidelity reaches $F = 92 \pm 2\,\%$ in our measurements. It is limited by the measurement time for a single acquisition, bound by the T_1 time of the nuclear spin, the fluorescence count rate and the magnetic resonance contrast. Since the ^{14}N nucleus has $I = 1$ we are able to track all three possible spin states by setting the CNOT gate alternating to be conditional to $|-1_n\rangle$, $|0_n\rangle$ and $|+1_n\rangle$. Thus we have three fluorescence traces that determine the full state of the nuclear spin as depicted in fig. 7.2. By collecting statistics of the quantum jumps we are able to tomograph the full density matrix of the nuclear spin state.

A consecutive measurement has a probability of $F^2 =\approx 82.5\,\%$ to give the same result as the measurement before. Application of a π-pulse on the nuclear spin drops the probability to $\approx 33\,\%$. Thus Rabi oscillations of the nuclear spin can be detected (fig. 7.3). The full Rabi contrast is not realized because the NV is sometimes switched from NV^- to NV^0 by the laser, thus scrambling the spin state. Truncation of the occurrences of NV^- gives the full contrast [102].

The high probability to return the same result in a consecutive measurement

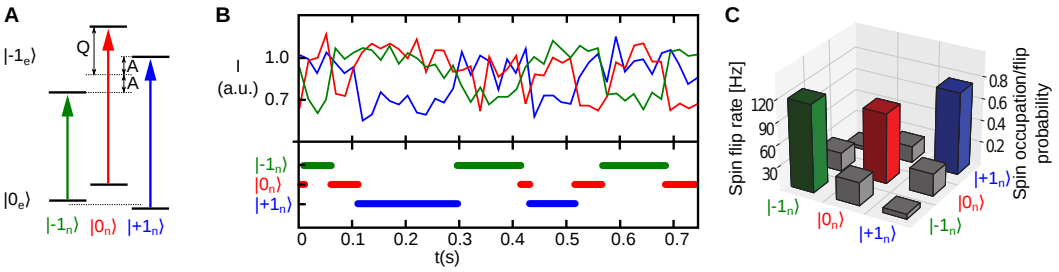

Figure 7.2.: **A** Schematic of the hyperfine transitions that have to be addressed to implement the CNOT gate controlled by the respective nuclear spin state. **B** Time trace of all three nuclear spin levels $m_I = \{0, \pm 1\}$. In the lower half the measured spin state is indicated. The violation of the $\Delta m_I = \pm 1$ selection rule at $t = 3\,\mathrm{s}$ as well as the "state conflict" at $t = 0.34\,\mathrm{s}$ may be due to a fast double jump faster than our $15\,\mu\mathrm{s}$ detection interval. **C** Tomography of the states density matrix deduced from the jumping rates and dwell times.

hints, that the measurement is a QND measurement. To perform a QND measurement in essence 3 requirements to the system Hamiltonian have to be met [48, 20]. The Hamiltonian is

$$\hat{H} = \underbrace{D\,\hat{S}_\mathrm{z}^2 + g_\mathrm{e}\,\mu_\mathrm{B}\,B_\mathrm{z}\,\hat{S}_\mathrm{z}}_{\hat{H}_\mathrm{e}} + \underbrace{Q\,\hat{I}_\mathrm{z}^2 + g_\mathrm{n}\,\mu_\mathrm{n}\,B_\mathrm{z}\,\hat{I}_\mathrm{z}}_{\hat{H}_\mathrm{n}} + \overbrace{\underbrace{\hat{S}\,\underline{\underline{A}}\,\hat{I}}_{\hat{H}_\mathrm{hf}} + \hat{H}_\mathrm{p}}^{=\hat{H}_\mathrm{I}} \tag{7.1}$$

with $\hat{H}_\mathrm{e}$ the NV's Hamiltonian, $\hat{H}_\mathrm{n}$ the nitrogen Hamiltonian, $\hat{H}_\mathrm{hf}$ the hyperfine interaction and $\hat{H}_\mathrm{p}$ the control pulses. $\hat{H}_\mathrm{hf}$ and $\hat{H}_\mathrm{p}$ form the full interaction Hamiltonian $\hat{H}_\mathrm{I}$.

The first requirement is that the probe observable (in our case $\hat{S}_\mathrm{z}$) must be influenced by the observable ($\hat{I}_\mathrm{z}$) we want to measure. That means $\hat{H}_\mathrm{I}$ has to depend on $\hat{I}_\mathrm{z}$ and must not commute with $\hat{S}_\mathrm{z}$

$$[\hat{S}_\mathrm{z}, \hat{H}_\mathrm{I}] \overset{!}{\neq} 0 \tag{7.2}$$

This is fulfilled for the CNOT gate. With preparing the electron spin in a superposition state rather than in an energy eigenstate this dependence can be tuned. In the equal superposition the population of the electron spin is independent of the nuclear spin state. The strength of the QND measurement can be tuned this way enabling us to conduct weak measurements as well [3].

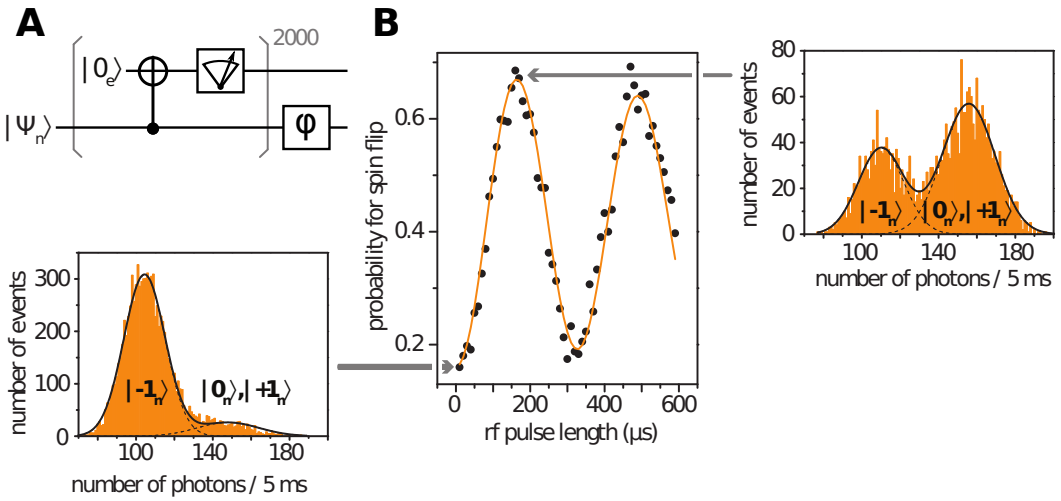

Figure 7.3.: **(A)** The quantum circuit of the Rabi oscillation of the nuclear spin state $|\Psi_n\rangle$. **(B)** shows Rabi oscillation with the histograms of a consecutive measurement to the left with a probability of $\approx 82\,\%$ to find the system in the initial state again. On the right is the histogram after a π-pulse. There is still a $\approx 33\,\%$ chance left to find the initial state again. For an ideal π-pulse the probability should be 0.

The second requirement is that there is no back action on the measured spin by the measurement except projecting it into an eigenstate. Because the measurement imposes maximum uncertainty of the conjugate operators ($\hat{I}_x$ and $\hat{I}_y$) of the observable $\hat{I}_z$. So the system Hamiltonian $\hat{H}$ should not be a function of those. Which is the case if the magnetic field is aligned along the NV axis reducing the Zeeman Hamiltonian to

$$\hat{H}_{Z\,n} = g_n\,\mu_n\,B_z\,\hat{I}_z \tag{7.3}$$

as put in (7.1). Independent from the magnetic field direction the system Hamiltonian becomes a function of $\hat{I}_x$ and $\hat{I}_y$ if the quantization axis of the nuclear spin is not parallel to the NV axis. This limits the choice of nuclear spins we are able to perform a single shot readout with. Strictly speaking the nitrogen spin of the NV itself, ^{13}C spins along the NV axis and on the equatorial plane are a suited. Because otherwise the dipole-dipole interaction with the NV tilts their quantization axis from the NV axis. Tilting of a strong magnetic field from the NV axis in order to realign the quantization axis of the NV and the nucleus leads to mixing of the $|0_e\rangle$ and $|\pm 1_e\rangle$ states, rendering the optical readout impossible. The tilt of the quantization axis however becomes

negligible for weak coupling ^{13}C nuclear spins at high magnetic fields, where $E_{\text{Zeeman}} \gg E_{\text{dipole}}$. If the T_2 times are long enough to execute the CNOT gate QND measurement is in principle possible with weak coupling ^{13}C spins.

The third condition is that the observables of the probe system $\hat{S}_\text{z}$ and the target system $\hat{I}_z$ should not be mixed by any interaction. The interaction Hamiltonian $\hat{H}_\text{I}$ has to commute with the observable

$$[\hat{H}_\text{I}, \hat{I}_\text{z}] \stackrel{!}{=} 0. \tag{7.4}$$

In a perfect QND measurement no quantum jumps would occur after the first measurement. But due to the relaxation dynamics of the nuclear spin we observe quantum jumps as depicted in fig. 7.2. Since purely longitudinal interaction can not be generated exactly by dipole-dipole coupling we slightly lift the requirement by demanding the interaction has to be negligible against the measurement duration i.e. the longitudinal relaxation time T_1 of the nuclear spin has to be much longer than the measurement time

$$[\hat{H}_\text{I}, \hat{I}_\text{z}] \stackrel{!}{=} 0 \Rightarrow T_1 \gg \tau_{\text{readout}}. \tag{7.5}$$

This is the case for the NV-^{14}N system at magnetic fields above 0.4 T. In the following the relaxation mechanisms are discussed.

7.1. Relaxation of the Nitrogen Nuclear Spin

In general two longitudinal relaxation mechanisms are assumed for nuclear spins in solids. They are Flip flop processes with environmental spins and coupling to phonons. In addition the quadrupole splitting of the $I = 1$ nitrogen spin makes it susceptible to variations of the electric field like fluctuating charges as well.

Spin baths are negligible for longitudinal relaxation. The most abundant spin species in the diamond lattice is the ^{13}C spin which has $T_1 \gg 20\,\text{ms}$ and even at natural abundance of 1.1 % it is considered to be very dilute. Otherwise the lattice is spin free except for Nitrogen electron and nuclear spins. They occur with concentrations around 1 ppb, which makes them negligible in average as well [67].

Phonons can be discarded as a relaxation source as well, because in the electronic ground state there is no spin orbit coupling whereas in the excited state at room temperature it is averaged out leaving the electron g-factor [7, 34, 72]. Due to the lack of spin orbit coupling the interaction with phonons is very low, therefore no major effect is expected.

The nuclear quadrupole moment along with the hyperfine coupling might lead to a spin flip upon the change of the electronic state of the NV because this changes the electric field gradient to which the quadrupole moment is sensitive. This effect gets stronger the more the quantization axis of the electronic ground and excited state are tilted from another. Due to symmetry reasons the two hyperfine tensors of ground and excited state should be collinear [96]. So this does not lead to a spin flip as long as there is no other electronic fluctuations in the close proximity of the NV. Ionization of the NV under laser irradiation would cause such a change in the local field. Without further knowledge on such processes we can not predict its effect on the nuclear spin state.

There is one additional mechanism left to cause spin flips of the ^{14}N nuclear spin [96]. To understand this mechanism we take a closer look at the system Hamiltonian. The only part featuring off diagonal entries in the Spin basis with the rf-field Hamiltonian $\hat{H}_p$ off is the hyperfine Hamiltonian $\hat{H}_{\mathrm{hf}}$. We rewrite it as

$$\hat{H}_{\mathrm{hf}} = \underline{\hat{S}}\,\underline{\underline{A}}\,\underline{\hat{I}} = A_{\parallel}\,\hat{S}_{\mathrm{z}}\,\hat{I}_{\mathrm{z}} + A_{\perp}\,(\hat{S}_{+}\,\hat{I}_{-} + \hat{S}_{-}\,\hat{I}_{+}) \tag{7.6}$$

with $\hat{S}_{\pm}$ and $\hat{I}_{\pm}$ the rising and lowering operators of the electron spin and the nuclear spin respectively. We assume farther that the transversal component $A_{\perp}$ of the hyperfine tensor is

$$A_{\perp} \approx A_{\parallel} = A_{\mathrm{E}} \approx 40\,\mathrm{MHz}. \tag{7.7}$$

Because of symmetry reasons the hyperfine tensor can be expected to be axial rather than isotropic. So this isotropy assumption is a worst case estimation. Because there is no actual data available we stick to this approximation as an upper bound. At the level anticrossing (LAC) between the $|0_{\mathrm{e}}\rangle$ and $|\pm 1_{\mathrm{e}}\rangle$ in the excited state at $\mp 500\,\mathrm{G}$ (fig. 7.4) the high field eigenstates mix, thus allowing mutual electron nuclear spin flip flops in certain spin states. With the repeated repolarization of the electron spin state into $|0_{\mathrm{e}}\rangle$ this leads to polarization of the nuclear spin into $|-1_{\mathrm{n}}\rangle$ ($|+1_{\mathrm{n}}\rangle$ at $-50\,\mathrm{G}$) [49]. See fig. 7.4 for a schematic of the state mixing. The probability for such a spin flip in dependence of the magnetic field has the shape of two Lorentzian distributions with maxima at $\pm 500\,\mathrm{G}$ and widths in the order of the hyperfine coupling $A_{\perp}$. The experiments were carried out at 6500 G far away of both LACs. The effect can therefore be considered as roughly equal in the $m_S = \pm 1$ and very small. Nevertheless it is the dominant mechanic due to the absence of other mechanisms

To simulate the effect of the LAC on the ^{14}N nuclear spin state under laser irradiation we apply 3 Hamiltonians. One for the electronic ground $\hat{H}_{\mathrm{G}}$ and

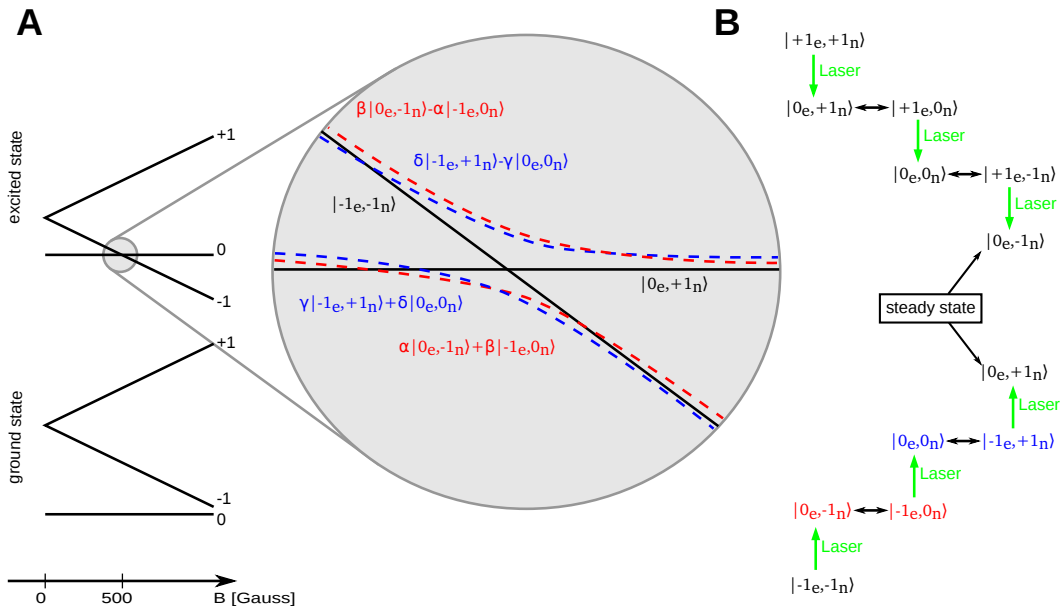

Figure 7.4.: **A** Schematic level scheme of the exited state level-anti-crossing. **B** The decay of the NV-N-system under laser irradiation is sketched here. The upper branch depicts the dynamics at the LAC at $-500\,\mathrm{G}$ where the $|+1\rangle$ state mixes with $|0\rangle$ while the lower branch shows the situation at the LAC at $500\,\mathrm{G}$ as in **A**. The black left-right-arrows indicate flip-flops between electron and nuclear spin while the green arrows depict a passage through the alternative decay channel. It always leads to a reset of the electron spin into the $|0\rangle$ state.

excited state $\hat{H}_\mathrm{E}$ and one for the metastable singlet state $\hat{H}_\mathrm{S}$.

$$\begin{aligned}\hat{H}_\mathrm{G} &= D_\mathrm{G}\,\hat{S}_\mathrm{z}^2 + g_\mathrm{e}\,\mu_\mathrm{B}\,B_\mathrm{z}\,\hat{S}_\mathrm{z} + Q\,\hat{I}_\mathrm{z}^2 + g_\mathrm{n}\,\mu_\mathrm{n}\,B_\mathrm{z}\,\hat{I}_\mathrm{z} + \\ &\quad + A_\mathrm{G}\,(\hat{S}_\mathrm{z}\,\hat{I}_\mathrm{z} + \hat{S}_+\,\hat{I}_- + \hat{S}_-\,\hat{I}_+) \qquad (7.8)\\ \hat{H}_\mathrm{E} &= D_\mathrm{E}\,\hat{S}_\mathrm{z}^2 + g_\mathrm{e}\,\mu_\mathrm{B}\,B_\mathrm{z}\,\hat{S}_\mathrm{z} + Q\,\hat{I}_\mathrm{z}^2 + g_\mathrm{n}\,\mu_\mathrm{n}\,B_\mathrm{z}\,\hat{I}_\mathrm{z} + \\ &\quad + A_\mathrm{E}\,(\hat{S}_\mathrm{z}\,\hat{I}_\mathrm{z} + \hat{S}_+\,\hat{I}_- + \hat{S}_-\,\hat{I}_+) \qquad (7.9)\\ \hat{H}_\mathrm{S} &= Q\,\hat{I}_\mathrm{z}^2 + g_\mathrm{n}\,\mu_\mathrm{n}\,B_\mathrm{z}\,\hat{I}_\mathrm{z} \qquad (7.10)\end{aligned}$$

We start in the electronic ground state with various spin product states. To simulate the effect of the laser we introduce jumping probabilities p_i according

to the measured dwell times

$$t_{G\to E} = 12\,\mathrm{ns} \tag{7.11}$$
$$t_{E\to G} = 20\,\mathrm{ns} \tag{7.12}$$
$$t_{E(0)\to S} = 167\,\mathrm{ns} \tag{7.13}$$
$$t_{E(\pm1)\to S} = 12\,\mathrm{ns} \tag{7.14}$$

and our time grating $\Delta t = 0.1\,\mathrm{ns}$

$$p_i = \frac{\Delta t}{t_i}. \tag{7.15}$$

Based on these jumping probabilities we did a Monte Carlo simulation on the hopping between the three possible electronic states and calculated the closed system dynamics during the dwell times. Because the jumping probability to the metastable singlet state $p_{E\to S}$ is spin state dependent we weighted the jumping probability by the electronic spin state $\rho_{\mathrm{E\,e}}(t) = \mathrm{tr_n}\rho_{\mathrm{E}}(t)$

$$p_{E\to S} = \rho_{\mathrm{E\,e\,11}}\, p_{E(\pm1)\to S} + \rho_{\mathrm{E\,e\,22}}\, p_{E(0)\to S} + \rho_{\mathrm{E\,e\,33}}\, p_{E(\pm1)\to S}. \tag{7.16}$$

The cycling transition between ground and excited state is assumed to be spin conserving [36] while the transition into the metastable state erases the electron spin state but conserves the nuclear spin state $\rho_{\mathrm{S}}(t_{\mathrm{S\,i}}) = \mathrm{tr_e}\rho_{\mathrm{E}}(t_{\mathrm{E\,f}})$. After relaxation from the singlet state the electron spin state is set to $|0_{\mathrm{e}}\rangle$ leaving us with

$$\rho_{\mathrm{G}}(t_{\mathrm{G\,i}}) = |0_{\mathrm{e}}\rangle\langle 0_{\mathrm{e}}| \otimes \rho_{\mathrm{S}}(t_{\mathrm{S\,f}}). \tag{7.17}$$

Whenever the system returns to the ground state the nuclear spin state $\rho_{\mathrm{n}}(t) = \mathrm{tr_e}\rho_{\mathrm{G}}(t_{\mathrm{G\,i}})$ is recorded. This shows the dynamics as depicted in fig. 7.5B. We fitted single exponentials to extract the T_1 times and steady state occupation probabilities of the different nuclear spin states. The magnetic field dependence of T_1 and the steady states are depicted in fig. 7.5B. The expected lifetimes rise approximately quadratic with the magnetic field and are minimal at the excited state LAC ($\approx 50\,\mathrm{mT}$) Which was to be expected for the mixing is a second order perturbation. The $m_S = 0$ state decays approximately twice as fast as $m_S = \pm1$ because it has two allowed transitions instead of one and is thus affected by both LACs. The steady states become equal as the 100 mT between the two LACs gets small against the Zeeman splitting.

The average lifetime measured at 450 mT turned out to be $T_{1\,\mathrm{avg}}^{\mathrm{probed}} = 70.1\,\mathrm{ms}$ for the probed $m_I = -1$ state and $T_{1\,\mathrm{avg}}^{\mathrm{remain}} = 43.4\,\mathrm{ms}$ for remaining unresolved

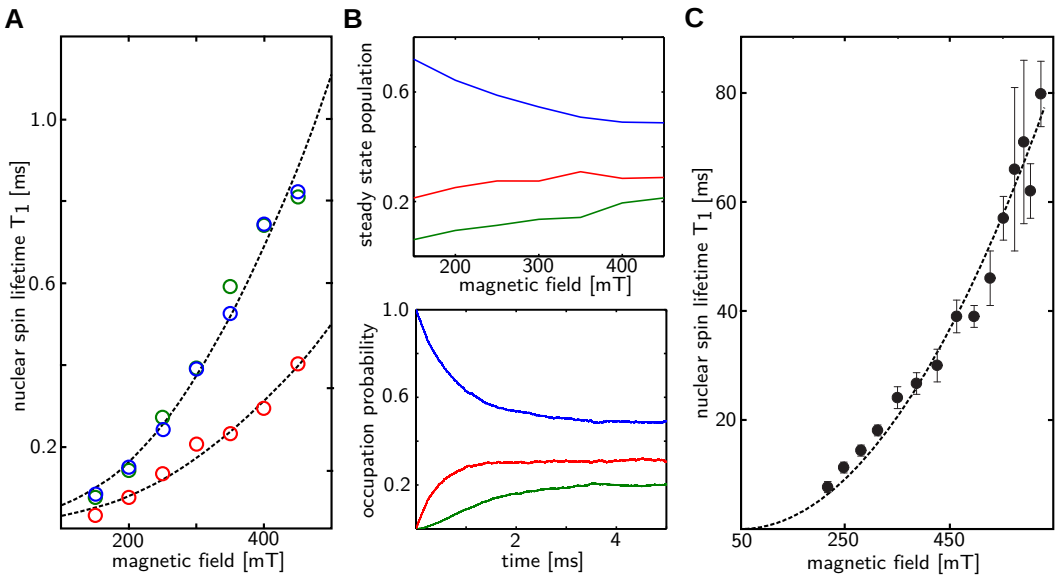

Figure 7.5.: **(A)** shows the simulated lifetime of the ^{14}N nuclear spin under laser illumination dependent of the magnetic field. The red circles represent the $m_I = 0$ state, green $m_I = -1$ and blue $m_I = +1$. **(B)** The above figure represents the steady state occupation probabilities of the ^{14}N nuclear spin under laser irradiation. The further the magnetic field detunes the system from the excited state LAC the closer the occupation probabilities of $m_I = \pm 1$ become. Below is an example of the relaxation dynamics of the ^{14}N nuclear spin under laser radiation at 450 mT. **(C)** shows the measured magnetic field dependence of the nuclear spin T_1 times with 200 ns laser and 2300 ns per repetition without . Both (A) and (C) show quadratic magnetic field dependence indicating the governing dynamics are captured by the simulation.

states $m_I = \{0, +1\}$. This is a mixture of the lifetimes with $T_{1\,\text{laser}}$ and without laser irradiation $T_{1\,\text{no laser}}$. They combine as

$$T_{1\,\text{avg}} = \frac{\Delta t_{\text{laser}} + \Delta t_{\text{no laser}}}{\frac{\Delta t_{\text{laser}}}{T_{1\,\text{laser}}} + \frac{\Delta t_{\text{no laser}}}{T_{1\,\text{no laser}}}} \tag{7.18}$$

to the effective lifetime. In order to retrieve $T_{1\,\text{laser}}$ and $T_{1\,\text{no laser}}$ from $T_{1\,\text{avg}}$ the lifetime was measured with increasing periods with the laser switched off while keeping the laser periods fixed to $\Delta t_{\text{laser}} = 200\,\text{ns}$. (7.18) is fitted to the data as shown in fig. 7.5. The fitted values are

	$m_I = -1$	$m_I = \{0, +1\}$
$T_{1\,\text{laser}}$	$2.8 \pm 0.2\,\text{ms}$	$5.6 \pm 0.4\,\text{ms}$
$T_{1\,\text{no laser}}$	$390 \pm 20\,\text{ms}$	$760 \pm 30\,\text{ms}$.

The measured lifetimes of the nuclear spin under laser radiation are of the same order as the calculated values. The deviation most likely originates from $A_\perp$ which was assumed too high.

As mentioned before the electron spin state can be correlated to the occupation probability of every one of the nitrogen nuclear spin states. So the "probed" lifetimes of all three nuclear spin levels could be measured

probed:	$\lvert -1_\text{n}\rangle$	$\lvert 0_\text{n}\rangle$	$\lvert +1_\text{n}\rangle$
T_1^{probed}	43 ms	18 ms	38 ms
T_1^{remain}	70 ms	22 ms	40 ms.

As the simulation indicated T_1^{probed} of the $m_I = 0$ state is shorter than the other two by roughly a factor of two. The other notable fact is that T_1 of $\lvert -1_\text{n}\rangle$ is a little longer than of $\lvert +1_\text{n}\rangle$. This may be due to a reduced flip-flop probability because by the CNOT gate the system is partially transfered into $\lvert -1_\text{e} - 1_\text{n}\rangle$. This state is not subject to mixing. Thus the flip-flop probability is reduced according to the occupation probability of $\lvert -1_\text{e} - 1_\text{n}\rangle$.

The measured magnetic field dependence of T_1 (fig. 7.5) exhibits a quadratic behavior. This finally leads to the conclusion that the mixing in the electronic excited state is the leading mechanism for the longitudinal relaxation of the nitrogen nuclear spin. By further increasing the magnetic field the T_1 time can in principle be increased up to $T_{1\,\text{no laser}} \approx 800\,\text{ms}$ where other relaxation mechanisms get relevant.

7.2. Conclusion

We have shown that an approximate quantum-non-demolition measurement comparable to trapped ions [68] is feasible with NV centers in diamond by correlating the ^{14}N's nuclear spin state of interest to the NV's electron spin, reading out the latter. Although the illumination with laser light imposes complicated dynamics on the spin system we found the relaxation of the nuclear governed by state mixing in the electronic excited state which diminishes with increasing magnetic field. That allows us to decouple the dynamics of nuclear and electron spin by increasing the magnetic field. The longer the nuclear spin is unaffected by relaxation the longer the signal can be integrated. Thus reducing the shot noise and therefore improving the read out fidelity.

In principle it is possible to extend the single shot readout to ^{13}C nuclear spins in the vicinity of the NV. Best suited are carbon spins located along the NV axis or on its equatorial plane. If the NV's coherence time is long enough to perform the CNOT gate weak coupling ^{13}C would be sufficient as well.

The realization of single shot read out has put the diamond among the leading systems of quantum information processing. With the achieved read out fidelity of $\sim 92\,\%$ we are close to the $95\,\%$ error per gate at least required to apply quantum error correction suitable for a scalable quantum computer [58] which should be reachable by further increasing the magnetic field. We are now able to test nonclassical correlations on a single qubit by testing the temporal Bell inequalities [60, 46, 47]. When able to perform the QND measurement on a larger register also the test of Bells inequalities and teleportation of quantum states becomes possible. Even in the field of metrology e.g. the sensing of magnetic fields the single shot readout could be a vast improvement because in contrast to conventional photon counting it is not limited by photon shot noise.

8. A Noise Spectral Density Approach to Dynamic Decoupling

In order to understand or even device sophisticated dynamic decoupling sequences like "Carr, Purcell, Meiboom, Gill" sequence (CPMG) [19] or "Uhrig dynamic decoupling" (UDD) [99] one has to understand how these algorithms decouple the target qubit from its environment. Therefore one needs to apply a more sophisticated model than the Bloch sphere picture, which depicts ambient noise varying on a time scale much slower than the measurement time τ. Here UDD and CPMG function the same way as the Hahn echo. Even if artificial damping is introduced to the Bloch equations (3.78)-(3.80) the effects of these sequences is not captured. The difference becomes obvious if we introduce noise fluctuating faster than $1/\tau$.

As described in more detail below the environment of every spin has its characteristic frequencies represented by its noise spectral density (NSD) $\Gamma(\omega)$. In the commonly used description a positive and a negative frequency branch is used to depict environment induced excitation (negative branch) and deexcitation (positive branch). In a thermal environment a Boltzmann factor connects the noise amplitude of two corresponding frequencies. This makes sure that the steady state of the system is the thermal state. In the low frequency range we are interested in, both branches are equal. Since the oscillation amplitude declines like δ^2 with the detuning δ of the two resonance frequencies flip-flop processes of the central spin are allowed primarily with bath entities of matching frequency. The relaxation time T_1 is therefore determined by the noise amplitude at the splitting of the observed transition.

Static, secular noise commutes with the time independent Hamiltonian of a static system at all times. It can not induce transitions, but it introduces phase shifts like fluctuating classical fields. The pure dephasing time $T_{2\rho}$ is therefore governed by the static noise at $\omega = 0$.

By applying microwave radiation we introduce a time dependence to the system Hamiltonian. One of the simplest cases is driving a continuous Rabi

oscillation of the spin (sec. 3.6). Now field noise at the Rabi frequency commutes with the system Hamiltonian. The system is effectively gapped by the Rabi frequency. Noise of the corresponding frequency now contributes to the damping of the Rabi oscillations with the time constant $T_{1\rho}$.

Measurements however have finite duration. This truncation introduces a time dependence to the system. Essentially the system becomes sensitive to the "harmonics" of the measurement time τ. This is represented in the frequency domain by a so called filter function $S(\tau, \omega)$ (fig. 8). It depicts continuously the sensitivity to frequencies around the frequency probed by an infinitely long measurement. In the case of dephasing experiments this would be $\omega = 0$. By increasing τ in the course of the measurement the "harmonics" change by moving closer to the center frequency. Therefore with a series of different τ different noise frequencies are probed. The application of quantum gates during the measurement time reshapes the filter function. For the sake of simplicity we restrict ourself to Hadamard and Pauli gates that are applied instantaneous in time. This so called δ-pulse regime is effectively reached in the experiment if the respective pulse duration is about three orders of magnitude shorter than τ [99]. If the gates are applied in a clever way the system becomes insensitive to the center frequency and thus to the foremost decay source. This is called dynamic decoupling. As discussed for the Hahn echo sequence in sec. 3.7.3 the application of a Pauli gate effectively inverts the phase dynamics. This leads to a refocusation of the phase coherence the spin echo. If one is only interested in the dynamics of the echo amplitude this refocussing dynamics is equivalent to the system not being sensitive to the noise which effect was refocused. This insensitivity is captured by $S(\tau, \omega)$.

Due to the high Debye temperature of diamond, phonons do not play a major role even at room temperature. Thus the noise floor is more or less constant in the applicable frequency range. T_1 is therefore insensitive to changes of the system splitting e.g. application of a low magnetic field. Because we are interested in prolonging the T_2 time we look at in the low frequency range of the NSD concentrating on magnetic nuclear spin noise. It originates on the one hand from mutual flip-flops among bath spins and on the other hand from single spin Larmor precession.

Measured Hahn echoes of NV centers show periodic collapses and revivals of the system coherence (fig. 8). This can be explained by coherent interaction with close by ^{13}C nuclei [21]. While the NV is in the $m_S = 0$ state the nuclear spins undergo Larmor precession with $\omega_{\mathrm{L}0} = \gamma B$. In the $m_S = \pm 1$ state their frequency changes to $\omega_{\mathrm{L}\pm1} = \gamma B + \hat{H}^{\mathrm{B}}_{\mathrm{I}i}$ with $\hat{H}^{\mathrm{B}}_{\mathrm{I}i}$ the A-term of the dipole-dipole interaction. In principle both oscillations are visible in the NV's coherence. Different interaction strengths with the NV average out. Thus rendering the

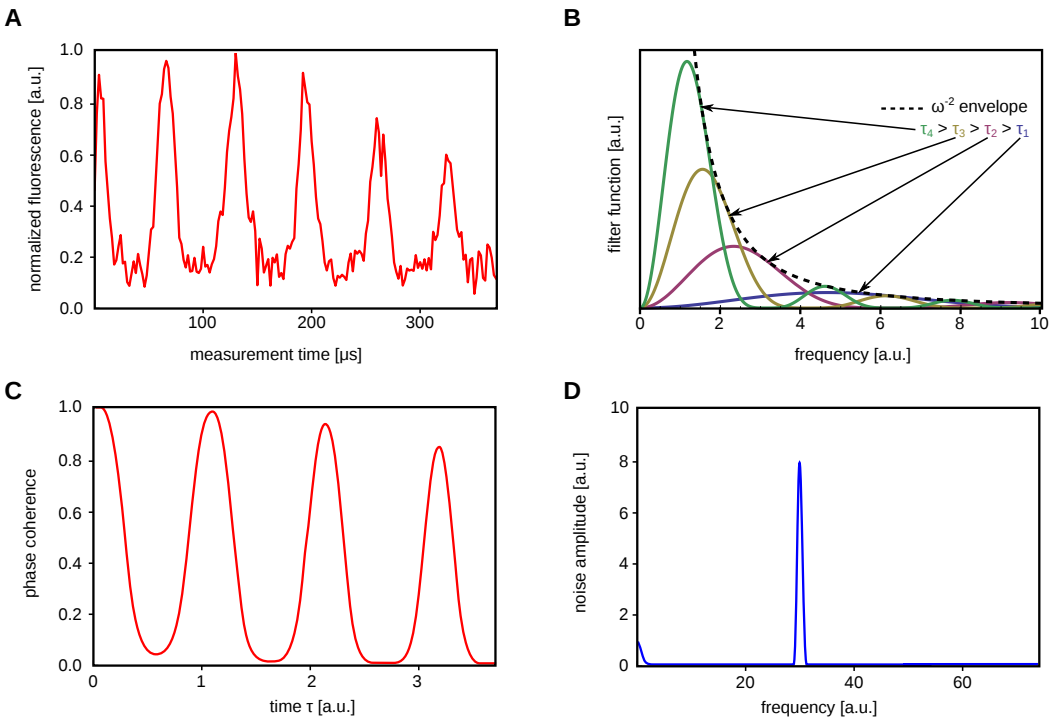

Figure 8.1.: **A** experimental Hahn echo data showing collapse and revivals caused by the Larmor precession of the ^{13}C. **B** The filter function $S(\tau, \omega)$ for a Hahn echo experiment. With increasing τ the "harmonics" of the sequence duration move towards the center frequency $\omega_0 = 0$. **C** Calculated Hahn echo signal by means of the filter function $S(\tau, \omega)$ and the noise spectral density. **D** Schematic of a NSD with a distinct feature.

process an incoherent relaxation to half the Rabi amplitude. The ω_{L0} however coincide for all ^{13}C. The coherence is therefore recovered at times $1/\omega_{\mathrm{L0}}$.

In the framework of the NSD and the filter function the collapses and revivals appear due to passing of the sensitivity peaks of $S(\tau, \omega)$ over a dominant feature in the NSD at ω_{L0}. While being sensitive to this strong noise source leads to a collapse of the coherence, it is preserved while insensitive to it. As depicted in fig. 8.2 we are able to qualitatively predict the measurement outcome of any given pulse scheme with this simple approach. We will now elaborate on a more detailed picture in order to do quantitative calculations.

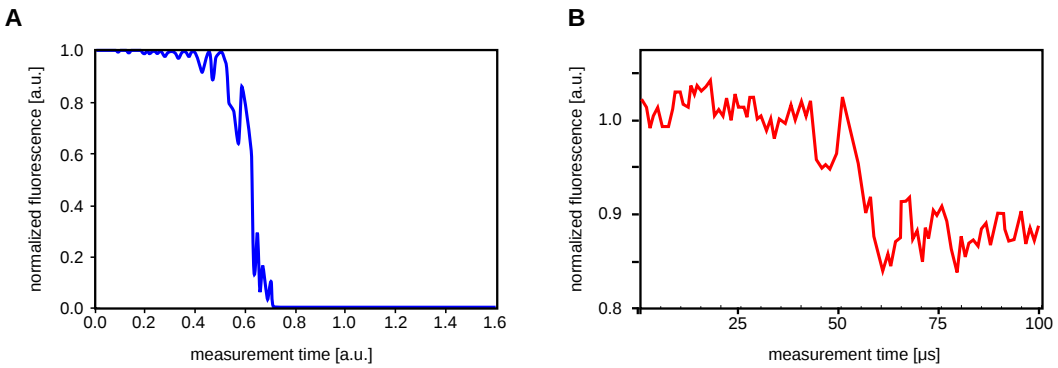

Figure 8.2.: Comparison between the calculated **A** and the measured **B** outcome of an UDD_{10} sequence. The calculation was done just assuming a single narrow noise feature at the ^{13}C Larmor frequency.

8.1. The Noise Spectral Density

The NSD description of dephasing is closely related to the application of a quantum master equation. It is introduced in the process of eliminating the bath degrees of freedom from the description of the system. Following [15] we derivate a Redfield master equation and introduce the NSD in the process. To describe the influence of a the quantum environment on a central spin system we start from the system Hamiltonian

$$\hat{H} = \hat{H}_\mathrm{S} + \hat{H}_\mathrm{B} + \hat{H}_\mathrm{I}. \tag{8.1}$$

$\hat{H}_\mathrm{S}$ denotes the free system Hamiltonian and $\hat{H}_\mathrm{B}$ the environment Hamiltonian respectively. $\hat{H}_\mathrm{I}$ represents the interactions between system and the environment. The dynamics in the interaction picture are given by (3.47)

$$\hat{\rho}_\mathrm{I}(t) = \hat{\rho}(t_0) - \frac{\mathrm{i}}{\hbar}\int_{t_0}^{t} [\hat{H}_\mathrm{I}(s), \hat{\rho}_\mathrm{I}(s)]\,\mathrm{d}s. \tag{8.2}$$

If we insert the differential form (3.46) and take the partial trace over the bath we obtain

$$\frac{\mathrm{d}\,\hat{\rho}_\mathrm{S}(t)}{\mathrm{d}t} = \mathrm{tr}_\mathrm{B}[\hat{H}_\mathrm{I}(t), \hat{\rho}_I(0)] - \int_{t_0}^{t} \mathrm{tr}_\mathrm{B}[\hat{H}_\mathrm{I}(t), [\hat{H}_\mathrm{I}(s), \hat{\rho}_\mathrm{I}(s)]]\,\mathrm{d}s. \tag{8.3}$$

We further assume that $\mathrm{tr}_\mathrm{B}[\hat{H}_\mathrm{I}(t), \hat{\rho}_I(0)] = 0$. In order to replace the full system density matrix $\hat{\rho}_\mathrm{I}(t)$ on the right hand side of the equation by the

system Hamiltonian $\hat{\rho}_{\mathrm{S}}(t)$ we perform the *Born approximation*. It assumes weak coupling between system and bath, such that the influence of the former on the latter is small. In other words the state of the system does not affect the state of the bath.

$$\hat{\rho}(t)_{\mathrm{I}} \approx \hat{\rho}_{\mathrm{S}}(t) \otimes \hat{\rho}_{\mathrm{B}}. \tag{8.4}$$

In the case of the NV center this does not hold true in a strict sense. The interaction energy between the NV and the nearest surrounding nuclei is big compared to their splitting. So the bath Hamiltonian $\hat{H}_{\mathrm{B}}$ changes dramatically depending on the state of the NV spin. But room temperature experiments justify taking the high temperature limit. So the thermal state of any given nuclear spin in the environment is $\hat{\rho}_{\mathrm{B_{nuc}}} = 1/2\,\mathbb{1}$ regardless of its splitting. That allows us to apply the approximation nonetheless. Inserting (8.4) into (8.3) we get a closed equation of motion for the system state alone

$$\frac{\mathrm{d}\,\hat{\rho}_{\mathrm{S}}(t)}{\mathrm{d}t} = -\int_{t_0}^{t} \mathrm{tr}_{\mathrm{B}}[\hat{H}_{\mathrm{I}}(t), [\hat{H}_{\mathrm{I}}(s), \hat{\rho}_{\mathrm{S}}(s) \otimes \hat{\rho}_{\mathrm{B}}]]\,\mathrm{d}s. \tag{8.5}$$

It is still impossible to solve this equation for most cases.

One way to introduce further simplification is to apply the *Markov approximation*. Here we assume that the system state is independent of its history. Thus defining the integration kernel of (8.5) local in time. So we substitute $\hat{\rho}_{\mathrm{S}}(s)$ with $\hat{\rho}_{\mathrm{S}}(t)$ and arrive at the *Redfield equation* [82]

$$\frac{\mathrm{d}\,\hat{\rho}_{\mathrm{S}}(t)}{\mathrm{d}t} = -\int_{t_0}^{t} \mathrm{tr}_{\mathrm{B}}[\hat{H}_{\mathrm{I}}(t), [\hat{H}_{\mathrm{I}}(s), \hat{\rho}_{\mathrm{S}}(t) \otimes \hat{\rho}_{\mathrm{B}}]]\,\mathrm{d}s. \tag{8.6}$$

To finally arrive at a true *Markovian master equation* one needs to transform (8.6) to have dynamic semigroup properties [85]

$$\frac{\mathrm{d}\,\hat{\rho}_{\mathrm{S}}(t)}{\mathrm{d}t} = -\int_{t_0}^{t} \mathrm{tr}_{\mathrm{B}}[\hat{H}_{\mathrm{I}}(t), [\hat{H}_{\mathrm{I}}(t-s), \hat{\rho}_{\mathrm{S}}(t) \otimes \hat{\rho}_{\mathrm{B}}]]\,\mathrm{d}s. \tag{8.7}$$

The time locality constraint infers that there is no coherence "returning" from the environment to the NV. Thus the phase coherence should in principle never rise above its previous value. Coherence may flow back to the central spin system on a time scale of the the baths correlation time τ_{B}. So the master equation only captures dynamics on a time scale longer than that.

To further simplify the master equation we apply the *secular* or *rotating wave approximation* by averaging over the rapidly oscillating terms in the master equation. For this purpose we take a closer look at the interaction Hamiltonian $\hat{H}_\mathrm{I}$. Its most general form is

$$\hat{H}_\mathrm{I} = \sum_k \hat{H}^\mathrm{S}_{\mathrm{I}k} \otimes \hat{H}^\mathrm{B}_{\mathrm{I}k} \tag{8.8}$$

where all $\hat{H}^\mathrm{S}_{\mathrm{I}k}$ and $\hat{H}^\mathrm{B}_{\mathrm{I}k}$ are self-adjoint operators. First we decompose the system sided operators $\hat{H}^\mathrm{S}_{\mathrm{I}k}$ into eigenoperators of the system Hamiltonian $\hat{H}_\mathrm{S}$. Let the eigenvalues of $\hat{H}_\mathrm{S}$ be ε and the according projection operators $\hat{\Pi}(\varepsilon)$. After the transformation

$$\hat{H}^\mathrm{S}_{\mathrm{I}k}(\omega) = \sum_{\varepsilon'-\varepsilon=\omega} \hat{\Pi}(\varepsilon)\, \hat{H}^\mathrm{S}_{\mathrm{I}k}\, \hat{\Pi}(\varepsilon) \tag{8.9}$$

the $\hat{H}^\mathrm{S}_{\mathrm{I}k}(\omega)$ are eigenoperators of $\hat{H}_\mathrm{S}$ which means

$$[\hat{H}_\mathrm{S}, \hat{H}^\mathrm{S}_{\mathrm{I}k}(\omega)] = -\omega\, \hat{H}^\mathrm{S}_{\mathrm{I}k}(\omega) \tag{8.10}$$

$$[\hat{H}_\mathrm{S}, \hat{H}^{\mathrm{S}\,\dagger}_{\mathrm{I}k}(\omega)] = +\omega\, \hat{H}^{\mathrm{S}\,\dagger}_{\mathrm{I}k}(\omega) \tag{8.11}$$

$$[\hat{H}_\mathrm{S}, \hat{H}^{\mathrm{S}\,\dagger}_{\mathrm{I}k}(\omega)\, \hat{H}^\mathrm{S}_{\mathrm{I}k}(\omega)] = 0 \tag{8.12}$$

$$\hat{H}^\mathrm{S}_{\mathrm{I}k}(-\omega) = \hat{H}^{\mathrm{S}\,\dagger}_{\mathrm{I}k}(\omega). \tag{8.13}$$

Applying the completeness relation we get

$$\sum_\omega \hat{H}^\mathrm{S}_{\mathrm{I}k}(\omega) = \sum_\omega \hat{H}^{\mathrm{S}\,\dagger}_{\mathrm{I}k}(\omega) = A_k. \tag{8.14}$$

Inserted into (8.8) the interaction Hamiltonian takes form

$$\hat{H}_\mathrm{I} = \sum_{k,\omega} \hat{H}^\mathrm{S}_{\mathrm{I}k}(\omega) \otimes \hat{H}^\mathrm{B}_{\mathrm{I}k} = \sum_{k,\omega} \hat{H}^{\mathrm{S}\,\dagger(\omega)}_{\mathrm{I}k} \otimes \hat{H}^{\mathrm{B}\,\dagger}_{\mathrm{I}k}. \tag{8.15}$$

After this decomposition $\hat{H}_\mathrm{I}$ is transformed into the interaction picture

$$\hat{H}_\mathrm{I}(t) = \sum_{k,\omega} \mathrm{e}^{-\mathrm{i}\,\omega\, t}\, \hat{H}^\mathrm{S}_{\mathrm{I}k}(\omega) \otimes \hat{H}^\mathrm{B}_{\mathrm{I}k}(t) = \sum_{k,\omega} \mathrm{e}^{\mathrm{i}\,\omega\, t} \hat{H}^{\mathrm{S}\,\dagger}_{\mathrm{I}k}(\omega) \otimes \hat{H}^{\mathrm{B}\,\dagger}_{\mathrm{I}k}(t). \tag{8.16}$$

Inserting this in (8.7) leads after some calculation to

$$\begin{aligned}\frac{\mathrm{d}\,\hat{\rho}_\mathrm{S}(t)}{\mathrm{d}t} =& \sum_{\omega,\omega'} \sum_{k,l} \mathrm{e}^{\mathrm{i}\,(\omega'-\omega)\,t}\, \hat{\Gamma}_{kl}(\omega) \cdot \\ & \cdot \Big(\hat{A}_l(\omega)\, \hat{\rho}_\mathrm{S}(t)\, \hat{H}^{\mathrm{S}\,\dagger}_{\mathrm{I}k}(\omega') - \hat{H}^{\mathrm{S}\,\dagger}_{\mathrm{I}k}(\omega')\, \hat{A}_l(\omega)\, \hat{\rho}_\mathrm{S}(t) \Big) + \mathrm{h.c.}\end{aligned} \tag{8.17}$$

Here $\hat{\Gamma}_{kl}(\omega)$ is the one-sided Fourier transform

$$\hat{\Gamma}_{kl}(\omega) = \int_0^\infty \mathrm{e}^{\mathrm{i}\,\omega\,s}\,\langle \hat{H}^{\mathrm{B}\,\dagger}_{\mathrm{I}\,k}(t)\,\hat{H}^{\mathrm{B}}_{\mathrm{I}\,l(t-s)}\rangle\,\mathrm{d}s \tag{8.18}$$

of the bath correlation function

$$G(t) = \langle \hat{H}^{\mathrm{B}\,\dagger}_{\mathrm{I}\,k}(t)\,\hat{H}^{\mathrm{B}}_{\mathrm{I}\,l(t-s)}\rangle = \mathrm{tr}_{\mathrm{B}}\{\hat{H}^{\mathrm{B}\,\dagger}_{\mathrm{I}\,k}(t)\,\hat{H}^{\mathrm{B}}_{\mathrm{I}\,l(t-s)}\,\hat{\rho}_B\}. \tag{8.19}$$

If $\hat{\rho}_B$ is in a stationary state of the environment, which is true for a thermal bath, the bath correlation function is homogeneous in time. So we can write

$$\langle \hat{H}^{\mathrm{B}\,\dagger}_{\mathrm{I}\,k}(t)\,\hat{H}^{\mathrm{B}}_{\mathrm{I}\,l(t-s)}\rangle = \langle \hat{H}^{\mathrm{B}\,\dagger}_{\mathrm{I}\,k}(s)\,\hat{H}^{\mathrm{B}}_{\mathrm{I}\,l(0)}\rangle. \tag{8.20}$$

Now we are able to complete the *secular approximation* by discarding fast oscillating terms in (8.17) leaving us with

$$\begin{aligned}\frac{\mathrm{d}\,\hat{\rho}_{\mathrm{S}}(t)}{\mathrm{d}t} =& \sum_{\omega}\sum_{k,l}\hat{\Gamma}_{kl}(\omega)\left(\hat{A}_l(\omega)\,\hat{\rho}_{\mathrm{S}}(t)\,\hat{H}^{\mathrm{S}\,\dagger}_{\mathrm{I}\,k}(\omega) - \hat{H}^{\mathrm{S}\,\dagger}_{\mathrm{I}\,k}(\omega)\,\hat{A}_l(\omega)\,\hat{\rho}_{\mathrm{S}}(t)\right) + \\ &+ \mathrm{h.c.}.\end{aligned} \tag{8.21}$$

This equation can be brought to Lindblad form [15].

In the context of the noise environment $\hat{\Gamma}_{kl}(\omega)$ is of great interest. In order to investigate it further we split it in

$$\hat{\Gamma}_{kl}(\omega) = \frac{1}{2}\,\hat{\gamma}_{kl}(\omega) + \mathrm{i}\,\hat{S}_{kl}(\omega). \tag{8.22}$$

The two parts are

$$\hat{\gamma}_{kl}(\omega) = \hat{\Gamma}_{kl}(\omega) + \hat{\Gamma}^*_{kl}(\omega) \tag{8.23}$$

$$\hat{S}_{kl}(\omega) = \frac{1}{2\,\mathrm{i}}\,(\hat{\Gamma}_{kl}(\omega) - \hat{\Gamma}^*_{kl}(\omega)). \tag{8.24}$$

$\hat{S}_{kl}(\omega)$ commutes with the system Hamiltonian $\hat{H}_{\mathrm{S}}$. Therefore it is responsible for Lamb shift like renormalization of the systems energy levels

$$\hat{H}_{\mathrm{LS}} = \sum_{\omega}\sum_{k,l}\hat{S}_{kl}(\omega)\,\hat{H}^{\mathrm{S}\,\dagger}_{\mathrm{I}\,k}(\omega)\,\hat{A}_l(\omega). \tag{8.25}$$

Reinserted in (8.21) $\hat{\gamma}_{kl}(\omega)$ constitutes the dissipator

$$\mathcal{D}(\hat{\rho}_{\mathrm{S}}) = \sum_{\omega}\sum_{k,l}\hat{\gamma}_{kl}(\omega)\left(\hat{A}_l(\omega)\,\hat{\rho}_{\mathrm{S}}(t)\,\hat{H}^{\mathrm{S}\,\dagger}_{\mathrm{I}\,k}(\omega) - \frac{1}{2}\,\left[\hat{H}^{\mathrm{S}\,\dagger}_{\mathrm{I}\,k}(\omega)\,\hat{A}_l(\omega)\,\hat{\rho}_{\mathrm{S}}(t)\right]\right).$$

(8.26)

$\hat{\gamma}_{kl}(\omega)$ is called noise spectral density. It is the real part of the Fourier transform of the bath correlation function (8.18). In a classical picture it depicts the amplitude of a fluctuating field at any given frequency. The frequencies are selected by the system Hamiltonian $\hat{H}_{\mathrm{S}}$ in the interaction picture. For pure dephasing static noise ($\hat{\gamma}_{kl}(0)$) in combination with the frequencies introduced by the filter function of the respective quantum algorithm are relevant.

8.2. Calculation of the NSD

We can distinguish between two types of magnetic field noise originating from the ^{13}C nuclei. On the one hand there are mutual flip flops between the nuclei. They interact via dipole-dipole interaction which is of the order of few kHz and less. On the other hand every nuclear spin undergoes Larmor precession in the combined external and NV magnetic field. Both dynamics lead to a fluctuating magnetic field at the site of the NV. As can be seen from (8.26) $\hat{\gamma}_{kl}(\omega)$ acts on one single transition kl. If the $m_S = 0$ state is part of the observed superposition state there is no dipolar interaction between the NV spin and the ^{13}C nuclei. Thus the Larmor frequency of all ^{13}C spins is their Zeeman splitting. Even at low magnetic fields this leads to a predominant peak at the free Larmor frequency in the NSD. In all other cases the Larmor frequencies are wide spread due to the dipole-dipole coupling to the NV. A "Larmor peak" emerges when the magnetic field strength is of the order of the hyperfine interaction (fig. 8.3).

8.2.1. Discrete Noise Features

Following [92] the flip-flop part of the noise spectral density is calculated as follows. We rewrite the Hamiltonian (8.1) as

$$\hat{H} = \hat{H}_{\mathrm{S}} + \underbrace{\hat{H}_{\mathrm{Z}}^{\mathrm{n}} + \hat{H}_{\mathrm{int}}^{\mathrm{n}}}_{\hat{H}_{\mathrm{B}}} + \hat{H}_{\mathrm{int}}. \tag{8.27}$$

$\hat{H}_{\mathrm{S}}$ is the NV Hamiltonian (2.2) while

$$\hat{H}_{\mathrm{Z}}^{\mathrm{n}} = -\gamma_{\mathrm{n}} \underline{B} \sum_i \underline{\hat{I}}_i \tag{8.28}$$

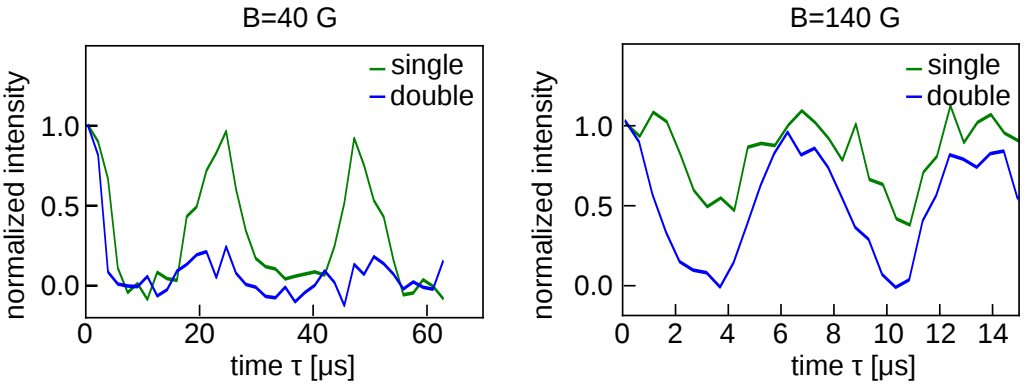

Figure 8.3.: the measurement data compares Hahn echo data of the "single" $m_S = 0 \leftrightarrow m_S = -1$ transition and the "double" $m_S = -1 \leftrightarrow m_S = +1$ transition. It confirms that with increasing magnetic field the Larmor noise leads to collapses and revivals even if the $m_S = 0$ level is not involved in the observed coherence.

is the nuclear Zeeman splitting and

$$\hat{H}_{\text{int}}^{\text{n}} = \gamma_{\text{n}}^2 \hbar \sum_{i<j} \frac{\hat{\underline{I}}_i \hat{\underline{I}}_j - 3\,(\hat{\underline{I}}_i\,\underline{r}_{ij})\,(\hat{\underline{I}}_j\,\underline{r}_{ij})}{r_{ij}^3} \tag{8.29}$$

$$\hat{H}_{\text{int}} = \gamma_{\text{e}}\,\gamma_{\text{n}}\,\hbar \sum_{i} \frac{\hat{\underline{S}}\,\hat{\underline{I}}_j - 3\,(\hat{\underline{S}}\,\underline{r}_i)\,(\hat{\underline{I}}_i\,\underline{r}_i)}{r_{ij}^3}. \tag{8.30}$$

are the dipole-dipole interaction Hamiltonians among the ^{13}C and between the NV and the nuclei. $\underline{r}_{ij}$ ($\underline{r}_i$) is the normalized vector between two given ^{13}C nuclei (the NV site and a ^{13}C nucleus). A short look at $\hat{H}_{\text{Z}}^{\text{n}}$ and $\hat{H}_{\text{int}}^{\text{n}}$ shows that the transformation into the interaction picture will give rise to a very complicated time dependence of the interaction Hamiltonian $\hat{H}_{\text{I int}}$. For simplicity we assume that the magnetic field is oriented parallel to the NV axis in z-direction. As a further simplification we omit terms in (8.29) that do not conserve the nuclear Zeeman energy and rewrite

$$\hat{H}_{\text{int}}^{\text{n}} \approx \frac{1}{4}\,\gamma_{\text{n}}^2\,\hbar \sum_{i<j} \frac{1 - 3\,\cos^2\theta_{ij}}{r_{ij}^3}\,(\hat{I}_{+\,i}\,\hat{I}_{-\,j} + \hat{I}_{-\,i}\,\hat{I}_{+\,j} - 4\,\hat{I}_{\text{z}\,i}\,\hat{I}_{\text{z}\,j}). \tag{8.31}$$

θ_{ij} is the angle between $\underline{r}_{ij}$ and the z-direction. With (8.4) the dynamics of the ^{13}C nuclear spins are governed by the effective Hamiltonian

$$H_{\mathrm{n}}^{\mathrm{eff}} = \sum_{i<j} \gamma_{\mathrm{n}} \underline{B} \, (\hat{I}_{\mathrm{z}\,i} + \hat{I}_{\mathrm{z}\,j}) + \frac{1}{2} \, (\hat{H}_{\mathrm{I}\,i}^{\mathrm{B}} \, \hat{I}_{\mathrm{z}\,i} + \hat{H}_{\mathrm{I}\,j}^{\mathrm{B}} \, \hat{I}_{\mathrm{z}\,j}) + \frac{1}{4} \, \gamma_{\mathrm{n}}^2 \, \hbar \, \frac{1 - 3 \, \cos^2 \theta_{ij}}{r_{ij}^3} \, (\hat{I}_{+\,i} \, \hat{I}_{-\,j} + \hat{I}_{-\,i} \, \hat{I}_{+\,j} - 4 \, \hat{I}_{\mathrm{z}\,i} \, \hat{I}_{\mathrm{z}\,j}). \tag{8.32}$$

Due to the zero field splitting of the NV flip-flop processes with a nuclear spin are energy forbidden. Therefore we can separate the dynamics and restrict ourself to the subspace of the single electronic spin states ($m_S = 0, \ \pm 1$). The resulting NSD is the same for $m_S = \pm 1$ as is easily confirmed by substituting $\hat{H}_{\mathrm{I}\,i}^{\mathrm{B}} = -\hat{H}_{\mathrm{I}\,i}^{\mathrm{B}}$ for all i. For $m_S = 0$ the situation is significantly different because $\hat{H}_{\mathrm{I}\,i}^{\mathrm{B}} = 0$ in first order which is of great importance for the single spin part of the noise. Now we can proceed to the *interaction picture* time correlation function.

$$\begin{aligned} G(t) &= \left\langle \sum_i \hat{H}_{\mathrm{I}\,i}^{\mathrm{B}} \, \hat{I}_{\mathrm{z}\,i}(t) \, \sum_j \hat{H}_{\mathrm{I}\,j}^{\mathrm{B}} \, \hat{I}_{\mathrm{z}\,j}(0) \right\rangle \\ &= \sum_i {\hat{H}_{\mathrm{I}\,i}^{\mathrm{B}}}^2 \, \langle \hat{I}_{\mathrm{z}\,i}(t) \, \hat{I}_{\mathrm{z}\,i}(0) \rangle + \sum_{i,j \neq i} \hat{H}_{\mathrm{I}\,i}^{\mathrm{B}} \hat{H}_{\mathrm{I}\,j}^{\mathrm{B}} \, \langle \hat{I}_{\mathrm{z}\,i}(t) \, \hat{I}_{\mathrm{z}\,j}(0) \rangle \end{aligned} \tag{8.33}$$

To further investigate we do a *pair approximation* by discarding all higher order correlations.

$$\langle \hat{I}_{\mathrm{z}\,i}(t) \, \hat{I}_{\mathrm{z}\,i}(0) \rangle \approx \sum_{j \neq i} \langle \hat{I}_{\mathrm{z}\,i}(t) \, \hat{I}_{\mathrm{z}\,i}(0) \rangle_{ij} \tag{8.34}$$

$$\langle \hat{I}_{\mathrm{z}\,i}(t) \, \hat{I}_{\mathrm{z}\,j}(0) \rangle \approx \langle \hat{I}_{\mathrm{z}\,i}(t) \, \hat{I}_{\mathrm{z}\,j}(0) \rangle_{ij} \tag{8.35}$$

where $\langle \rangle_{ij}$ denotes the thermal average restricted to the Hilbert space of the pair ij. This approximation is valid in sparsely populated environments like ^{13}C in diamond. The weak intra bath interactions reduce the third order interaction to a timescale not relevant for our purposes. However in dense spin environments as encountered e.g. in quantum dots model calculations of exact diagonalization of small spin ensembles show that higher order correlations are important. Entering this approximation into (8.33) and some algebra we get

$$G(t) \approx \sum_{i<j} \left\langle \left(\hat{H}_{\mathrm{I}\,i}^{\mathrm{B}} \, \hat{I}_{\mathrm{z}\,i}(t) + \hat{H}_{\mathrm{I}\,j}^{\mathrm{B}} \, \hat{I}_{\mathrm{z}\,j}(t) \right) \left(\hat{H}_{\mathrm{I}\,i}^{\mathrm{B}} \, \hat{I}_{\mathrm{z}\,i}(0) + \hat{H}_{\mathrm{I}\,j}^{\mathrm{B}} \, \hat{I}_{\mathrm{z}\,j}(0) \right) \right\rangle_{ij} \tag{8.36}$$

Doing the Fourier transform and expansion of $G(t)$ into eigenstates of (8.32) gives the NSD

$$\Gamma_{ij}(\omega) = \sum_{\alpha,\beta} p_\alpha |\langle\alpha| \hat{H}^{\mathrm{B}}_{\mathrm{I}i} \hat{I}_{\mathrm{z}\,i}(t) + \hat{H}^{\mathrm{B}}_{\mathrm{I}j} \hat{I}_{\mathrm{z}\,j}(t) |\beta\rangle|^2 \, \delta(\omega - E_{\beta\alpha}) \tag{8.37}$$

with $E_{\beta\alpha} = E_\beta - E_\alpha$ the transition energy between two energy eigenstates $|\alpha\rangle$, $|\beta\rangle$ with the occupation probability p_α. The NSD is essentially a sum over all transition frequencies introduced by $\hat{H}^{\mathrm{B}}_{\mathrm{I}i} \hat{I}_{\mathrm{z}\,i}(t) + \hat{H}^{\mathrm{B}}_{\mathrm{I}j} \hat{I}_{\mathrm{z}\,j}(t)$. For $I = 1/2$ nuclear spins like the ^{13}C the ij pair Hamiltonian (8.32) has the eigenenergies

$$E_{\uparrow\uparrow} = \gamma_n B - b_{ij} + a_{ij} \tag{8.38}$$

$$E_+ = b_{ij} + \sqrt{b_{ij}^2 + \Delta_{ij}^2} \tag{8.39}$$

$$E_- = b_{ij} - \sqrt{b_{ij}^2 + \Delta_{ij}^2} \tag{8.40}$$

$$E_{\downarrow\downarrow} = -\gamma_n B - b_{ij} - a_{ij} \tag{8.41}$$

with

$$b_{ij} = \frac{1}{4} \gamma_{\mathrm{n}}^2 \hbar \frac{1 - 3\,\cos^2\theta_{ij}}{r_{ij}^3} \tag{8.42}$$

the dipole-dipole interaction strength between the nuclei ij and

$$a_{ij} = \frac{1}{4} (\hat{H}^{\mathrm{B}}_{\mathrm{I}i} + \hat{H}^{\mathrm{B}}_{\mathrm{I}j}) \tag{8.43}$$

$$\Delta_{ij} = \frac{1}{4} (\hat{H}^{\mathrm{B}}_{\mathrm{I}i} - \hat{H}^{\mathrm{B}}_{\mathrm{I}j}) \tag{8.44}$$

defining the dipole-dipole interaction strength towards the NV. The transition frequency of the flip-flop process is the difference between E_+ and E_-

$$E_{+-} = 2\sqrt{b_{ij}^2 + \Delta_{ij}^2}. \tag{8.45}$$

It has the transition matrix element

$$\langle -| \hat{H}^{\mathrm{B}}_{\mathrm{I}i} \hat{I}_{\mathrm{z}\,i}(t) + \hat{H}^{\mathrm{B}}_{\mathrm{I}j} \hat{I}_{\mathrm{z}\,j}(t) |+\rangle = -2\Delta_{ij} \sin\theta \tag{8.46}$$

Inserting into (8.37) leads to the noise spectrum

$$\Gamma_{ij}(\omega) = A_{ij}^{\mathrm{rms}\,2} \, \delta(\omega) + 4 \frac{b_{ij}^2 \, \Delta_{ij}^2}{b_{ij}^2 + \Delta_{ij}^2} \, [p_+ \, \delta(\omega + E_{+-}) + p_- \, \delta(\omega - E_{+-})] \tag{8.47}$$

with the static part

$$A_{ij}^{\mathrm{rms}\,2} = 4\left[(p_{\uparrow\uparrow}+p_{\downarrow\downarrow})\,a_{ij}^2+(p_+ + p_-)\,\frac{\Delta_{ij}^4}{b_{ij}^2+\Delta_{ij}^2}\right] - 4\left[(p_{\uparrow\uparrow}-p_{\downarrow\downarrow})\,a_{ij}+(p_+ - p_-)\,\frac{\Delta_{ij}^2}{b_{ij}^2+\Delta_{ij}^2}\right]^2. \tag{8.48}$$

We now apply this known method to derive the "flip-flop" part to derive the "Larmor" part of the NSD by restricting ourselves to the single nucleus subspace. In terms of Larmor precession the interaction to neighboring nuclei only leads to line broadening which is taken into account later on. The bath Hamiltonian is reduced to its Zeeman part (8.28)

$$\hat{H} = \hat{H}_{\mathrm{S}} + \underbrace{\hat{H}_{\mathrm{n\,Z}}}_{\hat{H}_{\mathrm{B}}} + \hat{H}_{\mathrm{int}}. \tag{8.49}$$

In this rather simple case the *interaction picture* time correlation function (8.19) is analytically solvable for arbitrary magnetic field directions. First we expand $\hat{H}_{\mathrm{I\,int}}$ into eigenoperators of $\hat{H}_{\mathrm{S}}$ and truncate terms that do not couple to the S_z operator of the NV

$$\hat{H}_{\mathrm{I\,int}} \approx \sum_i \sum_{j=\{\mathrm{x,\,y,\,z}\}} c_{ij}\,S_z \otimes I_j. \tag{8.50}$$

The c_{ij} are

$$c_{i\mathrm{x}} = \frac{3}{4}\,\frac{\gamma_{\mathrm{e}}\,\gamma_{\mathrm{n}}\,\hbar^2}{r_i^3}\,\cos(\phi_i)\,\sin(2\,\theta_i) \tag{8.51}$$

$$c_{i\mathrm{y}} = \frac{3}{2}\,\frac{\gamma_{\mathrm{e}}\,\gamma_{\mathrm{n}}\,\hbar^2}{r_i^3}\,\cos(\theta_i)\,\sin(\theta_i)\,\cos(\phi_i) \tag{8.52}$$

$$c_{i\mathrm{z}} = \frac{1}{4}\,\frac{\gamma_{\mathrm{e}}\,\gamma_{\mathrm{n}}\,\hbar^2}{r_i^3}\,(1+3\,\cos(2\,\theta_i)) \tag{8.53}$$

with r_i, ϕ_i and θ_i the spheric coordinates of $^{13}C_i$ while the NV is in the center. The time correlation function (8.19) is

$$\begin{aligned} G_i(t) =& G_{i\mathrm{x}}(t) + G_{i\mathrm{y}}(t) + G_{i\mathrm{z}}(t) \\ =& \frac{1}{4}\,c_{i\mathrm{x}}^2\,[B_{\mathrm{x}}^2 + (B_{\mathrm{y}}^2+B_{\mathrm{z}}^2)\,\cos\{(\gamma_n\,\hbar\,\sqrt{B_{\mathrm{x}}^2+B_{\mathrm{y}}^2+B_{\mathrm{z}}^2}+B_i)\,t\}+ \\ &+\frac{1}{4}\,c_{i\mathrm{y}}^2\,[B_{\mathrm{y}}^2 + (B_{\mathrm{x}}^2+B_{\mathrm{z}}^2)\,\cos\{(\gamma_n\,\hbar\,\sqrt{B_{\mathrm{x}}^2+B_{\mathrm{y}}^2+B_{\mathrm{z}}^2}+B_i)\,t\}+ \\ &+\frac{1}{4}\,c_{i\mathrm{z}}^2\,[B_{\mathrm{z}}^2 + (B_{\mathrm{x}}^2+B_{\mathrm{y}}^2)\,\cos\{(\gamma_n\,\hbar\,\sqrt{B_{\mathrm{x}}^2+B_{\mathrm{y}}^2+B_{\mathrm{z}}^2}+B_i)\,t\}. \end{aligned} \tag{8.54}$$

The NSD follows

$$\Gamma_i(\omega) = \sqrt{\frac{\pi}{2}} \frac{1}{4\left(B_{\mathrm{x}}^2 + B_{\mathrm{y}}^2 + B_{\mathrm{z}}^2\right)} 2\left(B_{\mathrm{x}}^2\, c_{i\mathrm{x}}^2 + B_{\mathrm{y}}^2\, c_{i\mathrm{y}}^2 + B_{\mathrm{z}}^2 c_{i\mathrm{z}}^2\right) \delta(\omega) + \\ + \left(B_{\mathrm{x}}^2 \left(c_{i\mathrm{y}}^2 + c_{i\mathrm{z}}^2\right) + B_{\mathrm{y}}^2 \left(c_{i\mathrm{x}}^2 + c_{i\mathrm{z}}^2\right) + B_{\mathrm{z}}^2 \left(c_{i\mathrm{x}}^2 + c_{i\mathrm{y}}^2\right)\right) \cdot \\ \cdot\, \delta\left(\omega \pm \left(\gamma_n \hbar \sqrt{B_{\mathrm{x}}^2 + B_{\mathrm{y}}^2 + B_{\mathrm{z}}^2} + B_i\right)\right). \tag{8.55}$$

Again there is a static component which is immanent in (8.48) and thus ignored here. If the magnetic field is aligned to the NV axis $\Gamma(\omega)$ is reduced to

$$\Gamma_i(\omega) = \sqrt{\frac{\pi}{2}} \frac{1}{4} \left(c_{i\mathrm{x}}^2 + c_{i\mathrm{y}}^2\right) \delta\left(\omega \pm \left(\gamma_n \hbar B + B_i\right)\right). \tag{8.56}$$

Due to the angular dependence of c_x and c_y only spins located around the "magic angle" $\theta_{\mathrm{NV}} = 54.7°$ contribute to the Larmor noise. Especially at lower ^{13}C concentrations, this makes the peak less pronounced and may even vanish if there are on nuclear spins are located along the magic angle cone. This is in agreement with ESEEM. Here the modulation amplitude depends on the tilt of the nuclear spin quantization axis when the electron spin is flipped [86]. The quantization axis does not change if the ^{13}C nucleus is located along the NV quantization axis or on its equatorial plane. Because this Larmor kind of noise does not depend on the initial polarization of the ^{13}C nuclei the noise amplitude of the Larmor peak scales linearly with the ^{13}C concentration.

8.2.2. Introduction of Broadening to the NSD

Up to now the NSD consists of several δ-shaped lines due to mutual flip-flops and Larmor precession of the nuclei. We can further increase the number of lines e.g. by lifting the *pair approximation* (8.35). Increasing the size of clusters will give rise to some new transition frequencies but on top of that the multi spin interactions will introduce lifetime broadening to the existing lines. This broadening is estimated by a mean field theory closely following the method of moments introduced in chapter 5.0.1. We use the Van Vleck formula for the second moment to estimate the "line width" $\Delta\omega$ of the single spin feature of the NSD

$$M_2 = \sigma_i^2 = \frac{3}{4} \gamma_n^4 \hbar^2 I\left(I+1\right) \sum_i \frac{\left(1 - 3\,\cos^2\theta_i\right)^2}{r_i^6} \tag{8.57}$$

with σ the line width. For the flip-flop part we have to slightly modify the procedure. in the high temperature limit this part of the NSD for N-coupled

nuclei is

$$\Gamma_{ij}(\omega) = \sum_{\alpha,\beta} \frac{1}{N} |\langle\alpha| \hat{H}^{\mathrm{B}}_{\mathrm{I}i} \hat{I}_{\mathrm{z}\,i}(t) + \hat{H}^{\mathrm{B}}_{\mathrm{I}j} \hat{I}_{\mathrm{z}\,j}(t) |\beta\rangle|^2 \delta(\omega - E_{\beta\alpha}). \tag{8.58}$$

We directly calculate the 2nd moment

$$\begin{aligned}\int_{-\infty}^{\infty} \Gamma_{ij}(\omega)\,\mathrm{d}\omega &= -\frac{1}{2^N} \sum_{\alpha,\beta} \langle\alpha| \hat{H}^{\mathrm{B}}_{\mathrm{I}i} \hat{I}_{\mathrm{z}\,i}(t) + \hat{H}^{\mathrm{B}}_{\mathrm{I}j} \hat{I}_{\mathrm{z}\,j}(t) |\beta\rangle \langle\beta| \hat{H}^{\mathrm{B}}_{\mathrm{I}i} \hat{I}_{\mathrm{z}\,i}(t) + \hat{H}^{\mathrm{B}}_{\mathrm{I}j} \hat{I}_{\mathrm{z}\,j}(t) |\alpha\rangle \\ &= \frac{1}{2}\ {\hat{H}^{\mathrm{B}}_{\mathrm{I}i}}^2 \sum_{k\neq i} b_{ik}^2 - b_{ij}^2\, \hat{H}^{\mathrm{B}}_{\mathrm{I}i}\, \hat{H}^{\mathrm{B}}_{\mathrm{I}j} + \frac{1}{2}\ {\hat{H}^{\mathrm{B}}_{\mathrm{I}j}}^2 \sum_{k\neq j} b_{jk}^2 \end{aligned} \tag{8.59}$$

The δ-peaks in (8.37) are now replaced by normalized Gaussian functions. The noise spectrum becomes

$$\Gamma_{ij}(\omega) = \sum_{\alpha,\beta} p_\alpha |\langle\alpha| \hat{H}^{\mathrm{B}}_{\mathrm{I}i} \hat{I}_{\mathrm{z}\,i}(t) + \hat{H}^{\mathrm{B}}_{\mathrm{I}j} \hat{I}_{\mathrm{z}\,j}(t) |\beta\rangle|^2 \frac{1}{\sqrt{2\,\pi\,\sigma^2_{\alpha\beta}}} \mathrm{e}^{-\frac{(\omega - E_{\alpha\beta})^2}{2\,\sigma^2_{\alpha\beta}}} \tag{8.60}$$

The 2nd moment of this function approximates to

$$\int_{-\infty}^{\infty} \Gamma_{ij}(\omega)\,\mathrm{d}\omega \approx \sum_{\alpha,\beta} \frac{1}{4} |\langle\alpha| \hat{H}^{\mathrm{B}}_{\mathrm{I}i} \hat{I}_{\mathrm{z}\,i}(t) + \hat{H}^{\mathrm{B}}_{\mathrm{I}j} \hat{I}_{\mathrm{z}\,j}(t) |\beta\rangle|^2 (\sigma^2_{\alpha,\beta} + E^2_{\alpha,\beta}). \tag{8.61}$$

By combining (8.59) an (8.61) we can calculate the line widths

$$\sigma^2_{ij\ +-} = \frac{b_{ij}^2 + \Delta_{ij}^2}{4\, b_{ij}^2\, \Delta_{ij}^2} \sum_{k\neq i,j} b_{ik}^2\ {\hat{H}^{\mathrm{B}}_{\mathrm{I}i}}^2 + b_{jk}^2\ {\hat{H}^{\mathrm{B}}_{\mathrm{I}j}}^2 . \tag{8.62}$$

σ_{+-} denotes the equal broadening of the two corresponding peaks at $\omega = \pm E_{+-}$. We can discriminate several cases. If $\sigma_{ij\ +-} \ll |\hat{H}^{\mathrm{B}}_{\mathrm{I}i} - \hat{H}^{\mathrm{B}}_{\mathrm{I}j}|$ distinct peaks show in the NSD, while in the case of $\sigma_{ij\ +-} \gg |\hat{H}^{\mathrm{B}}_{\mathrm{I}i} - \hat{H}^{\mathrm{B}}_{\mathrm{I}j}|$ the two peaks merge to a single peak with a maximum at $\omega = 0$. This is visualized in fig. 8.4. In case of the NV even at natural ^{13}C abundance the bath is so diluted that the first case is most likely. If $\Delta_{ij} < b_{ij}$ the broadening of the line is in the order of the nuclear line width after the Van Vleck formula (8.57). If on the other hand $\Delta_{ij} \gg b_{ij}$ leads to $\sigma_{ij\ +-} \sim \Delta_{ij}$ and $\sigma_{ij\ +-} \approx E_{ij}$ again these lines merge and form a single peak at $\omega = 0$. Far parted spin pairs thus form the low frequency part of the NSD, While close by pairs give rise to

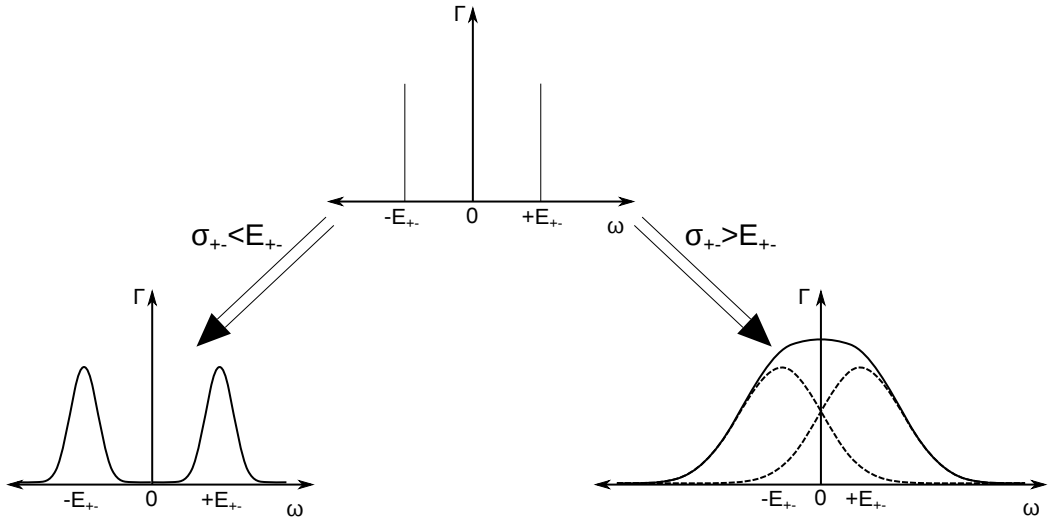

Figure 8.4.: Broadening of the noise peaks. If the line width is smaller than the frequency of the noise peak distinct features remain. Otherwise the two corresponding peaks merge to a single peak at $\omega = 0$.

distinct features which are in principle possible to detect as a echo amplitude modulation. We are now able to write the complete NSD for aligned magnetic field. In the high temperature limit It is symmetric to $\omega = 0$, we thus restrict ourself to the positive branch

$$\Gamma(\omega) = \sum_i \sum_{j>i} \frac{1}{8} \left(c_{\mathrm{ix}}^2 + c_{\mathrm{iy}}^2\right) \frac{1}{\sigma_i} \mathrm{e}^{-\frac{(\omega - E_i)^2}{2\,\sigma_i^2}} + A_{ij}^{\mathrm{rms}\,2}\ \delta(\omega) + 4\,\frac{b_{ij}^2\,\Delta_{ij}^2}{b_{ij}^2 + \Delta_{ij}^2} \frac{1}{\sqrt{2\,\pi\,\sigma_{ij}^2}} \mathrm{e}^{-\frac{(\omega - E_{ij})^2}{2\,\sigma_{ij}^2}}, \tag{8.63}$$

with E_i the Larmor frequency of $^{13}C_i$.

If the $m_S = 0$ state is part of the observed superposition state $\hat{H}_{\mathrm{I}i}^{\mathrm{B}} = 0$ in first order. So all "Larmor" contributions to the noise pile at the unperturbed Larmor frequency $\omega_{\mathrm{L}} = \gamma_n\,\hbar^2\,B$ forming a dominant feature (fig. 8.5. For the double quantum transition at slightly higher magnetic fields where $\omega_{\mathrm{L}} > \bar{\hat{H}}_{\mathrm{I}i}^{\mathrm{B}}$ the combined Larmor lines form again such a feature. At natural and lower abundance the flip-flop part is an order of magnitude lower than the Larmor part and may thus be neglected at the calculation of spin echo data. The static part $A^{\mathrm{rms}\,2}$ on the other hand is of the same order of magnitude than the Larmor peak and is responsible for the rapid decay of the *FID* signal.

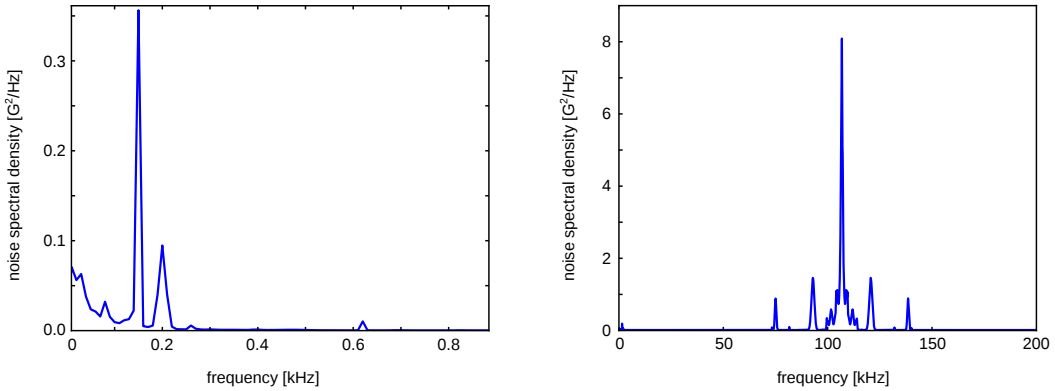

Figure 8.5.: **A** Shows an example of the flip-flop-part of the NSD at 1.1% ^{13}C abundance. Carbon sites within 5 nm of the NV were taken into account. **B** Full noise spectral density at 1.1% ^{13}C abundance again calculated up to 5 nm distance from the NV. The secondary maxima originate from close by ^{13}C sites in the $m_S = -1$ part of the NSD.

8.2.3. The Filter function

The second step in understanding dynamic decoupling is the application of the filter function $S(\tau, \omega)$. For purely classical noise represented by a fluctuating magnetic field $B(t)$ with $\bar{B}(t) = 0$ one would calculate the outcome of e.g. a Hahn echo experiment 3.7 by

$$\langle 1|\psi(t)\rangle \propto \int_0^{\frac{\tau}{2}} B(t)\,\mathrm{d}t - \int_{\frac{\tau}{2}}^{\tau} B(t)\,\mathrm{d}t \tag{8.64}$$

where at $t = 0$ the first Hadamard gate started the sequence. At $t = \tau/2$ the Pauli gate inverted the dynamic by flipping the spin. Finally at $t = \tau$ we read out the result. To simplify (8.64) we introduce a filter function (see fig. 8.6)

$$\tilde{S}(\tau, t) = \begin{cases} 0 & \text{for } t < 0 \\ 1 & \text{for } 0 < t < \frac{\tau}{2} \\ -1 & \text{for } \frac{\tau}{2} < t < \tau \\ 0 & \text{for } \tau < t. \end{cases} \tag{8.65}$$

This lets us write

$$\langle 1|\psi(t)\rangle \propto \int_{-\infty}^{\infty} \tilde{S}(t)\, B(t)\,\mathrm{d}t. \tag{8.66}$$

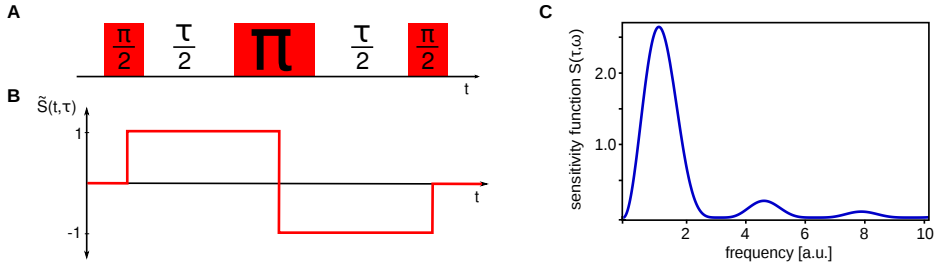

Figure 8.6.: On the right hand side the transition from the pulse sequence of the Hahn echo (a) to the time domain filter function $\tilde{S}(\tau, t)$ (b) is shown. The corresponding frequency domain filter function $S(\tau, \omega)$ on the right (c) is the Fourier transform squared of $\tilde{S}(\tau, t)$.

The same thing can be done in the quantum case. As established in section 8.1 the system is sensitive to frequencies present in the system Hamiltonian. All the single frequency dynamics superpose

$$\rho_{11}(t, \tau) = \prod_i \rho_{11}(\omega_i, t). \tag{8.67}$$

These dynamics are solutions to the Lindblad master equation (8.21)

$$\rho_{11}(\omega_i, t) = \mathrm{e}^{\left(-S(\omega_i)\,\tilde{\Gamma}(\omega_i)\,t\right)}. \tag{8.68}$$

We end up with a decay parameter

$$R = \sum_{i=0}^{\infty} S(\omega_i)\,\tilde{\Gamma}(\omega_i) \Rightarrow \int_0^{\infty} S(\omega)\,\tilde{\Gamma}(\omega)\,\mathrm{d}\omega. \tag{8.69}$$

Because the NV Hamiltonian is time independent the filter function only depends on the application of microwave radiation to the system. In order to describe pulsed experiments we assume the pulse duration to be short against the free induction time between the pulses. These so called delta shaped pulses do not cause a sensitivity component at the Rabi frequency. So the outcome of an echo experiment is independent of the microwave intensity as long as the above assumption holds. The control pulses lead to the same filter function $\tilde{S}(\tau, t)$ as in the classical case. In the frequency domain this gives us the filter function

$$S(\tau, \omega) = |\int_{-\infty}^{\infty} \mathrm{e}^{\mathrm{i}\,\omega\,s}\,\tilde{S}(\tau, t)\,\mathrm{d}s|^2. \tag{8.70}$$

For the above Hahn echo this is

$$S(\tau,\omega) = (2(-1+\cos^2\tau\,\omega)^2)/(\pi\,\omega^2). \tag{8.71}$$

In the following we discuss the most relevant dynamic decoupling sequences with their filter functions, in the presence of distinct features in the NSD.

8.3. Simulated Measurement Outcomes

As we have seen the NSD in combination with the filter function defines the decay parameter R. Because the filter function depends on the duration of the experiment τ R is as well

$$R \Rightarrow R(\tau), \tag{8.72}$$

which in general makes the decay not mono-exponential as the Lindblad equation would suggest. The coherence can actually assume a bigger value for a bigger τ. One could argue that therefore non Markovian effects are introduced to the system. But these revivals are not due to the system-bath interaction. The dynamics of the system that lead to the spin echo at $t = \tau$ are not captured by changing τ. As sketched in (fig. 3.7) a free induction decay takes place after the preparation of the initial state and is followed by a series of echoes. These dynamics can be observed e.g. in ESR measurements. The decay monitored by our measurement scheme only captures the τ dependence of the spin echo amplitude. Non Markovian environmental effects would show in the dynamics of the spin system rather than in the observed value.

In the following we will discuss the application of several pulse sequences to the NV with emphasis on the effect of the Larmor noise.

8.3.1. Free Induction Decay

is the simplest decoherence experiment. It is described in section 3.7. The filter function

$$\tilde{S}(\tau,t) = \begin{cases} 0 & \text{for } t < 0 \\ 1 & \text{for } 0 < t < \tau \\ 0 & \text{for } \tau < t. \end{cases} \tag{8.73}$$

leads to

$$S(\tau,\omega) = \frac{2\,\sin^2(\omega\,t)}{\pi\,\omega^2}. \tag{8.74}$$

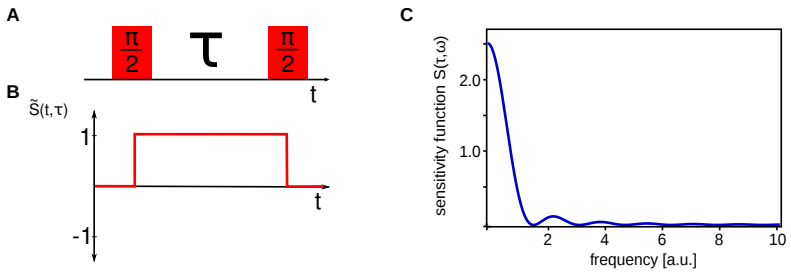

Figure 8.7.: On the right hand side the transition from the pulse sequence of the Hahn echo (a) to the time domain filter function $\tilde{S}(\tau, t)$ (b) is shown. The corresponding frequency domain filter function $S(\tau, \omega)$ on the right (c) is the Fourier transform squared of $\tilde{S}(\tau, t)$.

As we can see from fig. 8.7 this sequence is maximally sensitive at $\omega = 0$. On the one hand it gathers all low frequency components of $\Gamma(\omega)$ especially A^{rms}. Therefore T_2^* is normally 2 orders of magnitude shorter than T_2 of the same NV. On the other hand one is able to measure small dc-fields with this pulse sequence.

8.3.2. Hahn Echo

The Hahn echo sequence is described in in section 3.7. Its sensitivity function is (8.71) is shown in fig. 8.6

$$S_{\text{Hahn}}(\tau, \omega) = \frac{2(-1 + \cos^2 \tau\, \omega)^2}{\pi\, \omega^2}. \tag{8.75}$$

With the application of this sequence the system becomes completely insensitive to the dc-part of the NSD. In the low frequency limit the sensitivity increases quadratically with the frequency. Therefore it is a first order dynamic decoupling. At low magnetic fields the Larmor noise is the dominant source of decoherence. Its amplitude scales linearly with the ^{13}C concentration. T_2 should therefore scale the same way. The measurement data shown in fig. 5.1 supports this dependence.

8.3.3. Carr, Purcell, Meiboom, Gill sequence

The Carr, Purcell, Meiboom, Gill sequence or short CPMG is one natural extension to the Hahn echo sequence [19]. The idea is to successively refocus the spin echo by attaching the same echo sequence over and over again. In the original sequence τ is kept constant and one echo is attached with each

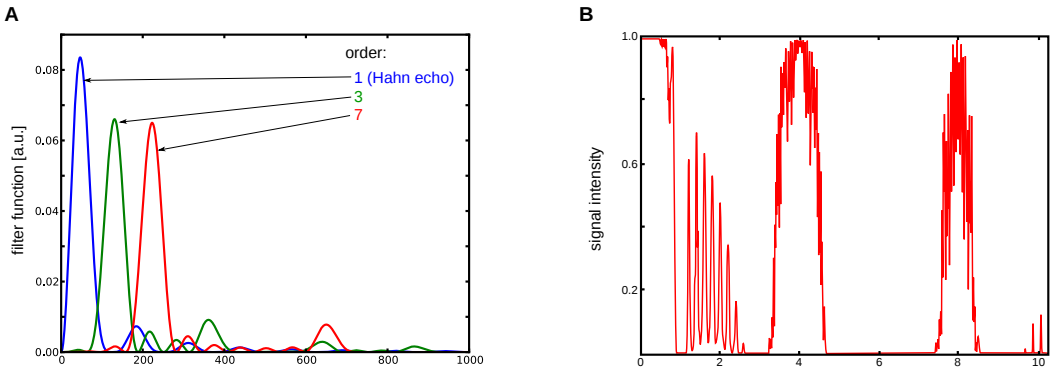

Figure 8.8.: **A** Filter functions of the CPMG pulse sequences of the order one, four and seven at the same τ. The insensitive low frequency region is expanded as well as the number of secondary peaks increases. **B** Exemplary CPMG signal with constant order and varying τ calculated with a NSD as in fig. 8.6.

iteration of the measurement. For better comparison with other sequences it is also possible to fix the number of π-pulses, the order n of the sequence and vary the measurement time τ. The fraction of τ at which the j^{th} π-pulse occurs is given by

$$\delta_{\text{CPMG}}(j,n) = \frac{2*j-1}{2*n}. \tag{8.76}$$

From there we easily get $\tilde{S}(\tau,t)$. The analytic expressions for $S(\tau,\omega)$ get somewhat cumbersome. Compared with the Hahn echo filter function the CPMG features a wider insensitive area at low frequencies. Similar to diffraction at a lattice secondary sensitivity peaks arise with rising order while the main peaks become sharper. The $1/\omega^2$ envelope remains in all orders. Therefore the CPMG is well suited to scan the NSD for distinct features with fixed high as possible order with increasing τ. To maximally prolong the coherence time it is best to choose $\tau_{n=1}$ such that it is insensitive to any noise peaks and from there increasing the order and τ accordingly [70].

8.3.4. Uhrig Dynamic Decoupling

The Uhrig dynamic decoupling sequence (UDD) is the most sophisticated dynamic decoupling sequence at the moment [99]. It is proven best to maintain the coherence of a TLS. Best in the sense that it has the flattest low frequency sensitivity for a given order. The π-pulses are not evenly distributed over τ

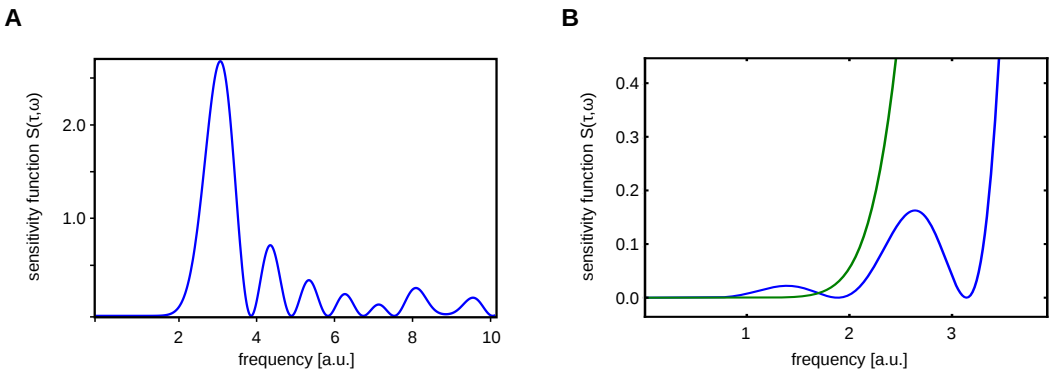

Figure 8.9.: **A** A filter function of the UDD pulse sequences of the order 7. Due to the non equidistant pulses the filter function is complicated above the cutoff frequency. **B** Comparison of the low frequency behavior of the CPMG sequence (blue) and the UDD sequence (green) both of order 7. The UDD remains flat while CPMG has its first secondary peak.

but like

$$\delta_{\mathrm{UDD}}(j,n) := \sin^2\left(\frac{\pi\, j}{2*n+2}\right). \tag{8.77}$$

This variety of time spaces introduce a lot of frequencies to the filter function. After the first rise of sensitivity $S_{\mathrm{UDD}}(\tau,\omega)$ never approaches zero again for a sufficiently long frequency space to become insensitive to the Larmor peak. Thus there are no revivals of the coherence after the first drop. Nonetheless it maintains the coherence longest before that.

To check whether the first and second order correlation functions are sufficient we performed disjoint cluster expansion [104, 64] simulations of the various pulse sequences. Including 1000 ^{13}C in clusters up to 6 nuclear spins we include correlation functions up to the 6^{th} order. The chopped interactions are in the order of Hz so they should have no effect on the system dynamics in the μs range of the measurements conducted.

8.4. Sensing Spins Outside the Diamond

Now that we have a pretty good understanding of decoherence due to ^{13}C inside the diamond we like to go a step further to sense other noise sources coupling to the NV. One possibility would be to sense the closest ^{13}C or ^{13}C-pairs [106]. One step further it would be great to sense spins outside the diamond, probing

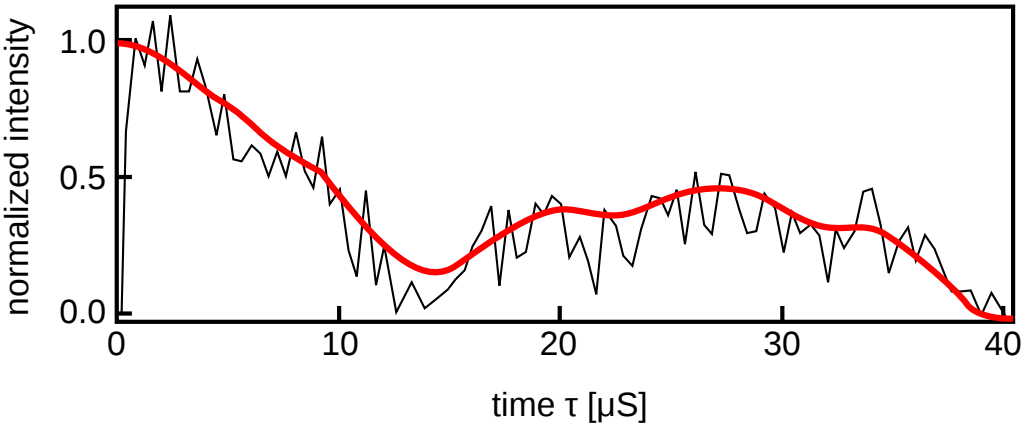

Figure 8.10.: The black line shows Hahn echo data of a NV close to the PMMA coated diamond surface. The red line represents the estimated signal assuming two strong noise features one at the carbon and one at the hydrogen Larmor frequency. The presence of the hydrogen line could not be confirmed by CPMG or UDD, so it is unclear whether it is really the hydrogen on top of the diamond, that causes this echo modulation.

its chemical environment. To do so the NV center has to be very close to the diamond surface. 3 to 5 nm are feasible without complications like blinking [98]. Because the noise amplitude scales like r^{-6} one needs $6.5 \cdot 10^5$ times the spin density at 5 nm or $2.2 \cdot 10^{-4}$ at 4 nm to have the same noise amplitude. If the spin species we want to detect is rather dense outside the diamond it could produce a sufficiently strong Larmor peak in the NSD. The hydrogen nuclear spin seems to be a good candidate for such an approach. It is abundant in organic compounds and can thus easily be applied to the diamond surface. We used PMMA ($(C_5O_2H_8)_n$) to coat the diamond. This should give rise to an additional peak in the NSD of NVs close to the surface. Because of its sharp sensitivity peaks the CPMG sequence should be best suited to sense small features in the NSD. UDD has the advantage that it is in essence insensitive to all noise below its cutoff frequency. It may be interesting to sense noise features of higher frequency than the ^{13}C Larmor. For the ease of application we also take the Hahn echo sequence into account. To estimate the effect we assumed various peak amplitudes relative to the carbon peak at the hydrogen Larmor frequency. The g-factor of hydrogen is $4,258\,\mathrm{kHz/G}$ roughly 4 times the ^{13}C g-factor. The hydrogen signature should therefore be visible as Echo amplitude modulation before the first collapse. In the following figures 8.11-8.14 qualitative results are shown. For a H-Larmor-peak of the same amplitude

and roughly the threefold width of the ^{13}C-peak the hydrogen fingerprint is visible even in the Hahn echo (fig. 8.11). If the peak has less amplitude the signature vanishes(fig. 8.12). The application of the CPMG sequence gives better results even at as low order as CPMG_{10}. Here the full signal of the H CPMG is visible before the first drop due to the carbon Larmor (fig. 8.13 and 8.12). The problem is the small amplitude of the hydrogen signature in combination with the anyway complicated structure of the CPMG signal. It can easily be mistaken as shot noise or coherently coupling ^{13}C nuclei. The sharpening of the ^{13}C revivals can not be taken as an indication, because the width of the revivals varies with the ^{13}C configuration from NV to NV.

In fig. 8.10 Hahn echo measurement data of the PMMA-coated diamond is shown. It features the threefold structure like in fig. 8.11. So this could be due to the hydrogen spins on the surface of the diamond. Without the PMMA it does not show these modulations, so the effect originates from the surface. At higher magnetic fields this threefold feature is replaced by a twofold feature we can not account for at the moment (fig. 8.10). To be sure we have to retrieve the NSD from the measurement data and confirm the Larmor frequency.

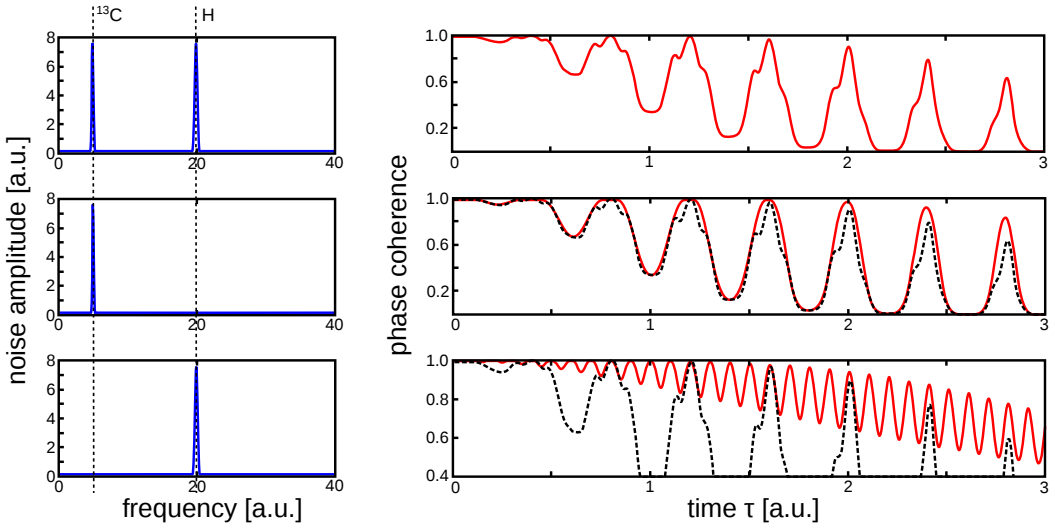

Figure 8.11.: On the left hand side the NSD used to calculate the Hahn echo signal on the right. The first line shows the signal in the presence of a ^{13}C peak as well a H peak of equal strength. The second line depicts the carbon signal only, while the third line shows the hydrogen only result. The signature of the H line is clearly visible as a three fold modulation on the ^{13}C dominated decay of the NV's coherence.

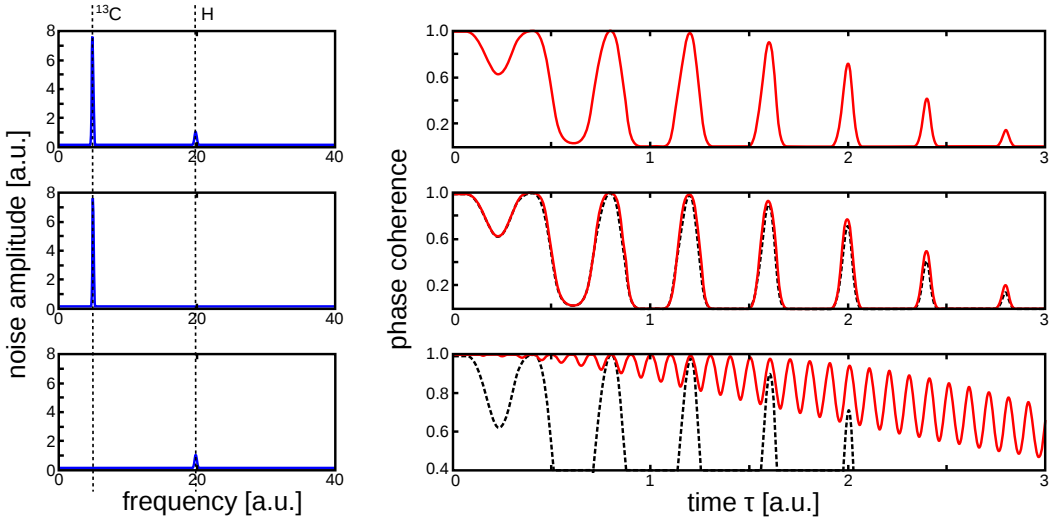

Figure 8.12.: If the relative amplitude of the H peak is reduced its imprint gets lost. At the ratio of 1/10 virtually nothing is left.

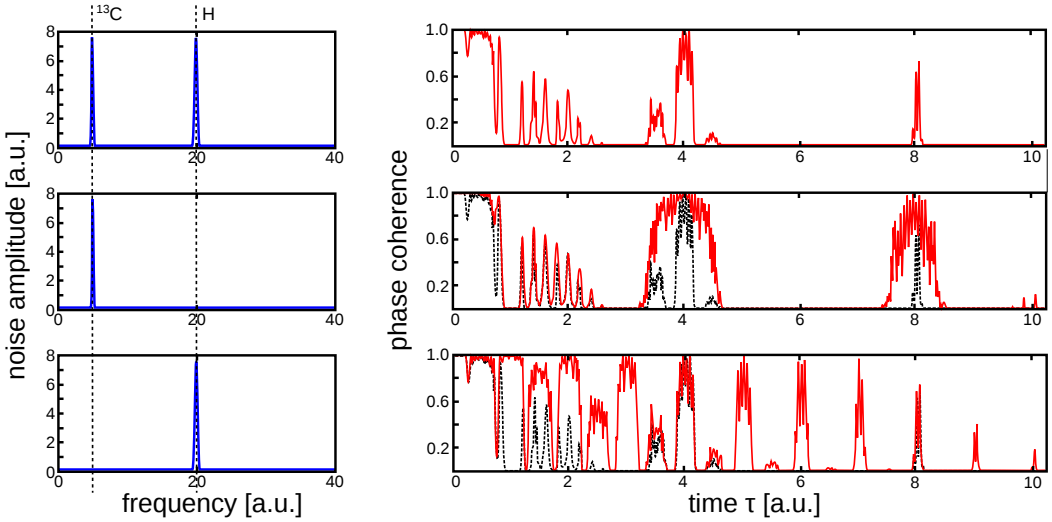

Figure 8.13.: Here the application of a CPMG_{10} sequence is simulated for the case of comparable strong noise features of ^{13}C a H. Before the first drop one can clearly see the complete H signature. At higher τ the unperturbed signal is altered drastically as well.

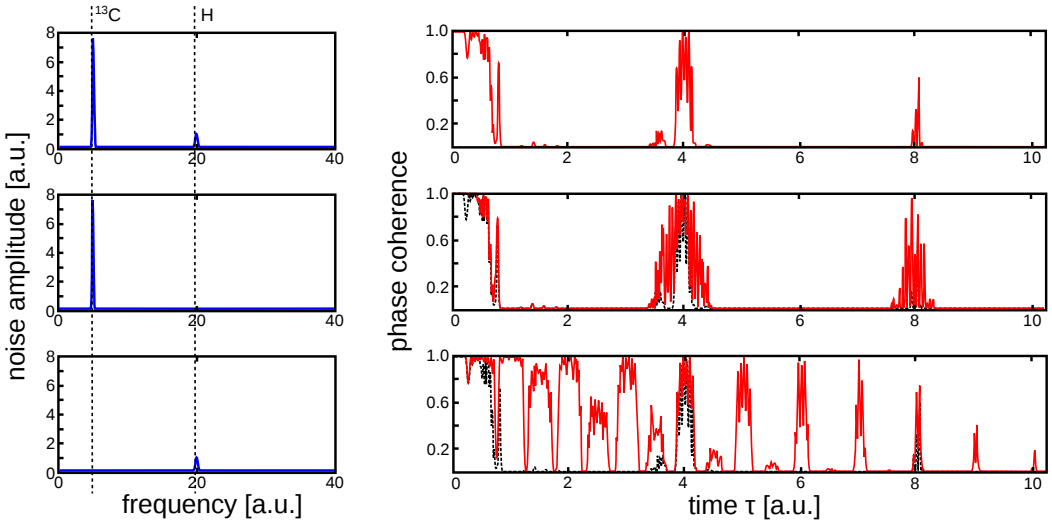

Figure 8.14.: Even at the amplitude ratio of 1/10 the combined signal shows the hydrogen fingerprint before the first drop as well as later on.

Part III.

Appendices

A. Conclusion

In the present work we have expanded the understanding of the dynamics of the NV center in diamond in itself as well as with its environment in the diamond lattice. By doing so we further approached the DiVincenzo criteria for a scalable quantum computer [24].

The first criterion is to have a scalable physical system with well characterized qubits. The NV quantum register is built as follows: First of all the electron spin of the system functions as a central qubit. All additional qubits are addressed via the electron spin, so it normally takes the role of an anzilla qubit. Nuclear spins in the near vicinity serve as the actual computing register. The nitrogen nuclear spin and ^{13}C nuclear spins both with strong coupling by contact interaction or weak coupling by magnetic dipole dipole interaction are feasible qubits that are accessible via the NV. To further increase the register additional NVs have to be addressed.

As a second criterion one has to be able to initialize the qubits into a simple pure state. The electron spin qubit is initialized by shining laser light on the system. By previous means additional spins are initialized by selective gates followed by manipulation in the $m_S = -1$ manifold of the electron qubit [74]. We are now able to polarize additional nuclear spins by conducting a projective quantum non-demolition measurement [75]. Weakly coupling nuclear spins can thus be polarized.

DiVincenzos third criterion is to have long coherence times in comparison with the gate duration. We found that the main source of decoherence in the diamond lattice is the ^{13}C nuclear spin population. T_2^* scales like the square root of the ^{13}C concentration in the lattice while T_2 shows linear dependency [67]. With that knowledge isotopically pure diamond samples were manufactured. That drastically increased the coherence times up to milliseconds [5] allowing in principle to access more remote ^{13}C nuclear spins as qubits. The elongation additionally enabled us to implement quantum gates between two NV electron qubits located approximately 10 nm apart from one another.

This directly leads us to the fourth criterion, the ability to apply a universal set of quantum gates. A universal set is the application of a CNOT gate and arbitrary single qubit phase gates. We demonstrated the CNOT gate between the two electron spins by observing dynamics of qubit A that depend

on the state of qubit B. In addition we effectively applied the combination of a Hadamard gate and a CNOT to generate entanglement between the two qubits. Unfortunately the coherence times of the observed spin pair were too short to actually observe entanglement.

The final criterion is to have the capability to do qubit specific measurement. Because our quantum register is accessible only via the electron qubit this is the requirement that is most complicated to accomplish for the NV center. The strong interacting carbon qubits are scrambled by the read out laser pulse, so they are contrary to the former opinion not really good candidates for qubits of the register. We found a scheme to perform a quantum-non-demolition (QND) measurement on the nitrogen nuclear spin [75], which is the most versatile form of measurement of a quantum system. For example QND measurement on single qubits simplifies quantum error correction and allows to observe the quantum zeno effect. In principle it is possible to perform QND measurements on weak coupled ^{13}C qubits as well. Because they are not perturbed by the readout laser sequential readout of the every nuclear spin qubit of the register should be possible, thus fullfilling DeVincenzo's requirement.

Additionally we understood the special shape of the spin echo signal of the electron qubit in the presence of the ^{13}C bath. Collapses and revivals of the signal are ascribed to incoherent Larmor precession of the carbon spins. Thus even the complicated shape of more advanced dynamic decoupling sequences like CPMG or UDD could be accounted for. It was shown that the first order correlations are responsible for most of the decoherence. The second order contribution is two orders of magnitude smaller already. By the understanding of this mechanism the effect of nuclear spins on the surface of the diamond could be predicted. Preliminary measurements with NVs close to the diamond surface hint that the predictions are correct.

In the future the inversion of the performed calculation will provide a reliable method to identify these external spins. That way the chemical environment of the diamond will be measurable. Applied on nano diamonds this may e.g. open new possibilities in bio diagnostics.

B. Zusammenfassung

Mit der vorliegenden Arbeit wurde das Verständnis der Dynamik des Nitrogen-Vacancy (NV) Farbzentrums in Diamant, vor allem auch in Hinblick auf seine Kopplung an die Quantenumgebung im Diamant, erweitert. Das NV-Zentrum besteht aus einer Gitterfehlstelle mit einem Stickstoffatom auf einer benachbarten Gitterstelle. Die Einbettung in den Diamant als sehr steife, fast spinfreie Umgebung erlaubt es Quantenexperimente bei Raumtemperatur durchzuführen. Eine geschickte Möglichkeit ein Quantensystem einzuordnen ist anhand der so genannten DiVincenzo-Kriterien [24]. Sie dienen als Richtlinie welche Eigenschaften ein skalierbarer Quantencomputer aufweisen sollte.

Das erste Kriterium ist es, ein skalierbares Quantensystem mit wohl definierten Qubits zu haben. Das zentrale Qubit des NV-Registers bildet der Elektronenspin des Farbzentrums. Über ihn werden alle weiteren Qubits des Registers adressiert und ausgelesen, deswegen kommt ihm zumeist die Rolle eines Anzilla-Qubits zu. Meistens werden die durch Austauschwechselwirkung stark koppelnden ^{13}C-Kernspins der ersten und dritten Schale um die Fehlstelle als Qubits verwendet. Im Laufe dieser Arbeit wurde auch der schwach koppelnde Kernspin des Stickstoffatoms nutzbar gemacht. Prinzipiell können zwischenzeitlich auch entferntere ^{13}C-Kernspins als Qubits adressiert werden. Um das Register weiter zu vergrößern kann man weitere NV-Zentren hinzu nehmen.

Zweitens sollte man in der Lage sein, alle Qubits in einen einfachen, reinen Zustand zu initialisieren. Der NV-Elektronenspin (NV-Spin) wird über seinen intrinsischen Relaxationsmechanismus durch bestrahlen mit grünem Laser initialisiert. Bisher bestand nur die Möglichkeit Kernspin-Qubits durch selektive Quantengatter und darauf folgende Manipulation im $|-1\rangle$ Subraum quasi zu initialisieren. Dies reduziert allerdings den Auslesekontrast auf $1/n + 1$, mit n als der Anzahl der auf diese Weise initialisierten Qubits [74]. Durch eine rückwirkungsfreie Messung (QND) [75] ist es nun möglich, den Stickstoffkernspin ebenfalls in einen Energie-Eigenzustand zu projizieren und damit zu initialisieren. Das selbe Verfahren ist prinzipiell auch bei schwach koppelnden ^{13}C-Kernspins möglich.

Die dritte Anforderung ist es, über eine lange Kohärenzzeit relativ zur Dauer eines Quantengatters zu verfügen. Wir haben herausgefunden, dass die Haupt-

ursache von Dekohärenz das ^{13}C-Spinbad des Diamantgitters ist. Die T_2^*-Zeit skaliert mit der Wurzel der ^{13}C-Konzentration während die T_2-Zeit einen linearen Zusammenhang aufweist [67]. Ausgehend davon wurden die Experimente auf isotopenreine Diamanten verlagert, was die T_2-Zeit in die Größenordnung von Millisekunden verlängerte [5]. Dadurch können sowohl weiter entfernte ^{13}C-Kernspins als Qubits herangezogen werden, als auch Quantengatter zwischen zwei bis zu 30 nm voneinander entfernen NV-Zentren implementiert werden [73].

Das bringt uns zum vierten DiVincenzo Kriterium, die Fähigkeit universelle Quantengatter auf dem Register auszuführen. Das CNOT-Gatter in Verbindung mit beliebigen Einzel-Qubit-Gattern ist ein solches universelles Set. Einzel-Qubit-Operationen sind ohne Schwierigkeiten möglich. Wir haben zusätzlich ein CNOT-Gatter zwischen zwei NV-Spins demonstriert, indem wir auf dem einen Qubit Dynamik nachgewiesen haben die vom Zustand des zweiten Qubit abhängt. Zusätzlich wurde effektiv die nacheinander Ausführung eines Hadamard- und eines CNOT-Gatters gezeigt, die Verschränkung zwischen den beiden Qubits erzeugt. Leider waren die Kohärenzzeiten des gemessenen Paares zu kurz um diese Verschränkung noch nachzuweisen.

Das letzte Kriterium ist, die einzelnen Qubits des Registers selektiv auslesen zu können. Es ist das mit dem NV am schwersten zu realisierende Kriterium, da man nur über den Elektronenspin Zugang zum Register hat. Die stark koppelnden ^{13}C-Kernspins werden vom Auslese-Laser-Puls sehr stark in Mitleidenschaft gezogen. Sie sind daher doch keine optimale Wahl als Register-Qubits. Wir habe jedoch eine Möglichkeit gefunden eine rückwirkungsfreie Messung (QND) am Stickstoffkernspin durchzuführen. Die QND-Messung ist die vielseitigste Form der Messung an einem Quantensystem, sie findet z.B Anwendung bei der Quantenfehlerkorrektur und mit ihrer Hilfe ist es möglich, den Quanten-Zenoeffekt zu beobachten. Es ist prinzipiell möglich QND-Messungen auch an schwach koppelnden ^{13}C-Kernspins auszuführen. Da diese vom Auslese-Laser-Puls nur schwach gestört werden, ist es möglich, das gesamte Register sequentiell auszulesen. Dadurch würde das fünfte DiVincenzo-Kriterium erfüllt.

Wir haben auch die spezielle Form von Spinechos des Elektronenspins in Gegenwart eines ^{13}C Spinbads besser verstanden, indem der periodische Zusammenbruch und die Wiederkehr der Kohärenz dem inkohärenten Larmorrauschen zugeschrieben wurden. Durch Berechnung der spektralen Rauschdichte konnte auch den komplizierten Signalformen der komplexeren Entkopplungssequenzen wie CPMG oder UDD Rechnung getragen werden. Dabei sind die Korrelationen erster Ordnung um circa zwei Größenordnungen schwächer als die erster Ordnung. Über die Methode der spektralen Rauschdichte konnte auch der Effekt von Kernspins auf der Oberfläche des Diamanten auf ober-

flächennahe NVs berechnet werden. Vorläufige Messungen an solchen NVs weisen darauf hin, dass die Vorhersagen korrekt sind. In Zukunft wird die Umkehrung dieser Methode, also die Berechnung der spektralen Rauschdichte aus den Messdaten, eine wirkungsvolle Methode darstellen, um diese Obenflächenspins zu identifizieren und damit die chemische Umgebung des Diamanten zu analysieren. Dies könnte bei Nanodiamanten zu interessanten Möglichkeiten zum Beispiel in der Biophysik führen.

Symbols

Mathematical Conventions

$\hat{O}$	Quantum operator
$\underline{V}$	Vector
$\underline{\underline{M}}$	Matrix
$\mathcal{M}_n$	n^{th} moment

Physical Symbols

τ	Duration of a dynamic decoupling sequence
E	Rhombic zero field splitting
D	Longitudinal zero field splitting
Q	Quatrupole
ω_{R}	Rabi frequency
T_2	Phase coherence time after dynamical decoupling
T_2^*	Phase coherence time
T_1	Longitudinal relaxation time
$T_{2\,\rho}$	Pure dephasing time
$\hat{S}_i$	Generator of rotations about kartesian coordinates for the electron spin
$\hat{I}_i$	Generator of rotations about kartesian coordinates for the nuclear spins
$\hat{H}_{\text{dip}}$	Dipole-dipole interaction Hamiltonian
$\hat{H}_{\text{ac}}$	Hamiltonian of an alternating magnetic field
$\hat{H}_{\text{S}}$	System Hamiltonian
$S(\tau, \omega)$	Filter function
$\Gamma(\omega)$	Noise spectral density

Abbreviations

AFM	Atomic force microscope
CNOT	Controlled not gate
CPMG	Carr, Purcell, Meiboom, Gill sequence
DEER	Double electron electron resonance sequence
GHZ	Greenberger–Horne–Zeilinger state
HPHT	High pressure high temperature method of growing diamond
LAC	Level anticrossing
NSD	Noise spectral density
NV	Nitrogen-vacancy center
ODMR	Optically detected magnetic resonance
STED	Stimulated emission depletion microscopy
UDD	Uhrig dynamic decoupling
ZFS	Zero field splitting

Bibliography

[1] Eisuke Abe, Akira Fujimoto, Junichi Isoya, Satoshi Yamasaki, and Kohei M Itoh. Line broadening and decoherence of electron spins in Phosphorus-Doped silicon due to environmental 29ˆSi nuclear spins. *cond-mat/0512404*, December 2005. Phys. Rev. B 82, 121201 (2010).

[2] A. Abragam. *The Principles of Nuclear Magnetism.* Clarendon Press, reprint edition, April 1994.

[3] Yakir Aharonov, David Z. Albert, and Lev Vaidman. How the result of a measurement of a component of the spin of a spin-1/2 particle can turn out to be 100. *Physical Review Letters*, 60(14):1351, April 1988.

[4] Gopalakrishnan Balasubramanian, I. Y. Chan, Roman Kolesov, Mohannad Al-Hmoud, Julia Tisler, Chang Shin, Changdong Kim, Aleksander Wojcik, Philip R. Hemmer, Anke Krueger, Tobias Hanke, Alfred Leitenstorfer, Rudolf Bratschitsch, Fedor Jelezko, and Jorg Wrachtrup. Nanoscale imaging magnetometry with diamond spins under ambient conditions. *Nature*, 455(7213):648–651, October 2008.

[5] Gopalakrishnan Balasubramanian, Philipp Neumann, Daniel Twitchen, Matthew Markham, Roman Kolesov, Norikazu Mizuochi, Junichi Isoya, Jocelyn Achard, Johannes Beck, Julia Tissler, Vincent Jacques, Philip R. Hemmer, Fedor Jelezko, and Jorg Wrachtrup. Ultralong spin coherence time in isotopically engineered diamond. *Nat Mater*, 8(5):383–387, May 2009.

[6] Adriano Barenco, Charles H. Bennett, Richard Cleve, David P. DiVincenzo, Norman Margolus, Peter Shor, Tycho Sleator, John A. Smolin, and Harald Weinfurter. Elementary gates for quantum computation. *Physical Review A*, 52(5):3457, November 1995.

[7] A. Batalov, V. Jacques, F. Kaiser, P. Siyushev, P. Neumann, L. J. Rogers, R. L. McMurtrie, N. B. Manson, F. Jelezko, and J. Wrachtrup. Low temperature studies of the Excited-State structure of negatively

charged Nitrogen-Vacancy color centers in diamond. *Physical Review Letters*, 102(19):195506, May 2009.

[8] A. Batalov, C. Zierl, T. Gaebel, P. Neumann, I.-Y. Chan, G. Balasubramanian, P. R. Hemmer, F. Jelezko, and J. Wrachtrup. Temporal coherence of photons emitted by single Nitrogen-Vacancy defect centers in diamond using optical Rabi-Oscillations. *Physical Review Letters*, 100(7):077401, February 2008.

[9] J. Baugh, O. Moussa, C. A. Ryan, A. Nayak, and R. Laflamme. Experimental implementation of heat-bath algorithmic cooling using solid-state nuclear magnetic resonance. *Nature*, 438(7067):470–473, November 2005.

[10] JOHN S. BELL. On the problem of hidden variables in quantum mechanics. *Reviews of Modern Physics*, 38(3):447, July 1966.

[11] Charles Bennett, David DiVincenzo, John Smolin, and William Wootters. Mixed-state entanglement and quantum error correction. *Physical Review A*, 54(5):3824–3851, November 1996.

[12] Charles H. Bennett, Gilles Brassard, Claude Crépeau, Richard Jozsa, Asher Peres, and William K. Wootters. Teleporting an unknown quantum state via dual classical and Einstein-Podolsky-Rosen channels. *Physical Review Letters*, 70(13):1895, March 1993.

[13] CharlesH. Bennett, Francois Bessette, Gilles Brassard, Louis Salvail, and John Smolin. Experimental quantum cryptography. *Journal of Cryptology*, 5(1), 1992.

[14] P. O. Boykin. Algorithmic cooling and scalable NMR quantum computers. *Proceedings of the National Academy of Sciences*, 99(6):3388–3393, March 2002.

[15] Heinz-Peter Breuer and Francesco Petruccione. *The Theory of Open Quantum Systems*. Oxford University Press, USA, August 2002.

[16] R. Hanbury Brown and R. Q. Twiss. Interferometry of the intensity fluctuations in light. i. basic theory: The correlation between photons in coherent beams of radiation. *Proceedings of the Royal Society of London. Series A. Mathematical and Physical Sciences*, 242(1230):300 –324, November 1957.

[17] I. Bugiel, K. Koenig, and H. Wabnitz. Investigation of cells by fluorescence laser scanning microscopy with subnanosecond time resolution. *Lasers in the Life Sciences*, 3(1):47–53, 1989.

[18] P. Cappellaro, L. Jiang, J. Hodges, and M. Lukin. Coherence and control of quantum registers based on electronic spin in a nuclear spin bath. *Physical Review Letters*, 102(21), May 2009.

[19] H. Y. Carr and E. M. Purcell. Effects of diffusion on free precession in nuclear magnetic resonance experiments. *Physical Review*, 94(3):630, May 1954.

[20] Carlton M. Caves, Kip S. Thorne, Ronald W. P. Drever, Vernon D. Sandberg, and Mark Zimmermann. On the measurement of a weak classical force coupled to a quantum-mechanical oscillator. i. issues of principle. *Reviews of Modern Physics*, 52(2):341, April 1980.

[21] L. Childress, M. V. Gurudev Dutt, J. M. Taylor, A. S. Zibrov, F. Jelezko, J. Wrachtrup, P. R. Hemmer, and M. D. Lukin. Coherent dynamics of coupled electron and nuclear spin qubits in diamond. *Science*, 314(5797):281 –285, October 2006.

[22] M. H Devoret, A. Wallraff, and J. M Martinis. Superconducting qubits: A short review. *cond-mat/0411174*, November 2004.

[23] David P. DiVincenzo. Two-bit gates are universal for quantum computation. *Physical Review A*, 51(2):1015, February 1995.

[24] David P DiVincenzo. The physical implementation of quantum computation. *Fortschritte der Physik*, 48(9-11):771–783, September 2000.

[25] V. Dobrovitski, A. Feiguin, D. Awschalom, and R. Hanson. Decoherence dynamics of a single spin versus spin ensemble. *Physical Review B*, 77(24), June 2008.

[26] F. Dolde, H. Fedder, M. W. Doherty, T. Nobauer, F. Rempp, G. Balasubramanian, T. Wolf, F. Reinhard, L. C. L. Hollenberg, F. Jelezko, and J. Wrachtrup. Electric-field sensing using single diamond spins. *Nat Phys*, 7(6):459–463, June 2011.

[27] D. Drung, C. Assmann, J. Beyer, A. Kirste, M. Peters, F. Ruede, and T. Schurig. Highly sensitive and Easy-to-Use SQUID sensors. *IEEE Transactions on Applied Superconductivity*, 17(2):699–704, June 2007.

[28] W. Duer, G. Vidal, and J. I. Cirac. Three qubits can be entangled in two inequivalent ways. *Physical Review A*, 62(6):062314, November 2000.

[29] M. V. G. Dutt, L. Childress, L. Jiang, E. Togan, J. Maze, F. Jelezko, A. S. Zibrov, P. R. Hemmer, and M. D. Lukin. Quantum register based on individual electronic and nuclear spin qubits in diamond. *Science*, 316(5829):1312–1316, June 2007.

[30] H. Fedder, F. Dolde, F. Rempp, T. Wolf, P. Hemmer, F. Jelezko, and J. Wrachtrup. Towards t 1-limited magnetic resonance imaging using rabi beats. *Applied Physics B*, 102(3):497–502, February 2011.

[31] Richard P. Feynman. Simulating physics with computers. *International Journal of Theoretical Physics*, 21(6-7):467–488, June 1982.

[32] T. Foerster. 27(7), 1959.

[33] L. Frunzio, A. Wallraff, D. Schuster, J. Majer, and R. Schoelkopf. Fabrication and characterization of superconducting circuit QED devices for quantum computation. *IEEE Transactions on Applied Superconductivity*, 15(2):860– 863, June 2005.

[34] G. D. Fuchs, V. V. Dobrovitski, D. M. Toyli, F. J. Heremans, and D. D. Awschalom. Gigahertz dynamics of a strongly driven single quantum spin. *Science*, 326(5959):1520–1522, November 2009.

[35] Adam Gali, Maria Fyta, and Efthimios Kaxiras. Ab initio supercell calculations on nitrogen-vacancy center in diamond: Electronic structure and hyperfine tensors. *Physical Review B*, 77(15):155206, April 2008.

[36] Adam Gali, Erik Janzén, Péter Deák, Georg Kresse, and Efthimios Kaxiras. Theory of Spin-Conserving excitation of the N-V- center in diamond. *Physical Review Letters*, 103(18), October 2009.

[37] J. Gemmer, M. Michel, Mathias Michel, and Guenter Mahler. *Quantum thermodynamics: emergence of thermodynamic behavior within composite quantum systems*. Springer, 2004.

[38] Neil A. Gershenfeld and Isaac L. Chuang. Bulk Spin-Resonance quantum computation. *Science*, 275(5298):350 –356, January 1997.

[39] Daniel M Greenberger, Michael A Horne, and Anton Zeilinger. Going beyond bell's theorem. *0712.0921*, December 2007. in: 'Bell's Theorem,

Quantum Theory, and Conceptions of the Universe', M. Kafatos (Ed.), Kluwer, Dordrecht, 69-72 (1989).

[40] E. L. Hahn. Spin echoes. *Physical Review*, 80(4):580, November 1950.

[41] R. HANBURY BROWN and R. Q. TWISS. A test of a new type of stellar interferometer on sirius. *Nature*, 178(4541):1046–1048, November 1956.

[42] J. B. Hannay. On the artificial formation of the diamond. *Proceedings of the Royal Society of London*, 30(200-205):450 –461, January 1879.

[43] Sung Ui Hong, Jin Soo Kim, Jin Hong Lee, Ho-Sang Kwack, Won Seok Han, and Dae Kon Oh. Properties of self-assembled InAs quantum dots grown by various growth techniques. *Journal of Crystal Growth*, 260(3-4):343–347, January 2004.

[44] M Horodecki. Separability of mixed states: necessary and sufficient conditions. *Physics Letters A*, 223(1-2):1–8, November 1996.

[45] Ryszard Horodecki, Michał Horodecki, and Karol Horodecki. Quantum entanglement. *Reviews of Modern Physics*, 81(2):865–942, June 2009.

[46] S. F. Huelga, T. W. Marshall, and E. Santos. Proposed test for realist theories using rydberg atoms coupled to a high-Q resonator. *Physical Review A*, 52(4):R2497, October 1995.

[47] S. F Huelga, T. W Marshall, and E Santos. Observation of quantum coherence by means of temporal bell-type inequalities. *Europhysics Letters (EPL)*, 38(4):249–254, May 1997.

[48] N. Imoto, H. A. Haus, and Y. Yamamoto. Quantum nondemolition measurement of the photon number via the optical kerr effect. *Physical Review A*, 32(4):2287, October 1985.

[49] V. Jacques, P. Neumann, J. Beck, M. Markham, D. Twitchen, J. Meijer, F. Kaiser, G. Balasubramanian, F. Jelezko, and J. Wrachtrup. Dynamic polarization of single nuclear spins by optical pumping of Nitrogen-Vacancy color centers in diamond at room temperature. *Physical Review Letters*, 102(5), February 2009.

[50] F. Jelezko, T. Gaebel, I. Popa, M. Domhan, A. Gruber, and J. Wrachtrup. Observation of coherent oscillation of a single nuclear

spin and realization of a Two-Qubit conditional quantum gate. *Physical Review Letters*, 93(13):130501, 2004.

[51] L. Jiang, J. S. Hodges, J. R. Maze, P. Maurer, J. M. Taylor, D. G. Cory, P. R. Hemmer, R. L. Walsworth, A. Yacoby, A. S. Zibrov, and M. D. Lukin. Repetitive readout of a single electronic spin via quantum logic with nuclear spin ancillae. *Science*, 326(5950):267–272, September 2009.

[52] Liang Jiang, J. Taylor, Kae Nemoto, W. Munro, Rodney Van Meter, and M. Lukin. Quantum repeater with encoding. *Physical Review A*, 79(3), March 2009.

[53] Liang Jiang, Jacob M. Taylor, Anders S. Sørensen, and Mikhail D. Lukin. Distributed quantum computation based on small quantum registers. *Physical Review A*, 76(6):062323, December 2007.

[54] Stefan Joisten. *Implantation von einzelenen NV-Defekten in Diamant*. Universitaet Stuttgart, Stuttgart, 2009.

[55] Richard Jozsa. Fidelity for mixed quantum states. *Journal of Modern Optics*, 41(12):2315–2323, December 1994.

[56] B. E. Kane. A silicon-based nuclear spin quantum computer. *Nature*, 393(6681):133–137, May 1998.

[57] Lowell D. Kispert. Electron-Electron double resonance. In Sandra R. Eaton, Gareth R. Eaton, and Lawrence J. Berliner, editors, *Biomedical EPR, Part B: Methodology, Instrumentation, and Dynamics*, volume 24/B, pages 165–197. Kluwer Academic Publishers-Plenum Publishers, New York, 2005.

[58] E. Knill. Quantum computing with realistically noisy devices. *Nature*, 434(7029):39–44, March 2005.

[59] W Kohn. Solid state physics. In *Solid State Physics*, volume 5, page 257ff. Academic Press, New York, 1957.

[60] A. J. Leggett and Anupam Garg. Quantum mechanics versus macroscopic realism: Is the flux there when nobody looks? *Physical Review Letters*, 54(9):857, March 1985.

[61] L. Marseglia, J. P. Hadden, A. C. Stanley-Clarke, J. P. Harrison, B. Patton, Y.-L. D. Ho, B. Naydenov, F. Jelezko, J. Meijer, P. R. Dolan, J. M.

Smith, J. G. Rarity, and J. L. O'Brien. Nanofabricated solid immersion lenses registered to single emitters in diamond. *Applied Physics Letters*, 98(13):133107, 2011.

[62] J R Maze, A Gali, E Togan, Y Chu, A Trifonov, E Kaxiras, and M D Lukin. Properties of nitrogen-vacancy centers in diamond: the group theoretic approach. *New Journal of Physics*, 13(2):025025, February 2011.

[63] J. R. Maze, P. L. Stanwix, J. S. Hodges, S. Hong, J. M. Taylor, P. Cappellaro, L. Jiang, M. V. Gurudev Dutt, E. Togan, A. S. Zibrov, A. Yacoby, R. L. Walsworth, and M. D. Lukin. Nanoscale magnetic sensing with an individual electronic spin in diamond. *Nature*, 455(7213):644–647, October 2008.

[64] J. R. Maze, J. M. Taylor, and M. D. Lukin. Electron spin decoherence of single nitrogen-vacancy defects in diamond. *Physical Review B*, 78(9):094303, 2008.

[65] B. Misra and E. C. G. Sudarshan. The zeno's paradox in quantum theory. *Journal of Mathematical Physics*, 18(4):756, 1977.

[66] Akimasa Miyake and Miki Wadati. *Multipartite Entanglement and Hyperdeterminants*, volume 2. 2002.

[67] N. Mizuochi, P. Neumann, F. Rempp, J. Beck, V. Jacques, P. Siyushev, K. Nakamura, D. Twitchen, H. Watanabe, S. Yamasaki, F. Jelezko, and J. Wrachtrup. Coherence of single spins coupled to a nuclear spin bath of varying density. *Physical Review B*, 80(4), July 2009.

[68] A. H. Myerson, D. J. Szwer, S. C. Webster, D. T. C. Allcock, M. J. Curtis, G. Imreh, J. A. Sherman, D. N. Stacey, A. M. Steane, and D. M. Lucas. High-Fidelity readout of Trapped-Ion qubits. *Physical Review Letters*, 100(20):200502, May 2008.

[69] B. Naydenov, R. Kolesov, A. Batalov, J. Meijer, S. Pezzagna, D. Rogalla, F. Jelezko, and J. Wrachtrup. Engineering single photon emitters by ion implantation in diamond. *Applied Physics Letters*, 95(18):181109, 2009.

[70] Boris Naydenov, Florian Dolde, Liam Hall, Chang Shin, Helmut Fedder, Lloyd Hollenberg, Fedor Jelezko, and Joerg Wrachtrup. Dynamical decoupling of a single-electron spin at room temperature. *Physical Review B*, 83(8), February 2011.

[71] Boris Naydenov, V. Richter, Johannes Beck, Matthias Steiner, Philipp Neumann, Gopalakrishnan Balasubramanian, Jocelyn Achard, Fedor Jelezko, Joerg Wrachtrup, and Rafi Kalish. Enhanced generation of single optically active spins in diamond by ion implantation. *Applied Physics Letters*, 96(16):163108, 2010.

[72] P Neumann, R Kolesov, V Jacques, J Beck, J Tisler, A Batalov, L Rogers, N B Manson, G Balasubramanian, F Jelezko, and J Wrachtrup. Excited-state spectroscopy of single NV defects in diamond using optically detected magnetic resonance. *New Journal of Physics*, 11(1):013017, January 2009.

[73] P. Neumann, R. Kolesov, B. Naydenov, J. Beck, F. Rempp, M. Steiner, V. Jacques, G. Balasubramanian, M. L. Markham, D. J. Twitchen, S. Pezzagna, J. Meijer, J. Twamley, F. Jelezko, and J. Wrachtrup. Quantum register based on coupled electron spins in a room-temperature solid. *Nat Phys*, 6(4):249–253, April 2010.

[74] P. Neumann, N. Mizuochi, F. Rempp, P. Hemmer, H. Watanabe, S. Yamasaki, V. Jacques, T. Gaebel, F. Jelezko, and J. Wrachtrup. Multipartite entanglement among single spins in diamond. *Science*, 320(5881):1326–1329, June 2008.

[75] Philipp Neumann, Johannes Beck, Matthias Steiner, Florian Rempp, Helmut Fedder, Philip R. Hemmer, Joerg Wrachtrup, and Fedor Jelezko. Single-Shot readout of a single nuclear spin. *Science*, 329(5991):542 –544, July 2010.

[76] Michael A. Nielsen and Isaac L. Chuang. *Quantum computation and quantum information*. Cambridge University Press, 2000.

[77] Asher Peres. Separability criterion for density matrices. *Physical Review Letters*, 77(8):1413–1415, August 1996.

[78] S Pezzagna, B Naydenov, F Jelezko, J Wrachtrup, and J Meijer. Creation efficiency of nitrogen-vacancy centres in diamond. *New Journal of Physics*, 12(6):065017, June 2010.

[79] Sébastien Pezzagna, Detlef Rogalla, Dominik Wildanger, Jan Meijer, and Alexander Zaitsev. Creation and nature of optical centres in diamond for single-photon emission—overview and critical remarks. *New Journal of Physics*, 13(3):035024, March 2011.

[80] Sébastien Pezzagna, Dominik Wildanger, Paul Mazarov, Andreas D Wieck, Yanko Sarov, Ivo Rangelow, Boris Naydenov, Fedor Jelezko, Stefan W Hell, and Jan Meijer. Nanoscale engineering and optical addressing of single spins in diamond. *Small*, 6(19):2117–2121, October 2010.

[81] N.F. Ramsey. 78(695), 1950.

[82] A. G Redfield. On the theory of relaxation processes. *IBM J. Res. Dev.*, 1(1):19–31, January 1957. ACM ID: 1661808.

[83] Florian Rempp, Mathias Michel, and Guenter Mahler. Cyclic cooling algorithm. *Physical Review A*, 76(3), September 2007.

[84] E. Rittweger, D. Wildanger, and S. W. Hell. Far-field fluorescence nanoscopy of diamond color centers by ground state depletion. *EPL (Europhysics Letters)*, 86(1):14001, April 2009.

[85] Ángel Rivas, A Douglas K Plato, Susana F Huelga, and Martin B Plenio. Markovian master equations: a critical study. *New Journal of Physics*, 12(11):113032, November 2010.

[86] L. G. Rowan, E. L. Hahn, and W. B. Mims. Electron-Spin-Echo envelope modulation. *Physical Review*, 137(1A):A61, January 1965.

[87] Charles Santori, Philippe Tamarat, Philipp Neumann, Joerg Wrachtrup, David Fattal, Raymond G. Beausoleil, James Rabeau, Paolo Olivero, Andrew D. Greentree, Steven Prawer, Fedor Jelezko, and Philip Hemmer. Coherent population trapping of single spins in diamond under optical excitation. *Physical Review Letters*, 97(24):247401, December 2006.

[88] Wolfgang Schnitzler, Georg Jacob, Robert Fickler, Ferdinand Schmidt-Kaler, and Kilian Singer. Focusing a deterministic single-ion beam. *New Journal of Physics*, 12(6):065023, June 2010.

[89] Peter W. Shor. Scheme for reducing decoherence in quantum computer memory. *Physical Review A*, 52(4):R2493, October 1995.

[90] Peter W. Shor. Polynomial-Time algorithms for prime factorization and discrete logarithms on a quantum computer. *SIAM Review*, 41(2):303, 1999.

[91] Charles P. Slichter. *Principles of Magnetic Resonance (Springer Series in Solid-State Sciences)*. Springer, March 1996.

[92] Rogerio de Sousa. Electron spin as a spectrometer of nuclear spin noise and other fluctuations. *TOP.APPL.PHYS.*, 115:183, 2009.

[93] P Spinicelli, A Dréau, L Rondin, F Silva, J Achard, S Xavier, S Bansropun, T Debuisschert, S Pezzagna, J Meijer, V Jacques, and J-F Roch. Engineered arrays of nitrogen-vacancy color centers in diamond based on implantation of CN ⁻ molecules through nanoapertures. *New Journal of Physics*, 13(2):025014, February 2011.

[94] A. Steane. The ion trap quantum information processor. *Applied Physics B: Lasers and Optics*, 64(6):623–643, June 1997.

[95] A. M. Steane. Error correcting codes in quantum theory. *Physical Review Letters*, 77(5):793, July 1996.

[96] M. Steiner, P. Neumann, J. Beck, F. Jelezko, and J. Wrachtrup. Universal enhancement of the optical readout fidelity of single electron spins at nitrogen-vacancy centers in diamond. *Physical Review B*, 81(3):035205, January 2010.

[97] S. Steinert, F. Dolde, P. Neumann, A. Aird, B. Naydenov, G. Balasubramanian, F. Jelezko, and J. Wrachtrup. High sensitivity magnetic imaging using an array of spins in diamond. *Review of Scientific Instruments*, 81(4):043705, 2010.

[98] Julia Tisler, Gopalakrishnan Balasubramanian, Boris Naydenov, Roman Kolesov, Bernhard Grotz, Rolf Reuter, Jean-Paul Boudou, Patrick A. Curmi, Mohamed Sennour, Alain Thorel, Michael Boersch, Kurt Aulenbacher, Rainer Erdmann, Philip R. Hemmer, Fedor Jelezko, and Joerg Wrachtrup. Fluorescence and spin properties of defects in single digit nanodiamonds. *ACS Nano*, 3(7):1959–1965, July 2009.

[99] Goetz S. Uhrig. Keeping a quantum bit alive by optimized pi -Pulse sequences. *Physical Review Letters*, 98(10):100504, March 2007.

[100] Goetz S. Uhrig. Concatenated control sequences based on optimized dynamic decoupling. *Physical Review Letters*, 102(12):120502, March 2009.

[101] J. H. Van Vleck. The dipolar broadening of magnetic resonance lines in crystals. *Physical Review*, 74(9):1168, November 1948.

[102] G. Waldherr, J. Beck, M. Steiner, P. Neumann, A. Gali, Th. Frauenheim, F. Jelezko, and J. Wrachtrup. Dark states of single Nitrogen-Vacancy centers in diamond unraveled by single shot NMR. *Physical Review Letters*, 106(15), April 2011.

[103] J. R. Weber, W. F. Koehl, J. B. Varley, A. Janotti, B. B. Buckley, C. G. Van de Walle, and D. D. Awschalom. Quantum computing with defects. *Proceedings of the National Academy of Sciences*, 107(19):8513 –8518, May 2010.

[104] W. M. Witzel and S. Das Sarma. Quantum theory for electron spin decoherence induced by nuclear spin dynamics in semiconductor quantum computer architectures: Spectral diffusion of localized electron spins in the nuclear solid-state environment. *Physical Review B*, 74(3):035322, July 2006.

[105] William K. Wootters. Entanglement of formation of an arbitrary state of two qubits. *Physical Review Letters*, 80(10):2245, March 1998.

[106] Nan Zhao, Jian-Liang Hu, Sai-Wah Ho, Jones T. K. Wan, and LiuR. B. Atomic-scale magnetometry of distant nuclear spin clusters via nitrogen-vacancy spin in diamond. *Nat Nano*, 6(4):242–246, April 2011.